

Review

The Corrosion Performance and Mechanical Properties of Mg-Zn Based Alloys—A Review

Pingli Jiang ^{1,*}, Carsten Blawert ¹ and Mikhail L. Zheludkevich ^{1,2}

¹ Magnesium Innovation Centre (MagIC), Institute of Materials Research, Helmholtz-Zentrum Geesthacht, Max-Planck Str.1, 21502 Geesthacht, Germany; carsten.blawert@hzg.de (C.B.); mikhail.zheludkevich@hzg.de (M.L.Z.)

² Faculty of Engineering, University of Kiel, Kaiserstrasse 2, 24143 Kiel, Germany

* Correspondence: pingli.jiang@hzg.de

Received: 12 February 2020; Accepted: 21 April 2020; Published: 23 April 2020



Abstract: Magnesium alloys have shown great potential for applications as both structural and biomedical materials due to their high strength-to-weight ratio and good biodegradability and biocompatibility, respectively. Among them, Mg-Zn based alloys are attracting increasing interest for both applications. As such, this article provides a review of the corrosion performance and mechanical properties of Mg-Zn based alloys, including the influence of environment and processing on both of them. The strategies for tailoring corrosion resistance and/or mechanical properties by microstructure adjustment and surface treatment are discussed.

Keywords: magnesium alloys; zinc; corrosion performance; mechanical property

1. Introduction

Magnesium (Mg) alloys have drawn increasing attention during the past two decades for applications in the automotive, aerospace, and electronics industries due to their high specific strength and stiffness, low density, good castability, and machinability [1–4]. In addition, they have also been considered as attractive candidates for application as biodegradable implant materials because of their mechanical properties that are similar to those of natural bone, good biodegradability, and inherent biocompatibility [5–9]. To expand the application scope of Mg alloys, alloying is one of the most effective strategies for the further enhancement of mechanical properties and corrosion performance [10].

Magnesium–aluminum (Mg–Al) based alloys are the most widely studied and used Mg alloys due to their excellent castability, reasonable mechanical properties at room temperature, and good corrosion resistance [11]. However, the mechanical properties of Mg–Al based alloys significantly decrease as temperature rises above 130 °C, above which softening of the β -Mg₁₇Al₁₂ phases, precipitated at grain boundaries, results in poor creep resistance [12,13]. Additionally, Al has been reported to be a neurotoxicant, and the accumulation of Al can induce various neurological disorders during the degradation of Mg–Al alloys in the human body [14]. Therefore, the development of Al-free Mg alloys is desired.

Zinc (Zn) is the second most common alloying element for commercial Mg alloys [15,16]. Zn alloying additions can lead to a higher free corrosion potential of the MgZn alloy compared to that of pure Mg, reduce the corrosion rate, and improve the mechanical properties through a solid solution hardening mechanism [17,18]. Moreover, in comparison with Mg–Al series alloys, the presence of heat-resistant intermetallics results in the much higher creep resistance and the better tensile properties of Mg–Zn–Al alloys at elevated temperatures [19,20]. Furthermore, Zn is one of the essential trace elements for the human body and is crucial for many biological functions, such as the immune system

and sense of smell and taste [21]. Thus, the Mg-Zn system shows great potential as a low-cost Mg alloy alternative with high strength in industrial applications, and has attracted increasing interest for medical applications.

Motivated by the new trend of biomedical applications for Mg-Zn based alloys, the objective of this article is to provide a review of the corrosion performance and mechanical properties of Mg-Zn based alloys developed for both industrial and biomedical applications. Potentials or relative Volta potentials of some secondary phases in Mg-Zn based alloys and the corrosion rates and mechanical properties of Mg-Zn based alloys summarized from publications are compared in Tables A1 and A2 in the Appendix A. The influence of environment and processing on the corrosion behavior and mechanical properties of Mg-Zn based alloys are also reviewed. The strategies for improving the properties of Mg-Zn based alloys are discussed based on microstructure design and surface modification. Finally, typical applications are shortly summarized.

2. Binary Mg-Zn Alloys

2.1. Mg-Zn System

The maximum solid solubility of Zn in Mg is considered to be relatively high at high temperatures [22,23], e.g., 2.5 at.% (6.2 wt.%) at 325 °C, as indicated by the binary Mg-Zn phase diagram proposed by Okamoto et al. [24] and shown in Figure 1. However, with decreasing temperature, only 0.6 at.% (1.6 wt.%) Zn remains soluble in the Mg matrix and contributes to solid solution strengthening [22,25,26]. Excess Zn will form intermetallic phases. In the Mg-Zn system, five intermetallic phases, namely $Mg_{51}Zn_{20}$ (previously denoted as Mg_7Zn_3 [27]), $MgZn$, Mg_2Zn_3 (previously denoted as Mg_4Zn_7 [28,29]), $MgZn_2$, and Mg_2Zn_{11} , exist. The primary Mg_7Zn_3 phase has a body-centered orthorhombic structure [30]. The crystal structures of $MgZn$, $MgZn_2$, and Mg_2Zn_{11} are base-centered monoclinic [31], hexagonal [32], and cubic [33], respectively. However, the structure of the Mg_4Zn_7 phase is under debate, assumed to be a triclinic structure by Gallot and Graf [34], but reported to be a base-centered monoclinic structure by Gao and Nie [31]. It is believed that the Mg_xZn_y intermetallics can provide a pronounced age hardening effect [35–37], but they are detrimental to the corrosion resistance of the alloy due to accelerated cathodic reaction rates [38–40].

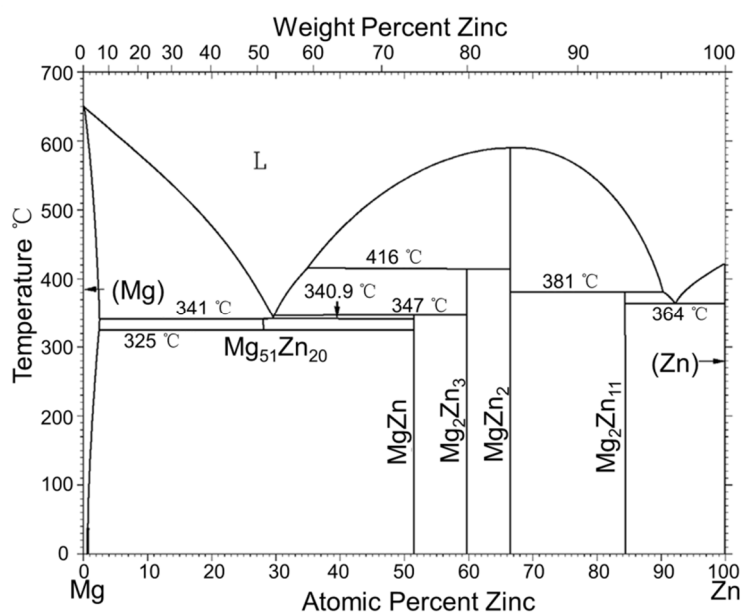


Figure 1. The binary Mg-Zn phase diagram [24] (with permission from Springer Nature and Copyright Clearance Center).

2.2. Influence of Zn Content on the Corrosion and Mechanical Properties of Binary Mg-Zn Alloys

Addition of Zn as an alloying element can refine the grain size and improve the corrosion resistance and mechanical properties of Mg [10,41]. Compared with pure Mg and high-purity AZ31 alloy, almost one order of magnitude improvement of corrosion resistance can be achieved by small additions of Zn (1 wt.%) [10,42]. Since the electrode potential of Zn (-0.762 V vs. Standard Hydrogen Electrode) is higher than that of Mg (-2.372 vs. Standard Hydrogen Electrode), and Zn is known to have a high hydrogen evolution over-potential, the improved corrosion resistance is presumably attributed to the reduced hydrogen evolution kinetics by Zn in solid solution [42]. It was also suggested that Zn can increase the tolerance limits of impurities (iron (Fe), copper (Cu), nickel, and cobalt) in Mg, which enhances the corrosion resistance of Mg via weakening of the galvanic corrosion between impurities and Mg [1,43,44]. In addition, Gu et al. [45] have reported that the corrosion resistance of as-cast Mg1Zn (in wt.%) alloy is higher compared to several other binary Mg alloys alloyed with the same amount (Ag, Al, In, Mn, Si, Sn, Y, and Zr). Generally, the corrosion resistance and mechanical properties of Mg-Zn binary alloys strongly depend on Zn content. When the added amount of Zn is lower than 5 wt.%, an increase in Zn content enhances the general and localized corrosion resistance of as-cast Mg-Zn alloys in simulated body fluid (SBF) at 37 °C, which is due to the refinement of grain size and the facilitated formation of protective surface film induced by Zn [10,41,46]. However, much higher levels of Zn (up to 7 wt.%) can result in the formation of a significant amount of secondary phases. As a result, severe localized corrosion occurs due to the galvanic effect between intermetallics and matrix, and, consequently, a decrease of the overall corrosion resistance is found [10,47,48]. Opposite results have been reported by Kubàsek et al. [42,49], showing that the corrosion rates of Mg-Zn binary alloys increase with increasing Zn amount in the range of 0–6 wt.% when testing is performed in either simple sodium chloride (NaCl) solution or simulated body fluid. This finding is ascribed to the increased galvanic effect due to the increase in volume fraction of secondary phases.

The yield (YS) and ultimate tensile strength (UTS) of binary Mg-Zn alloys increase with increasing Zn content when Zn wt.% is in the range of 0–4 wt.% [10,22,46,50]. This is a combined result of fine grain strengthening [51–53], solid solution strengthening [25,26,54], and precipitation hardening effects [54,55]. Nevertheless, when alloying with higher amounts of Zn, plenty of secondary phases will form at the grain boundaries. They will result in the increased dislocation density and act as new crack sources [10]. Consequently, the tensile strength of the alloy can be significantly reduced.

Binary Mg-Zn alloys with much higher amounts of Zn (>10 wt.%) produced by using powder metallurgy have only been studied by Yang et al. [55]. High Zn content (>10 wt.%) causes the formation of large-size secondary phases and undissolved Zn particles, which results in severe pitting and localized corrosion due to the formation of galvanic cells, thus reducing the corrosion resistance of the alloys (corrosion current density: $16.9 \mu\text{A cm}^{-2}$ for Mg6Zn alloy, $54.2 \mu\text{A cm}^{-2}$ for Mg14.5Zn alloy, $80.3 \mu\text{A cm}^{-2}$ for Mg20.3Zn alloy, $132.2 \mu\text{A cm}^{-2}$ for Mg40.3Zn alloy). The compression strength increases with increasing Zn content, but reaches the highest value when Zn content reaches 14.5 wt.% (373.5 MPa for M6Zn alloy, 396.5 MPa for Mg14.5Zn alloy, 371.7 MPa for Mg20.3Zn alloy, 354.6 MPa for Mg40.3Zn alloy). Above this value, further addition of Zn is detrimental because large-size secondary phases and Zn particles formed in the alloy could act as crack sources [56].

Considering the aforementioned dependence of a good combination of mechanical properties and corrosion resistance on Zn content, Zhang et al. [22] have suggested that the Zn content of MgZn alloys should be limited to 4 wt.%. Figure 2 depicts the influence of Zn content on the corrosion rate and tensile properties of Mg-Zn binary alloys, summarizing the data provided in the literature. This shows that, as Zn content varies, the corrosion rate of MgZn alloy changes differently between different reports (Figure 2). One of the reasons might be the fact that other influences besides the Zn content do affect the corrosion rate. The most obvious is the electrolyte composition, which was not the same in all of the experiments (see Table A2 in Appendix A). Two other important influence factors are the microstructure of the alloy (e.g., grain size and distribution of secondary phases) and the impurity levels of the tested alloys. Generally, more secondary phases and more impurities would lead to faster

corrosion and severer localized corrosion of the alloy. In contrast, an average tendency can be observed for the influence of Zn content on tensile properties. The yield and ultimate tensile strength increase while elongation to fracture decreases with increasing Zn content in the range of 0–4 wt.%. It can be noted that studies about binary Mg-Zn alloys are still quite limited and many inconsistencies exist, suggesting that more systematic studies are needed.

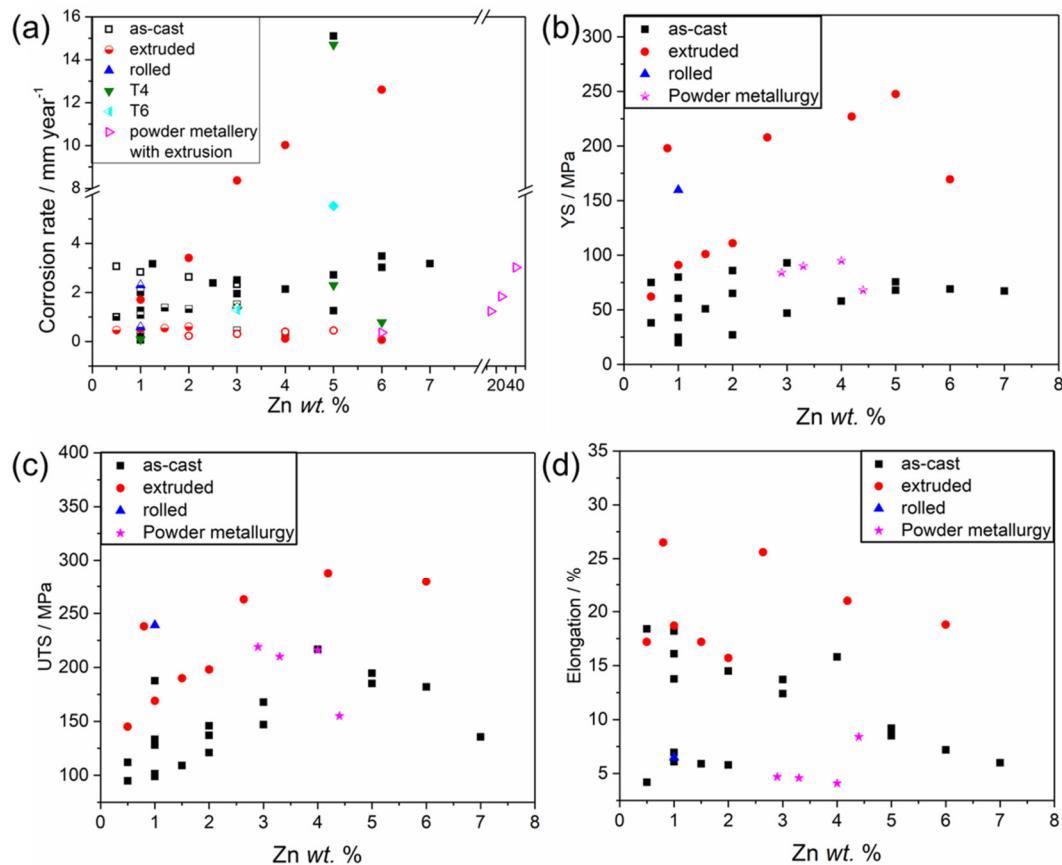


Figure 2. Influence of Zn wt.% on (a) corrosion rate (solid symbols refer to corrosion rate of Mg alloys measured by gravimetric method (P_w), half-up open symbols refer to corrosion rate of Mg alloys measured by hydrogen evolution (P_H), and open symbols refer to corrosion rate of Mg alloys evaluated from corrosion current density (P_i)), (b) yield strength, (c) ultimate tensile strength, and (d) elongation to fracture of binary Mg-Zn alloys reproduced from the literature [10,22,26,40–42,45–50,54,56–61].

3. Ternary Mg-Zn-X Alloys

Superior combinations of corrosion resistance and mechanical properties of as-cast Mg-Zn based alloys can often be improved by the addition of a third alloying element or microstructure modification via heat treatment or mechanical processing.

3.1. Influence of Microstructure on the Corrosion and Mechanical Properties

Microstructural features, such as grain size, volume fraction, and distribution of secondary phases, generally play an important role in the corrosion behavior of Mg alloys. It is widely accepted that refined grain size is beneficial to the corrosion resistance of Mg alloys in neutral and alkaline sodium chloride (NaCl) corrosive electrolytes [62–67]. However, large residual stresses, which can be introduced during grain refinement, can be detrimental to the corrosion resistance of Mg [63,64]. Song et al. have reported that the influence of secondary phases on corrosion behavior of Mg alloys depends on the amount and distribution of the secondary phases [1,68,69]. They can either act as a galvanic cathode to accelerate the corrosion rate, or as a continuous barrier with higher corrosion

resistance (compared with the Mg matrix) when exposed to the corrosive environment after the dissolution of the top Mg matrix (Figure 3). Lu et al. [70] have studied the combined influence of secondary phases and grain size on the corrosion of as-cast and heat-treated Mg₃Zn0.3Ca (in wt.%) alloy. The results (Figure 4) indicate that both the volume fraction of secondary phases and grain size are important for controlling the corrosion of the alloy. When the influence of grain size is dominating the corrosion process of the alloy, the large grain size would lead to the increase of the corrosion rate. Vice versa, when the secondary phase volume fraction is high, it overrules the beneficial effect of fine grain size.

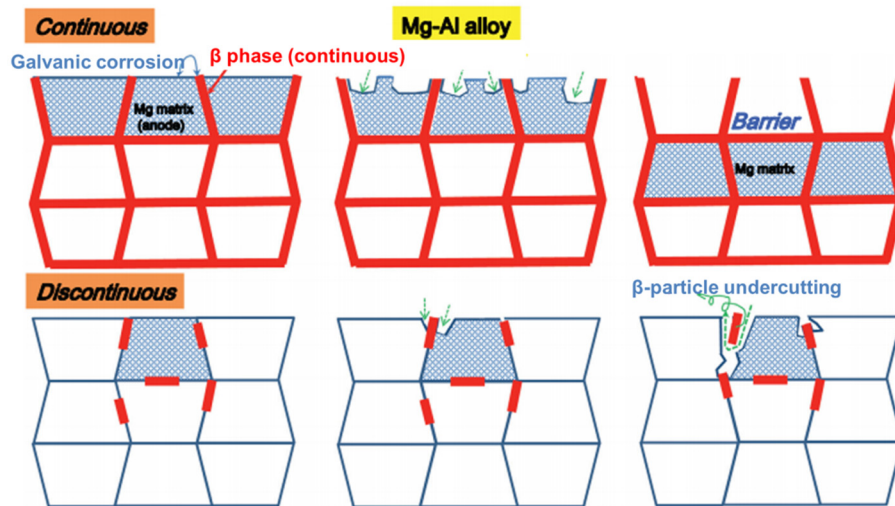


Figure 3. Influence of distribution of secondary phases on corrosion behavior of Mg alloys (AZ91D alloy as representative) [71] (with permission from Elsevier and Copyright Clearance Center).

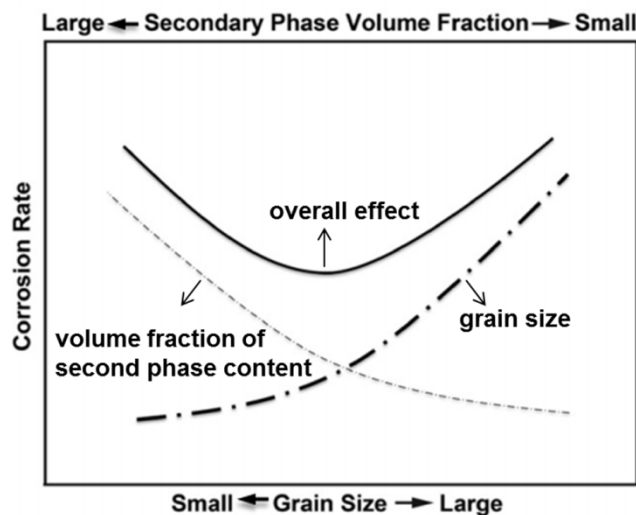


Figure 4. Schematic illustration showing the effect of volume fraction of secondary phases and grain size on the corrosion rate of Mg₃Zn0.3Ca alloy [70] (with permission from Elsevier and Copyright Clearance Center).

3.1.1. Mg-Zn-Ca Alloys

Due to their good biocompatibility, Mg-Zn-Ca alloys have attracted attention in research of Mg alloys for biomedical devices. Calcium (Ca) behaves as an effective grain refiner for MgZn alloys [5,72,73]. The phase formation depends on the contents of Zn and Ca (especially the Zn/Ca ratio), and affects the corrosion performance of the alloy. It has been pointed out that eutectic α -Mg + Mg₂Ca

+ $\text{Ca}_2\text{Mg}_6\text{Zn}_3$ phase precipitates when Zn/Ca atomic ratio is lower than 1.2, while $\alpha\text{-Mg} + \text{Ca}_2\text{Mg}_6\text{Zn}_3$ eutectic phase is formed when Zn/Ca atomic ratio is higher than 1.2 [5,74]. A new phase $\text{Ca}_2\text{Mg}_5\text{Zn}_{13}$ has also been reported in the case of $\text{Mg}_6\text{Zn}_1\text{Ca}$ (in wt.%) alloy [23]. Mg_2Ca and $\text{Ca}_2\text{Mg}_6\text{Zn}_3$ phases usually distribute along the grain boundary and form interdendritic interstices in as-cast Mg-Zn-Ca alloys. A segregation of Zn may occur in the vicinity of Mg_2Ca phase, consequently protecting this area (Mg_2Ca phase) against corrosion [75,76]. Mg_2Ca is more active than $\alpha\text{-Mg}$ matrix, while $\text{Ca}_2\text{Mg}_6\text{Zn}_3$ is nobler than $\alpha\text{-Mg}$ [75,77]. Therefore, $\text{Ca}_2\text{Mg}_6\text{Zn}_3$ phase with discontinuous distribution can act as a cathode site, accelerating galvanic corrosion of the matrix, but can act as a barrier when the $\text{Ca}_2\text{Mg}_6\text{Zn}_3$ phase is continuously distributed in the microstructure, e.g., along the grain boundary [75].

When the content of Ca is lower than 1 wt.%, alloying additions of Ca improve the corrosion resistance of Mg-Zn alloys by forming compounds with elemental impurities and thus purifying the melts, while more addition of Ca leads to the formation of secondary phases and thus results in increased pitting corrosion with increasing overall corrosion rate [5,22,59,73,75]. It has been reported that $\text{Ca}_2\text{Mg}_6\text{Zn}_3$ and $\text{Ca}_2\text{Mg}_5\text{Zn}_{13}$ phases have strengthening effects [16,78,79]. Thereby, grain refinement and precipitate strengthening would contribute to an improvement in mechanical properties of Mg-Zn-Ca alloys. Nevertheless, with increasing Ca content, Mg_2Ca and $\text{Ca}_2\text{Mg}_6\text{Zn}_3$ phases continuously precipitate along the grain boundary, which is detrimental to the tensile properties of the alloy, since Mg_2Ca is a brittle phase and can produce crack sources that can lead to brittle failure [5,22,80,81].

Increasing the Zn content promotes the corrosion of Mg-Zn-Ca alloys because, as aforementioned, nobler $\text{Ca}_2\text{Mg}_6\text{Zn}_3$ secondary phases form and thus accelerate galvanic corrosion [7,23,82]. However, the yield and tensile strength of the alloy can be enhanced with the increase of the Zn content when Zn concentration is in the range of 0–4.0 wt.%, which is due to the solid solution hardening and precipitation strengthening effects [7,23]. Nevertheless, more Zn addition would result in decline of mechanical properties of Mg-Zn-Ca alloys and change the fracture type from ductile to brittle [23].

On the basis of the above discussion, the corrosion and mechanical properties of Mg-Zn-Ca alloys can be optimized by adjusting the content of Zn and Ca, influencing the microstructure. Geng et al. studied Mg_4ZnCa (in wt.%) alloys with micro-alloying addition of 0.2 wt.% Ca (corrosion and mechanical properties) [6] and 0.5 wt.% Ca (only mechanical property) [16], respectively. The corrosion properties of $\text{Mg}_4\text{Zn}_0.2\text{Ca}$ alloys are similar to those of high-purity Mg in SBF. In addition, both of these two alloys exhibit good mechanical properties, especially $\text{Mg}_4\text{Zn}_0.5\text{Ca}$, which shows a good balance between tensile strength and ductility. The tensile strength and elongation to fracture are 185 MPa and 12.5% for $\text{Mg}_4\text{Zn}_0.2\text{Ca}$ alloy and 211 MPa and 17% for $\text{Mg}_4\text{Zn}_0.5\text{Ca}$ alloy, respectively [6,16]. Furthermore, tensile strength and elongation to fracture can be further enhanced by extrusion. The integrity of the alloy with 0.2Ca is still given even after immersion for 30 days in SBF, and the mechanical properties are still high enough (ultimate strength: 220 MPa, yield strength: 160 MPa, ductility: 8.3) for bone fixture applications.

3.1.2. Mg-Zn-Y Alloys

The solubility of Zn in the Mg matrix is greatly decreased when Y is incorporated as an alloying addition. This decrease is believed to be a result of the interaction between Zn and Y [53]. Ternary MgZnY phases would precipitate firstly at grain boundaries because of the higher eutectic temperature of ternary phases compared with that of binary phases [83]. The phase constituency in Mg-Zn-Y alloys is strongly dependent on the weight ratio of Zn to Y for both low (2 wt.%) and high (≥ 3 wt.%) Zn-containing systems [53,83,84]. When the Zn/Y weight ratio is lower than 1.5, Mg_{12}ZnY phase precipitates (X-phase or LPSO phase—long period stacking ordered phase). When the Zn/Y weight ratio is 1.5–2, $\text{Mg}_3\text{Zn}_3\text{Y}_2$ phase (W-phase, dendritic phase) forms in the interdendritic region. When the Zn/Y ratio increases to 2–2.5, $\text{Mg}_3\text{Zn}_6\text{Y}$ phase (I-phase, icosahedral quasicrystal phase) begins to form and co-exists with W-phase. When the Zn/Y ratio is 5–7, only I-phase forms in the Mg-Zn-Y alloy. However, with further increase of the Zn/Y ratio (~ 10), the composition is close to that of the binary Mg-Zn

system; thus, mainly binary MgZn phases form [84,85]. Those secondary phases are electrochemically nobler than the α -Mg matrix and can thus be effective cathode sites when the alloys are exposed to corrosive environments, resulting in pitting corrosion at the secondary phase/ α -Mg interface. With similar sizes and volume fractions of intermetallic particles, MgZnY alloys with a single secondary phase (e.g., Mg₃Zn₆Y I-phase) exhibit better corrosion resistance than those with two secondary phases (e.g., Mg₃Zn₃Y₂ W-phase and Mg₃Zn₆Y I-phase) [53,86]. Generally, with the increase of volume fraction of secondary phases with discontinuous distribution, the corrosion properties of the alloys would deteriorate, since the effective cathode area increases [87–89]. However, continuous distribution and moderate volume fraction of secondary phases can hinder the corrosion propagation [87,88]. For example, Mg₉₇Zn₁Y₂ alloy (continuous distribution, volume fraction of secondary phases: 30.4%) has higher corrosion resistance compared with Mg_{98.5}Zn_{0.5}Y₁ alloy (discontinuous distribution, volume fraction of secondary phases: 11.5%), Mg₉₄Zn₂Y₄ alloy (continuous distribution, volume fraction of secondary phases: 55.4%) and Mg₈₈Zn₄Y₈ alloy (continuous distribution, volume fraction of secondary phases: 63.2%) [87]. Li et al. [88] have studied the influence of volume fraction of LPSO phases on the corrosion resistance of Mg_{0.9}Zn_{1.6}Y, Mg_{2.1}Zn_{5.2}Y, and Mg_{3.1}Zn_{7.6}Y (all in wt.%) alloys in 0.1 M NaCl solution. It has been revealed that the Volta potential difference at the LPSO phase/ α -Mg interface could be up to 250 mV (Figure 5b). As a result, severe micro-galvanic corrosion preferentially occurs at the LPSO/ α -Mg interfaces. Then, the corrosion progresses along the boundary of LPSO phases instead of in the α -Mg matrix (Figure 5c,d). A new phase (currently cannot be indexed) has been found in the Raman spectra of the corrosion products forming on LPSO phases besides magnesium hydroxide (Mg(OH)₂).

The mechanical properties of Mg-Zn-Y alloys also largely rely on the phase constituency. The presence of stable I-phase is beneficial for the mechanical properties of Mg-Zn-Y alloys, especially at elevated temperatures [90–92], due to the low interfacial energy between the I-phase and α -Mg matrix. The yield and tensile strengths of the alloys increase with increasing volume fraction of I-phase [84,90,93]. W-phase also contributes to the strength, but not as effectively as I-phase. However, W-phase has a better softening effect than I-phase, which is beneficial for the ductility of the alloys [53,94]. Many reports have demonstrated that the LPSO phases are effective for strengthening of Mg alloys [88,95–102]. Kawamura et al. have firstly reported a Mg₉₇Zn₁Y (in at.%) alloy with high yield strength of 610 MPa, usable ductility (5%), and a yield strength of 300 MPa at 473 K due to the presence of LPSO phase [103]. The strengthening mechanisms of LPSO phase were attributed to four mechanisms: (1) increased critical resolved shear stress (CRSS) of the basal plane, (2) activated non-basal slip, (3) kinking bands on LPSO formed during the deformation process, and (4) a coherent LPSO/Mg interface along the basal and prismatic planes [104–106]. However, the improvement of strength is slight (the ultimate strength is only increased from 141 MPa to 148 MPa) when the volume fraction of LPSO phases exceeds 20.3%, and even declines with much higher LPSO phase concentration because of the large length and thickness of the LPSO phases [88,96]. The influences of different phases on the mechanical properties of Mg-Zn-Y alloys are summarized in Table 1. In addition to the abovementioned influence of phase constituency, conditions of the alloys should also be taken into serious consideration during the optimization of mechanical properties.

Table 1. Summary of mechanical properties of Mg-Zn-Y alloys containing different secondary phases.

Composition	Condition	Containing Phases	Mechanical Properties (Room Temperature)			Refs.
			YS/MPa	UTS/MPa	Elongation/%	
Mg97Zn1Y2 (at.%)	Rapidly solidified powder metallurgy	LPSO phase	610	-	5	[103]
Mg97Zn1Y2 (at.%)	High-frequency induction melting + warm extrusion	LPSO phase	350	410	6	[98]
Mg97Zn1Y2 (at.%)	Conventional casting + extrusion	LPSO phase	-	400	12.5	[100]
Mg97Zn1Y2 (at.%)	Conventional casting + ECAP	LPSO phase	400	450	2.5	[102]
Mg3.1Zn7.6Y (wt.%)	Conventional casting	LPSO phase	107	148	3	[88]
Mg94Zn2Y4 (wt.%)	Conventional casting	LPSO phase	155	236	3.7	[96]
Mg94Zn3Y3 (wt.%)	Conventional casting + hot-rolling	LPSO phase + W-phase	380	-	6	[97]
Mg96Zn2Y2 (wt.%)	High-frequency induction melting + extrusion	LPSO phase + W-phase	390	420	5	[99]
Mg1.5Zn0.8Y (wt.%)	Conventional casting + hot-rolling	W-phase	178 *	225	18	[94]
Mg2Zn1.54Y (wt.%)	Conventional casting + extrusion	W-phase	214	266	27	[53]
Mg2Zn0.82Y (wt.%)	Conventional casting + extrusion	W-phase + I-phase	213	266	25	[53]
Mg2Zn0.36Y (wt.%)	Conventional casting + extrusion	I-phase	197	261	23	[53]
Mg96.27Zn3.3Y0.43 (at.%)	Rapidly solidified powder metallurgy + extrusion	I-phase	412	445	13	[107]
Mg95Zn4.3Y0.7 (at.%)	Conventional casting + hot-rolling	I-phase	220 *	370	19.7	[90]
Mg12Zn2.4Y (wt.%)	Conventional casting + hot-rolling	I-phase	189	286	21.3	[108]

* means 0.2% yield strength.

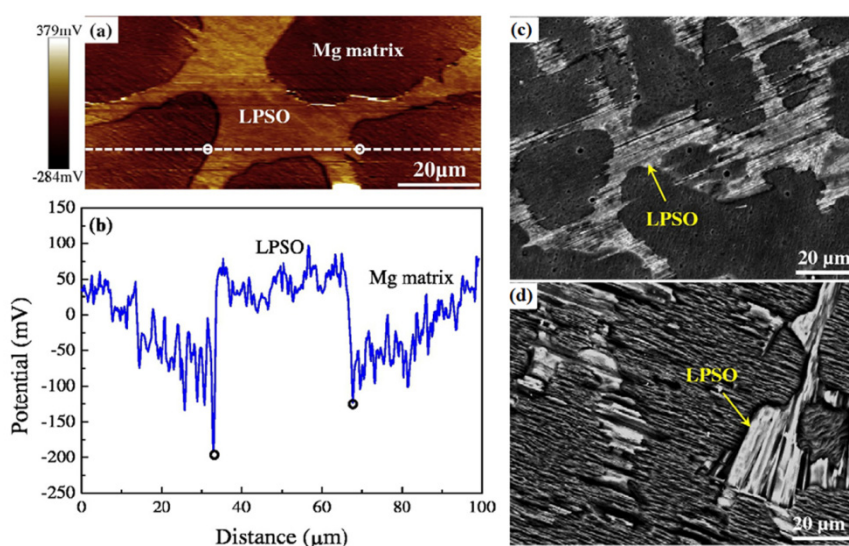


Figure 5. Scanning kelvin probe force microscopy (SKPFM) results of Mg_{3.1}Zn_{7.6}Y (in wt.%) alloy: (a) Surface Volta potential map and (b) line-profile analysis of relative Volta potential through the LPSO phase in (a). Scanning electron microscopy (SEM) surface morphologies of Mg_{3.1}Zn_{7.6}Y alloy after immersion in 0.1 M NaCl solution for (c) 2 h and (d) 4 h [88] (with permission from Elsevier and Copyright Clearance Center).

3.1.3. Mg-Zn-Mn Alloys

It is well known that manganese (Mn) is effective in combining with some heavy metal impurities, for example, Fe, thereby decreasing the galvanic corrosion between impurities and the Mg matrix [44]. When Mn is micro-alloyed (Mn wt.% < 1.0 wt.%) with the Mg-Zn system, Mn exists in a soluble state, and some binary MgZn phases precipitate with increase of Zn content in the range of 0 to 3 wt.% [109–112]. In addition, Mn in solid solution could stabilize the corrosion product layer formed when alloys corrode in corrosive environments by incorporating manganese as an oxide into the Mg(OH)₂ layer [51,112]. Rosalbino et al. [51] have found that Mg₂Zn_{0.2}Mn exhibits the best corrosion resistance in comparison with Mg₂Zn_{0.2}Ca, Mg₂Zn_{0.2}Si (all in wt.%), and AZ91 alloys, revealing a four-fold increase in polarization resistance over that of AZ91 alloy after exposure for 168 h in Ringer's solution at 37 °C. Moreover, it has been reported by Abidin et al. [113] that the steady state corrosion rate of Mg₂Zn_{0.2}Mn (wt.%) alloy tested in Hank's solution at 37 °C is much lower than that of high-purity Mg. However, this has been ascribed to a lower content of Fe impurity particles in the Mg₂Zn_{0.2}Mn alloy. In addition to MgZn₂ phase, additions of silicon (Si, 0–2 wt.%) into Mg-Zn-Mn alloys can induce the formation of Mg₂Si and Mn₅Si₃ phases, but only Mg₂Si phase influences the corrosion resistance of the alloy significantly [114]. The role of Mg₂Si phase on the corrosion property of the alloy depends on its morphology and volume fraction in the microstructure (Figure 6). When Mg₂Si is in Chinese script type (0.5 wt.% Si), the corrosion rate is higher than that in the polygonal type. However, when the morphology of Mg₂Si phase changes from Chinese script type to polygonal type with increasing Si content (1 wt.% and 2 wt.%), the corrosion resistance of the alloy increases again [114–116].

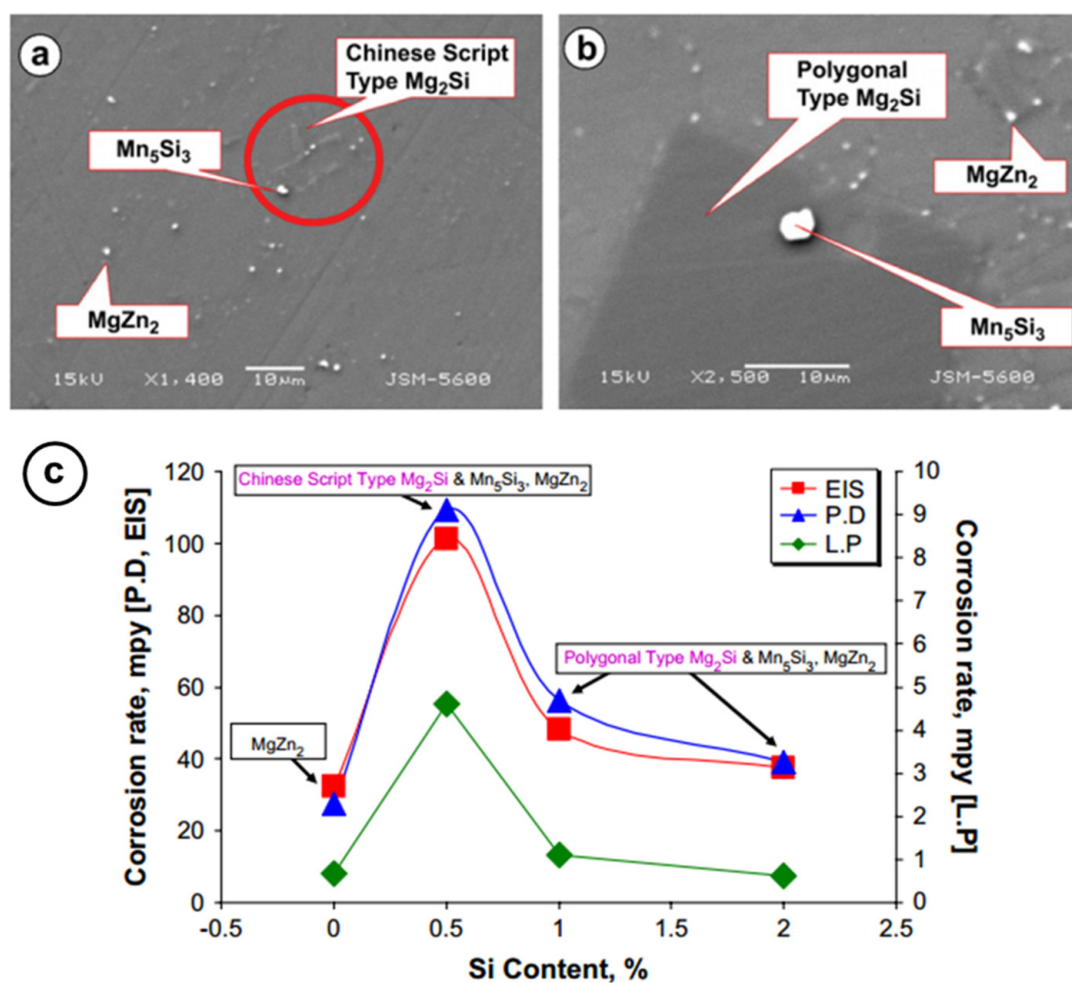


Figure 6. Microstructures of (a) $\text{Mg}_6\text{Zn}_{0.5}\text{Mn}_{0.5}\text{Si}$ and (b) $\text{Mg}_6\text{Zn}_{0.5}\text{Mn}_2\text{Si}$ alloys (wt.%) determined by SEM. (c) Influence of Mg_2Si phase on the corrosion rates of $\text{Mg}_6\text{Zn}_{0.5}\text{Mn}_x\text{Si}$ ($x = 0, 0.5, 1.0, 2.0$; wt.%) alloys in 3.5% NaCl solution saturated with $\text{Mg}(\text{OH})_2$ (EIS: Electrochemical impedance spectroscopy, P.D: Potentiodynamic polarization measurements, L.P: Linear polarization measurements) [114] (with permission from Elsevier and Copyright Clearance Center).

3.1.4. Representative Mg-Zn-RE and Mg-Zn-Zr Based Alloys

Generally, the addition of rare earth (RE) elements is beneficial for the mechanical properties of Mg alloys at elevated temperatures, and zirconium (Zr) is considered to behave as an effective grain refiner [117,118]. Thus, many efforts have been devoted to the development of RE/Zr-containing Mg alloys with fine grains. Representatively, Mg-Zn-RE (ZE) and Mg-Zn-Zr (ZK) alloys have been widely studied for automotive/aerospace and biomedical applications, especially commercial ZE41 and ZK60 alloys.

The corrosion resistance of ZE41 alloy is poor, with a corrosion rate twice as high as that of AZ91D and about thirteen times higher than that of pure Mg in 1 M NaCl solution [119]. $\text{Mg}_7\text{Zn}_3\text{RE}$ (T-phase) and Mg_{12}RE phases with nobler corrosion potential can precipitate along the grain boundaries, as well as inside of the grains, thereby inducing severe galvanic corrosion. As a result, the Mg matrix adjacent to the secondary phases will dissolve preferentially; then, pitting and intergranular corrosion can occur [118,120]. Caution should be paid during mass loss measurements because the T-phase could be dissolved by chromium-trioxide-based corrosion product removal solutions [121], thus leading to misleading results of corrosion rate. Furthermore, with micro-additions of Zr into ZE41 alloy, a so-called Zr-rich interaction zone can form within the grains and Zr-rich particles, together with some Zn and Fe precipitates can be found in those Zr-rich regions (shown in Figure 7) [121–123].

Consequently, the Zr-rich zones are also favorable sites for galvanic-driven localized corrosion attack (galvanic couple between the Zr-rich particles and the surrounding matrix).

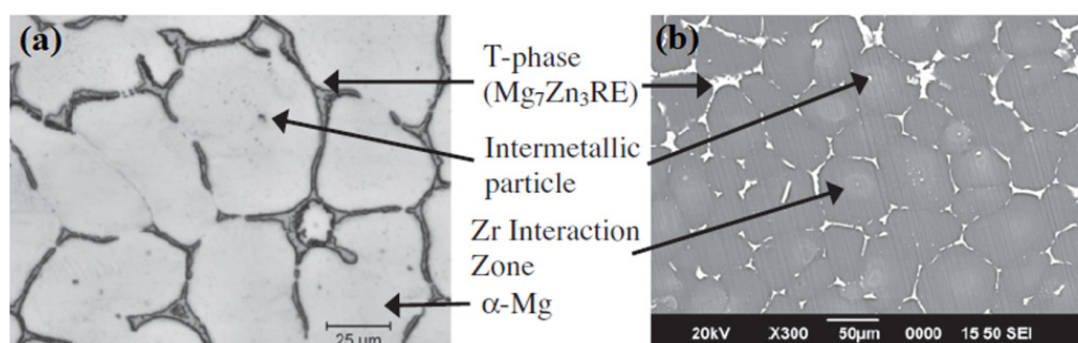


Figure 7. Microstructure of ZE41A alloy obtained by (a) optical micrograph and (b) SEM micrograph [122] (with permission from Elsevier and Copyright Clearance Center).

ZK60 alloy has wide engineering applications due to its good combination of tensile strength (≥ 250 MPa) and uniform elongation ($\geq 15\%$) [124]. However, a piece of $\phi 28$ mm \times 5 mm specimen can degrade completely after 12 weeks of immersion in Hank's solution due to the galvanic corrosion between binary MgZn phases (Mg_7Zn_3 or MgZn_2) and the Mg matrix [125]. This fast degradation rate cannot meet the requirements of biomedical applications [126]. By optimizing the content of Zn ($\text{Mg}_3\text{Zn}_0.6\text{Zr}$, in wt.%) in Mg-Zn-Zr alloy, the corrosion rate of Mg-Zn-Zr alloy can be comparable to that of WE43 alloy, which exhibits good corrosion behavior relative to AZ31, AZ91, and LAE42 alloys [125,127]. The further addition of Y and/or neodymium (Nd) into Mg-Zn-Zr alloys results in the precipitation of less noble T-phase and/or W-phase, and leads to the formation of more a compact corrosion product layer with higher corrosion resistance [128,129]. It is quite often observed for Mg alloys that the protective film is denser when the overall corrosion rate is low. Too much and fast $\text{Mg}(\text{OH})_2$ formation results in more compact films with coarse needle-like structures [130]. The tensile properties of Mg-Zn-Zr alloys further alloyed with some rare earth elements (Nd, Gd, etc.) strongly depend on the microstructure of the alloy, i.e., the types and shapes of secondary phases [131–135]. For example, the addition of 2 wt.% Nd into $\text{Mg}_5\text{Zn}_0.6\text{Zr}$ (in wt.%) alloy leads to the formation of a continuous network of intergranular phases, which significantly deteriorates the ultimate strength and elongation to fracture. However, the presence of discontinuous phases in $\text{Mg}_5\text{Zn}_0.6\text{Zr}_2\text{Nd}_0.5\text{Y}$ (in wt.%) favors the ultimate strength and elongation to fracture [136].

Gadolinium (Gd) has a large solubility in Mg (23.49 wt.% at 548 °C and 3.82 wt.% at 200 °C), but binary MgGd (Mg_5Gd or Mg_3Gd) phase and/or ternary MgZnGd ($\text{Mg}_3\text{Gd}_2\text{Zn}_3$) phase precipitate in the matrix when Gd is alloyed to the Mg-Zn system. Similar to the Mg-Zn-Y alloys, the phase constitutions of Mg-Zn-Gd alloys also strongly depend on the Zn/Gd atomic ratio [137]. Small amounts of Gd addition (1 wt.%) are beneficial to the corrosion resistance of the Mg1Zn (in wt.%) system. Furthermore, both Gd and Zn enrich in the Mg matrix surrounding the secondary phases, improving the corrosion resistance of the matrix [49]. Yang et al. [138,139] have studied the influence of varying Gd content (from 0.5 up to 5 wt.%) on the microstructures and mechanical properties of the Mg4.5Zn (in wt.%) system. It has been revealed that Gd can refine the grains when additions are less than 2 wt.%, and further increase of Gd content would cause increasing grains. The strength of the Mg4.5Zn alloy is improved with increasing Gd addition up to 2 wt.%, but deteriorates with further increase of Gd content. This is related to the effects of grain size, solid solubility of Zn and/or Gd, and the size and volume fraction of secondary phases.

3.1.5. Other Mg-Zn-X Alloys

Addition of strontium (Sr) can also refine the microstructure of Mg-Zn alloys in spite of its limited solubility in Mg (0.11 wt.% at 858 K), and the refinement effect increases with increasing Sr content (0.1–1 wt.%) due to precipitate formation [140,141]. Although nobler secondary phases (compared with Mg matrix) precipitate, the corrosion behavior of Mg₄Zn₁Sr (in wt.%) is superior to that of pure Mg [142]. Nevertheless, the corrosion rate of Mg-Zn-Sr alloy increases with the increase of either Zn or Sr contents due to the enhanced galvanic corrosion induced by the increased amount of secondary phases. In comparison, the strength of Mg-Zn-Sr alloys is improved when both Zn (2–6 wt.%) and Sr (0.2–1 wt.%) contents increase, because of the refined grains and homogeneously distributed secondary phases [140,143].

A few studies have also been carried out to investigate the influence of alloying with silver (Ag), Cu, germanium (Ge), etc. on the corrosion and/or mechanical properties of an Mg-Zn system. For example, Ben-Hamu et al. [144] have revealed that addition of Ag into an Mg₆Zn (in wt.%) system is harmful to the corrosion resistance due to the galvanic coupling between Ag₁₇Mg₅₄ phases and the α -Mg matrix, but contributes to the hardness of the alloy. Minor additions of Cu (<0.5 wt.%) into the Mg₂Zn (in wt.%) system improves the corrosion resistance and tensile properties of the alloy, but higher addition levels are detrimental to both corrosion and tensile performance due to the increased volume fraction of secondary phases [145]. Liu et al. [146] and our recent study [147] have demonstrated that a small addition of Ge (\leq 0.5 wt.%) significantly improves the corrosion resistance and tensile strength of binary Mg-Zn alloys. Furthermore, the presence of Ge suppresses the kinetics of cathodic reactions and facilitates the incorporation of alloying elements into the corrosion product layer, which are beneficial for the corrosion resistance of Mg-Zn alloys. However, the amount of related work is too small to give a comprehensive overview.

3.2. Influence of Environment on the Corrosion Behavior

In addition to the galvanic coupling between secondary phases and the Mg matrix (influence of microstructure), the corrosion behavior of Mg alloys is also governed by surface product layers and their protective properties, which are significantly affected by the environment. Fang et al. [73] have studied the corrosion behavior of Mg₁Zn_xCa ($x = 0.2, 0.5, 0.8, 1.0$; wt.%) alloys in SBF and 3.5 wt.% NaCl solutions, which reveals that Mg₁Zn_{0.8}Ca alloy is the most corrosion-resistant alloy in 3.5 wt.% NaCl solution, while Mg₁Zn_{0.5}Ca alloy has the best corrosion properties in SBF, demonstrating that the corrosion properties of the alloys are significantly influenced by the compositions of the corrosive media.

It is well known that the surface film formed on Mg alloys in aqueous solution is mainly composed of magnesium oxide (MgO) and Mg(OH)₂, and the film can be easily broken down by the penetration of chloride ions (Cl⁻) [1]. Zhao et al. [119] have studied the corrosion behavior of ZE41 alloy in NaCl solutions at different pH and Cl⁻ concentrations. The incubation period to the onset of corrosion is shortened as pH decreases or Cl⁻ concentration increases. This is because corrosion predominantly happens at the uncovered regions or defects of the surface film, and the fraction of film-free surface of the alloy increases with decreasing pH and increasing Cl⁻ concentration. This phenomenon has been further confirmed by Johnston et al. [148] and Taltavull et al. [149], who investigate the corrosion behavior of ZE41 alloy in Hanks' solution at different pH and Cl⁻ concentrations buffered with bicarbonate. A more stable and thicker Mg(OH)₂ layer could be formed with increasing pH, since higher pH values mean that Mg(OH)₂ can precipitate at a lower magnesium ion (Mg²⁺) concentration. The breakdown of the surface layer induced by Cl⁻ subsequently accelerates galvanic corrosion between the constituencies in the alloy.

Very few corrosion studies of Mg-Zn based alloys have been carried out in other salt solutions, such as sodium sulfate (Na₂SO₄) and ammonium nitrate (NH₄NO₃) solutions. The limited studies show that the corrosion rate of ZE41 alloy in Na₂SO₄ solution increases with increased concentration of Na₂SO₄ at each pH, and decreases with increased pH at each concentration of Na₂SO₄ [150]. In

mixed solutions of NaCl and Na₂SO₄, the increased concentration of Na₂SO₄ also leads to a higher corrosion rate of ZE41 alloy [117]. Mg_{2.03}Zn_{0.83}Mn (in wt.%) alloy is more corrosion-resistant in 0.01 M Na₂SO₄ solution than in 0.01 M NH₄NO₃ solution [151]. As such, much more research is needed in order to get more general influence of those salt solutions on the corrosion behavior of Mg-Zn based alloys, and the application background should be specified when the corrosion of Mg-Zn based alloys is discussed or investigated.

In addition to immersion tests in salt solutions, salt spray tests are also commonly used to evaluate the corrosion resistance of Mg alloys. Under salt spray conditions, weight loss of Mg alloys is lower, and the pits formed on the sample surface are fewer and grow more slowly [152]. Generally, salt spray atmosphere is less deleterious in terms of general and pitting corrosion compared with solution immersion environments. The differences between salt spray tests and immersion tests come from the fact that a thin solution layer can be formed on the sample surface in salt spray tests, which can be considered as a stagnation, and subsequently results in rapid increase of local pH as Mg dissolves, whereas the immersion environment favors the diffusion of dissolved Mg ions, as well as the formation and growth of pits [152–154]. Therefore, interrupted salt spray and alternate immersion tests are suggested to comment on the normal corrosion of Mg-Zn alloys [57].

Direct comparison between the corrosion rates obtained from the two tests would not always be possible, since different concentrations of salt are usually used for each testing environment. Cao et al. [57] have tested the corrosion behavior of as-cast and heat-treated Mg₅Zn (in wt.%) alloys in 3.5 wt.% NaCl solution saturated with Mg(OH)₂ at room temperature, as well as in spray of 5 wt.% NaCl solution at 35 °C. The general trend of corrosion rates is the same in the two kinds of tests. Corrosion rates of Mg₅Zn alloys measured by weight loss after immersion and salt spray tests are comparable, and both of those two tests have demonstrated that heat treatment can improve the corrosion resistance of Mg₅Zn alloy. Moreover, the corroded morphologies of Mg₅Zn alloy are similar after immersion and salt spray tests. Zhao et al. [155] have studied the corrosion of ZE41 alloy in interrupted salt spray and solution immersion tests with 3 wt.% NaCl. When the interrupted salt spray period is 1 min for salt spray and 119 min for drying at 20 % humid conditions (duration for one week), the corrosion rate of ZE41 alloy is similar to the steady state corrosion rate in the solution immersion test. However, when the procedure is changed to be 15 min for salt spray and 105 min for drying (duration for 1 d), the corrosion rate of ZE41 alloy measured in interrupted salt spray tests is significantly lower than that measured in solution immersion for 1 day, revealing the importance of salt spray intervals to the corrosion tests of alloys.

In contrast to simple salt solutions, a variety of different corrosion products (e.g., calcium carbonate (CaCO₃), carbonated calcium phosphates (Ca₁₀(PO₄)₆(OH)₆ or Ca₃(PO₄)₂·3H₂O), hydroxyapatite (HA), etc.) are formed on the surfaces of Mg alloys exposed to complex electrolytes, such as SBF. Usually, a simulated body solution contains appropriate inorganic components, a buffering system, and/or organic ingredients. Ringer's solution, Hanks' solution, phosphate-buffered saline (PBS), SBF, Dulbecco's modified Eagles medium (DMEM), Earle's balanced salt solution (EBSS), and minimum essential media (MEM) are frequently used for the *in vitro* investigation of the corrosion behavior of Mg alloys [46,52,113,126]. The typical chemical compositions of those simulated body fluids are listed in Table 2. The corrosion behavior of Mg alloys differs when different simulated body fluids are used due to the different compositions of the fluids and different corrosion products formed. In particular, the use and type of buffering agent plays a particularly significant role in determining the type of corrosion product formed [9,156]. For example, the corrosion resistance of ZK60 alloy in Hanks' solution is higher than in DMEM and DMEM + fetal bovine serum (FBS). In DMEM+FBS, the corrosion resistance of ZK60 alloy is the lowest compared to that in Hanks' solution and DMEM. The lower content of hydrocarbonate, as well as the absence of organic components in Hanks' solution, results in less protective corrosion products on the surface and the consequent faster corrosion occurring on ZK60 alloy. Additionally, in the presence of FBS, the interaction between proteins and corrosion products may affect the equilibrium of dissolution and regeneration of corrosion products, thus accelerating

the corrosion of the alloy [126]. Jamesh et al. [124] have reported that the corrosion products formed on ZK60 alloy surface are $\text{Ca}_{10}(\text{PO}_4)_6(\text{OH})_6$, $\text{Ca}_3(\text{PO}_4)_2 \cdot 3\text{H}_2\text{O}$, and $\text{Mg}(\text{OH})_2$ in SBF, while CaCO_3 and $\text{Mg}(\text{OH})_2$ predominate in the case of Ringer's solution. In addition, much more severe pitting and localized corrosion occurs on ZK60 samples immersed in SBF. Zander et al. [75] have further demonstrated that the influence of Zn content on the corrosion resistance of Mg-Zn-Ca alloys is more significant in Hank's solution than in PBS, as indicated by the anodic polarization curves measured in Hanks' solution.

Table 2. The typical chemical compositions of simulated body fluids (in mM/L if not specified).

Ingredient	Ringer's Solution	Hanks' Solution	DMEM	EBSS	SBF	PBS	MEM	Blood Plasma
Mg^{2+}	-	0.8	0.81	0.4	1	-	0.4	1
Na^+	156	142	154	144	142	153	143	140
K^+	5.8	5.8	6.24	5.4	5	5	5.4	5
Ca^{2+}	2.2	2.5	1.8	1.8	2.5	-	1.8	2.5
Cl^-	164	145	118	125	109	140	125	100
HCO_3^-	2.4	4.2	44.05	26	27	-	26	22–30
H_2PO_4^-	-	0.4	1.04	1	-	2	0.9	0.8
HPO_4^{2-}	-	0.3	-	-	1	8	-	-
SO_4^{2-}	-	0.8	0.81	0.4	1	-	0.4	0.5
Glucose	-	-	5.55	5.6	-	-	5.6	5
Amino acid (g/L)	-	-	11.01 (mM/L)	-	-	-	0.95	Variable
Proteins (g/L)	-	-	-	-	-	-	-	35–50
Vitamins (mg/L)	-	-	-	-	-	-	8.1	Variable
Phenol red	-	-	-	0.03	-	-	0.03	-
Refs.	[51]	[113]	[126]	[157]	[158]	[158]	[157]	[157]

Normally, the corrosion rate of Mg alloy in vivo is around 1–5 times lower than that obtained in vitro [159]. For example, the corrosion rate of as-cast $\text{Mg}_3\text{Zn}_{1.34}\text{Ca}$ (in wt.%) alloy in MEM is 4.718 mm/year, whilst that measured in vivo implanted in Lewis rats is only 0.786 mm/year after immersion or implantation for 7 d [157]. However, opposite results have also been reported. Extruded Mg_6Zn corrodes faster in vivo (2.32 mm/year) than in SBF (average at 0.14 mm/year) [160]. As indicated in Table 2, the lower concentration of Cl^- in blood plasma (100 mM/L), compared to simulated physiological solutions such as Hank's solution (145 mM/L), generally contributes to slower corrosion of Mg alloy in vivo than in vitro. Additionally, the possible interaction between the complicated components in vivo (e.g., cells and proteins) and Mg may also contribute to the lower corrosion rate measured in vivo [157,159,161]. As already suggested by many researchers [157,162–164], much caution should be paid when choosing the appropriate simulated body fluid to evaluate the corrosion rates of Mg-Zn alloys in vitro to get results comparable to those in vivo.

The behavior of Mg alloys in aggressive environments under dynamic loading, including stress corrosion cracking (SCC) (applied tensile mechanical loading) and corrosion fatigue (CF) (applied cyclic loading), is also a critical concern for their applications. The combined action of stress and corrosive electrolytes can result in an unexpected premature failure of alloys at a loading below the designed value for static loading service conditions [165]. Generally, the corrosion rates of Mg alloys are significantly higher in corrosion fatigue tests than those measured in static immersion. The corrosion product layers can be broken due to the cyclic loading or the strain induced, which consequently promotes the penetration of corrosive electrolytes into the underlying metals and the occurrence of corrosion [166]. Furthermore, the corrosion rates of Mg alloys increase with increasing cyclic loading. Bian et al. [167] have studied the corrosion behavior of extruded $\text{Mg}_2\text{Zn}_{0.2}\text{Ca}$ (in wt.%) alloy in SBF under static conditions and cyclic loading, revealing the effect of cyclic loading on the corrosion rate of the alloy mentioned above (Figure 8b). Moreover, it has been pointed out that a material that corroded more slowly in static immersion may exhibit a faster corrosion rate under cyclic loading conditions.

This finding is often attributed to the stress-accumulating role of intermetallics due to the evolution of hydrogen at these locations. SCC of Mg alloys, which can occur in either the presence or absence of Cl^- [168], is often associated with hydrogen embrittlement. Under tensile loading in a corrosive environment, the rupture of surface film can be induced by an applied stress or localized corrosion, and can facilitate the initiation of cracks. This, in turn, allows the diffusion of hydrogen into the material [169,170]. The strain rate plays a critical role in the failure of alloys. Fast strain rate results in failure via mechanical overload as opposed to SCC. However, low strain rate increases the contact time of the alloy with the corrosive medium, thus facilitating the penetration of the electrolyte and the ingress of hydrogen [171]. Additionally, SCC can even occur in the presence of residual stress that accumulates during thermal–mechanical processing without externally applied stress. Jadari et al. [172] have observed that the fracture morphologies of extruded Mg2Zn1Zr (in wt.%) alloy, immersed in modified simulated body fluid (m-SBF) and then strained in air, are similar to those strained directly in m-SBF. The SCC of the pre-immersion sample is ascribed to the residual stress developed during the extrusion processing.

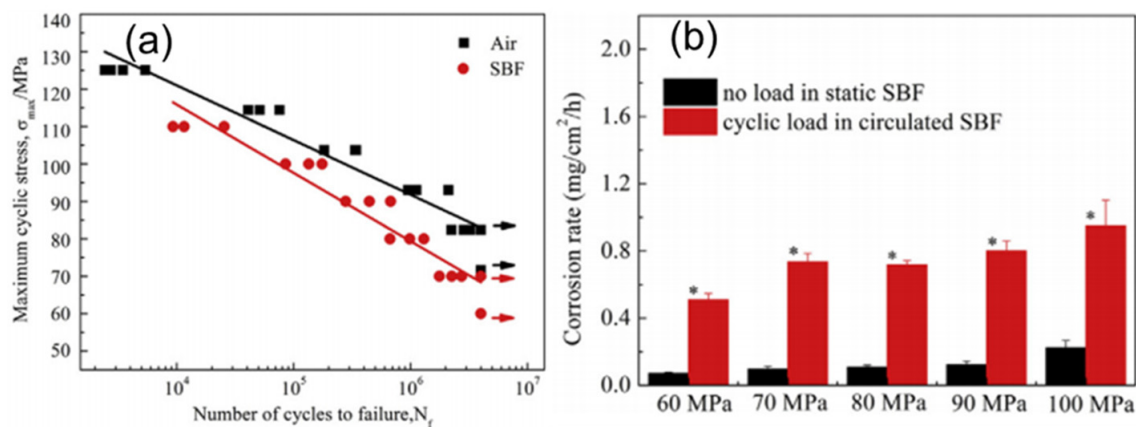


Figure 8. (a) Stress-life (S-N) curve of Mg2Zn0.2Ca alloy in air and in simulated body fluid (SBF). (b) Corrosion rate of Mg2Zn0.2Ca alloy measured in static SBF (static immersion) and under a cyclic loading in circulating SBF [167] (with permission from Elsevier and Copyright Clearance Center).

3.3. Influence of Processing

The influence of thermal and mechanical processing on corrosion and mechanical properties of Mg-Zn-X alloys is closely associated with the grain size and the distribution of precipitates within the microstructure. This results in significant differences in the performance compared to as-cast alloys.

Solid solution heat treatment is beneficial to the corrosion resistance of Mg-Zn-X alloys, especially when conducted at high temperatures or for relatively long time periods. Some secondary phases—for example, MgZn binary phase—could dissolve into the Mg matrix during solution treatment. Thus, dendrite structures would disappear, resulting in the formation of a homogenized microstructure [70,173,174]. With the decrease of volume fraction of secondary phases, micro-galvanic corrosion is reduced; thus, the corrosion resistance of the alloys is improved. However, solution treatment can increase grain size, which could decrease corrosion resistance of Mg-Zn-X alloys when the effect of grain size overwhelms that of secondary phases on corrosion of Mg-Zn-X alloys [70]. In contrast, aging treatments facilitate the precipitation of secondary phases [58,142,173,175]. For example, rod-like metastable MgZn₂ secondary phases would precipitate both at the grain boundaries and inside the grains, inducing enhanced strength of the alloy due to the strengthening effect of this phase. With the increase of ageing time, the average volume fraction of precipitates increases. Guan et al. [142] have studied the development of microstructure and mechanical properties of rolled Mg4Zn1Sr (in wt.%) alloy with different aging times (0–16 h). The hardness, ultimate tensile strength, and elongation to fracture of Mg4Zn1Sr alloy increased as aging time increased, and reached their

maximum after aging for 8 h at 175 °C. This was attributed to the strengthening effect of the precipitated rod-like transition MgZn_2 phase. However, with further increase in aging time, the volume of rod-like MgZn_2 phases decreases, while the amount of particle-like flaky MgZn_2 phase and stable MgZn phase, which weaken the strengthening effect, increases. Therefore, mechanical properties of the alloy start to decrease. Ibrahim et al. [176] have also confirmed the influence of aging time on the microstructure and mechanical properties of Mg-Zn-Ca alloy. They have studied the microstructural, mechanical, and corrosion characteristics of Mg1.2Zn0.5Ca (in wt.%) alloy after solid solution treatment and with further aging treatment for different time. It has been demonstrated that when the age hardening duration increases to 2–5 h, both the mechanical properties and corrosion resistance of Mg1.2Zn0.5Ca alloy strengthen because of the refined microstructure and finely distributed $\text{Mg}_6\text{Ca}_2\text{Zn}_3$ precipitates. Further increases in aging time did not contribute to further enhancement of either mechanical or corrosion properties.

Wrought processing can introduce several effects, such as grain refinement and texture, conferring specific improved properties to Mg alloys. Extrusion treatment induces severe plastic deformation, simultaneously refines α -Mg grains by dynamic recrystallization, and produces highly dispersed precipitates. The refined microstructure is beneficial for the improvement of the corrosion resistance of Mg-Zn-X alloys [6,126]. Moreover, the tensile strength and ductility of Mg-Zn-X alloys can be enhanced by grain refinement strengthening, solid solution strengthening, and secondary phase strengthening during the extrusion process [6,16,96,160,177]. Extrusion parameters, such as extrusion temperature, speed, and ratio, have a significant influence on the microstructure and mechanical properties of Mg-Zn-X alloys (Figure 9). In general, with the increase of extrusion temperature, ratio, and speed, average grain size and area fraction of dynamic recrystallized (DRXed) grains increase. This is because the deformation heating, which occurs during the extrusion process, results in rise of temperature at the deformation zone. Concomitantly, the ultimate strength and yield strength decrease due to the coarsened microstructure [86,173,178–180]. Formation of precipitates also increases with elevated extrusion temperature because the diffusion of solute atoms is faster at higher temperatures [173,181]. However, the influence of extrusion temperature on the plastic deformation of Mg-Zn-X alloys is still under debate. Park et al. [179] and Zeng et al. [180] have reported increased elongation to fracture of $\text{MgZn}(\text{Mn})\text{Ce}/\text{Gd}$ and MgZnYZr alloys with increased extrusion temperature, while the relationship was reversed in the case of MgZnHo [178] and MgZnGd alloys [173]. Park et al. attribute the increased ductility of $\text{MgZn}(\text{Mn})\text{Ce}/\text{Gd}$ alloys to the suppression of {10-11}-{10-12} double twinning with increased area fraction of DRXed.

It is believed that a weaker or non-basal texture is beneficial to the improvement of ductility of Mg sheets at room temperature, since the majority of grains in weaker basal or non-basal textures favor dislocation glide on the basal plane [182–184]. To control the texture, many processing technologies have been applied to Mg alloys. Rolling processes have been shown to be more effective in developing weaker or non-basal textures in Mg alloys compared with continuous extrusion, torsion extrusion, and equal channel angular extrusion [185]. The refined microstructure and uniformly dispersed fine secondary phases, formed during the rolling processing, contribute to enhanced yield strength and elongation to fracture of Mg-Zn-X alloys [101]. Lee et al. [186] have compared the recrystallization behavior of hot-rolled Mg3Zn0.5Ca alloy with that of hot-rolled Mg3Al1Zn alloy (both in wt.%). The results showed a totally different twins formation mode in Mg3Zn0.5Ca and Mg3Al1Zn alloys. Both compressive and secondary twins are generated in Mg3Zn0.5Ca alloy, while only tensile twins are observed in Mg3Al1Zn alloy. The presence of compressive and secondary twins leads to a weaker basal texture evolution in the Mg3Zn0.5Ca sheet. As a result, the hot-rolled Mg3Zn0.5Ca alloy exhibits much better formability than hot-rolled Mg3Al1Zn alloy. The influences of rolling on the corrosion properties of Mg-Zn-X alloys are not widely studied. The increase of grain boundary area due to significantly refined microstructure after rolling can decrease the corrosion resistance of Mg3.0Zn (in wt.%) alloy in SBF [187].

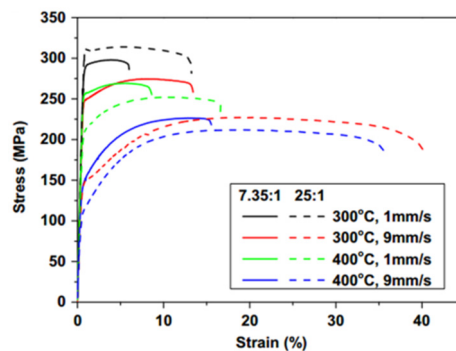
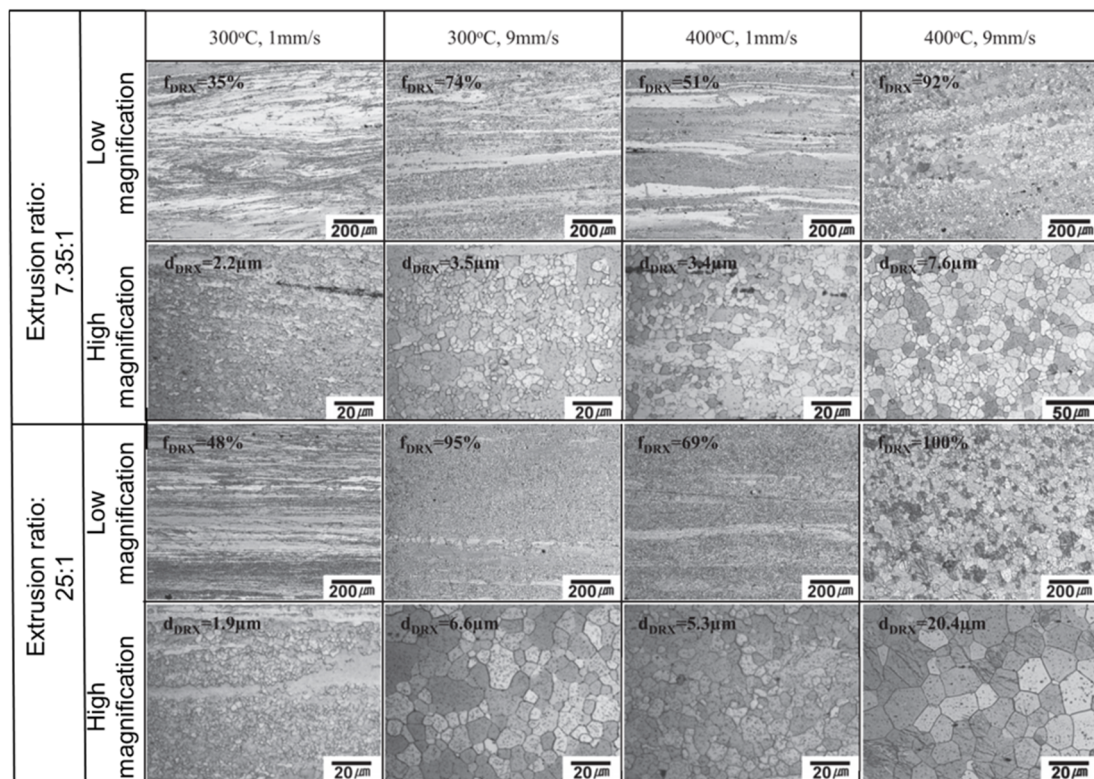


Figure 9. Effect of extrusion parameters (extrusion speed, ratio, and temperature) on the microstructure and mechanical properties of Mg₂Zn₁Mn_{0.5}Ce alloy (in wt.%) (f_{DRX} : Area fraction of the recrystallized grains, d_{DRX} : Grain size of the recrystallized grains) [179] (with permission from Elsevier and Copyright Clearance Center).

Equal channel angular pressing (ECAP), which induces severe plastic deformation (SPD) by introducing an extremely large strain, is one of the most effective processing techniques for fabricating ultrafine-grained (UFG) Mg alloys. Compared with conventionally processed Mg alloys, ECAPed Mg alloys exhibit improved corrosion resistance and excellent mechanical properties [188–193]. Jiang et al. [188] have studied the influence of ECAP pass number on the corrosion resistance of as-cast ZE41A alloy in NaCl solution. Higher ECAP passes endow UFG ZE41A alloy with better corrosion resistance. The corrosion product layers formed on ECAPed ZE41A alloy, which has undergone 60 passes, are free of cracks compared to those formed on the ECAPed alloy surfaces with fewer passes. This can be explained by the decreased residual internal stress of the alloy, resulting from the complete DRX of the deformed microstructure formed after a high number of ECAP passes. ECAP processing of extruded ZK60 alloy is also beneficial for the reduction of the corrosion rate of the alloy in PBS solution [189]. The refinement and redistribution of precipitates during the ECAP process lead to a remarkable change in corrosion behavior from a localized to a more uniform mode. However,

the influence of ECAP processing on the mechanical properties of Mg-Zn-X alloys differs with the initial conditions of the alloys. Zheng et al. [190] have compared the mechanical properties of as-cast and extruded Mg5Zn0.9Y0.2Zr (in wt.%) alloys after different passes of ECAP processing. Both the strength and elongation to fracture of as-cast Mg5Zn0.9Y0.2Zr alloy are significantly enhanced after ECAP processing, especially after an increased number of ECAP passes. This is attributed to the uniformly dispersed I-phase and refined grains formed during recrystallization. In contrast, for extruded Mg5Zn0.9Y0.2Zr alloy, the grain size is further refined after ECAP and the ductility is improved, while both yield strength and ultimate strength are reduced. This trend, also confirmed by other researchers [189,191,192], does not follow the Hall–Petch relation. It is explained by the intensive development of texture during ECAP. ECAP processing routes (shown in Figure 10), regarding the rotation of the billet between each pass, also have significant influence on the microstructure and mechanical properties of Mg alloys [193]. Route B_c (Figure 10b) is the most effective way to refine grains, while route A is the least effective one. The different strain paths can also result in different textures. Processing as route C would lead to the strongest texture of the alloys, with high-intensity basal planes inclining about 45° to the extrusion direction. As a result of the competition between grain refinement strengthening and texture softening effect, both yield strength and ultimate tensile strength of extruded Mg5.25Zn0.6Ca (in wt.%) alloy processed by ECAP with routes A and B_c increase, but decrease with route C.

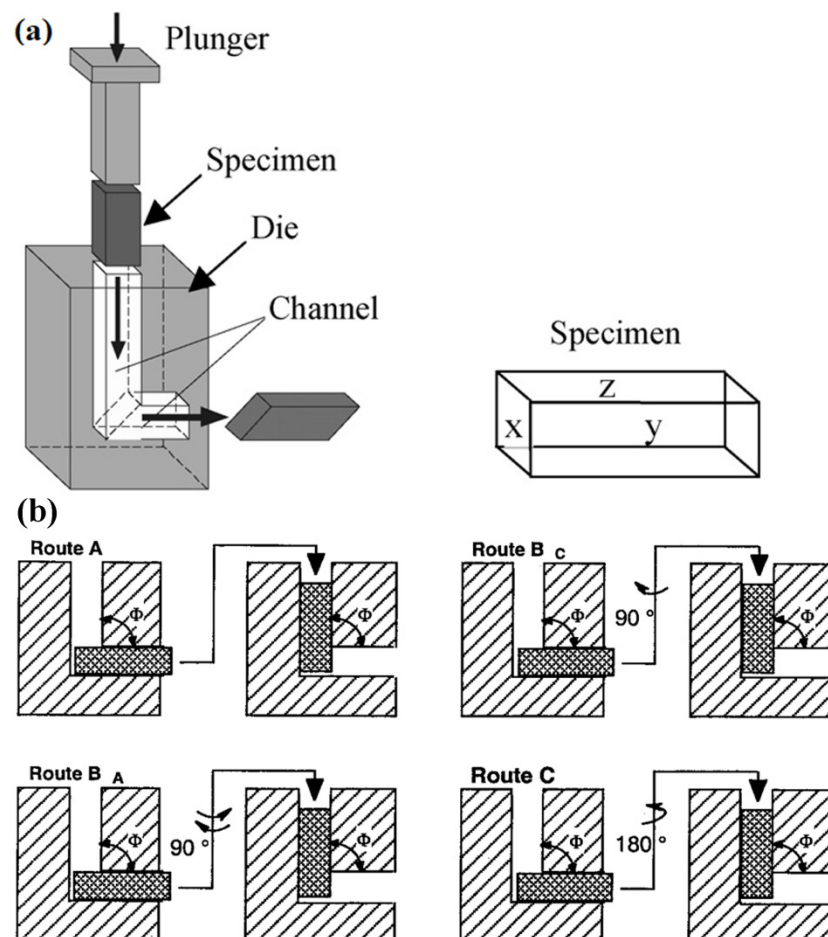


Figure 10. Schematic illustration for (a) equal channel angular pressing (ECAP) processing and (b) the rotation schemes for four ECAP routes [193,194] (with permission from Elsevier and Copyright Clearance Center).

4. Strategy to Improve Properties of Mg-Zn Based Alloys

In the previous chapters, it was demonstrated how alloying additions and thermal–mechanical treatments can be used to meet the requirements of different applications and expand the application field. However, microstructure adjustment by phase composition and unconventional fabrication approaches can also improve the corrosion performance and mechanical properties of Mg-Zn based alloys. Furthermore, surface treatment is effective for tailoring surface properties and corrosion resistance.

4.1. Microstructure Adjustment by Phase Composition

4.1.1. Magnesium-Based Metal Matrix Composites

Magnesium-based metal matrix composites (MMCs) have high specific stiffness and strength both at room and elevated temperature, as well as improved damping capacity and wear resistance compared to the conventional alloys. The fabrication of MMCs has been considered as an approach to tailor the corrosion rate of Mg alloys with enhanced mechanical properties. Therefore, they have attracted considerable attention as high-performance structural materials for applications in the automotive and aerospace industries [195–197]. Nunez-Lopez et al. [198,199] have studied the corrosion behavior of Mg-Zn-Cu (ZC71)/SiC_p (silicon carbide particles) metal matrix composite in salt spray tests at 25 °C, particularly the micro-galvanic corrosion between the reinforcement and the matrix. Compared with conventional ZC71 alloy, the local penetration rate recorded for ZC71/SiC_p composites is about three times higher, which is due to the formation of less protective corrosion products. However, the maximum depth of corrosion attack in the salt spray test is the greatest for extruded ZC71 alloy, which is believed to be a result of the more uniform distribution of eutectic Mg(Zn, Cu)₂ phases in the composite. This uniform distribution is ascribed to the effective nucleation sites of SiC_p for precipitation of eutectic Mg(Zn, Cu)₂ phases. Additionally, no galvanic corrosion is detected in the vicinity of the reinforcement particles. Difficulty in forming protective corrosion product layers on SiC_p/ZK80A and SiC_p/ZK60A composites has also been revealed by Zucchi et al. using electrochemical impedance spectroscopy [200]. Nevertheless, dense corrosion product (Mg(OH)₂) layers can be formed on the surfaces of calcium-polyphosphate-reinforced ZK60A composites [201]. Compared with the porous and plate-like crystalline morphology of the Mg(OH)₂ formed on the surface of conventional ZK60A alloy, dense and plate-like Mg(OH)₂ is formed on the surface of the composite. This dense layer significantly slows down the corrosion of the composite. Nieh et al. [202] have reported superplasticity of a ZK60A composite reinforced by 17 vol.% SiC particles, with an elongation to failure of up to 350% at a very high strain rate of about 1 s⁻¹, which is due to the refined grain size of about 0.5 μm. The presence of fine SiC particles contributes to the refinement and stabilization of the microstructure of the composites at elevated temperature. Hu et al. [203] have also fabricated ZK51A matrix composites reinforced by SiC whiskers (SiC_w) using a two-step squeeze casting process. The modulus and mechanical strength increase compared with unreinforced ZK51A alloy. Particularly, the increase in 0.2% offset yield strength and modulus of the composite is linearly proportional to the volume fraction of SiC_w in the range of 0–0.2, demonstrating the load transfer strengthening mechanism. The adjustment of mechanical properties and corrosion rates of MMCs by choosing appropriate composites, such as HA [204,205], β-tricalcium phosphate (β-TCP) [206], and poly-L-lactic acid (PLLA) [207], also confers great potential as biomaterial candidates on MMCs. Yu et al. [208] have investigated the in vitro and in vivo degradation behavior of β-Ca₃(PO₄)₂/Mg6Zn (wt.%) composites in SBF and rabbits, respectively. The corrosion rate of 10% β-Ca₃(PO₄)₂/Mg6Zn composites significantly decreases compared with Mg6Zn alloy fabricated with the same processing route. This is explained by the decomposition of β-Ca₃(PO₄)₂ that favored the formation of protective insoluble phosphates and carbonates on the composite surfaces during immersion. Furthermore, in vivo tests indicate that the composites improve the concrescence of pre-broken bone tissues and

exhibit good biocompatibility with vital organs like the hearts, livers, and kidneys of rabbits, even in the presence of hydrogen bubbles.

4.1.2. Magnesium Bulk Metallic Glasses

Magnesium bulk metallic glasses (BMGs), especially Mg-Zn-Ca glassy alloys, have been extensively studied as biodegradable materials. Their single-phase and chemically homogenous microstructures are beneficial for the improvement of both corrosion resistance and mechanical properties of Mg alloys [209]. The specific strength of Mg-Zn-Ca alloy in glass state ($250\text{--}300\text{ MPa cm}^3/\text{g}$) can be about 40% higher than those of traditional crystalline Mg alloys (around $220\text{ MPa cm}^3/\text{g}$ for die-casting AZ91D alloy) [210]. Gu et al. [211] have assessed the corrosion behavior of $\text{Mg}_{66}\text{Zn}_{30}\text{Ca}_4$ and $\text{Mg}_{70}\text{Zn}_{25}\text{Ca}_5$ (both in at.%) BMGs, and have revealed that the corrosion rate decreases compared to some previously reported Mg alloys, such as as-cast AZ91 alloy and as-rolled pure Mg. This was attributed to the absence of secondary phases in BMGs, which can induce galvanic corrosion and the dense corrosion products containing zinc oxide/hydroxide forming on Mg-Zn-Ca BMGs. Due to the absence of crystal slip systems in Mg-Zn-Ca BMGs, the single-phase and chemically homogeneous nature also results in a three-times-higher compressive strength compared to as-rolled pure Mg. Moreover, the cytocompatibility is improved, and good adherence and growth of MG63 cells occur on the Mg-Zn-Ca BMGs surface. However, glassy Mg-Zn-Ca alloys are extraordinarily brittle at room temperature, and the fabrication of BMGs usually requires high-purity raw materials to guarantee glass-forming ability (GFA). Wang et al. [209] have successfully synthesized $\text{Mg}_{69}\text{Zn}_{27}\text{Ca}_4$ (in at.%) glassy alloy reinforced by ductile Fe particles by using industrial raw metallic elements. The GFA decreases due to the addition of Fe with the formation of ductile $\alpha\text{-Mg}$ and dendrite MgZn phases. Nevertheless, the compressive strength and fracture strain are enhanced.

4.2. Microstructure Adjustment by Production Technique

4.2.1. Squeeze Casting

Squeeze casting is a metal fabrication process in which the solidification of molten metal is accelerated by applying high pressure. It combines permanent mold casting with die forging. Compared with conventional casting process, such as die-casting, gravity casting or sand casting, squeeze casting processing can produce Mg alloys with finer microstructure, less porosity, longer die-life, and reduced microshrinkage. These merits confer both better corrosion resistance and mechanical properties on alloys fabricated by squeeze casting [212,213]. Mo et al. [214] have compared the microstructures and mechanical properties of $\text{Mg}_{12}\text{Zn}_4\text{Al}_{0.5}\text{Ca}$ (in wt.%) alloys fabricated by gravity and squeeze casting. The applied pressure used during squeeze casting limits the formation of shrinkage porosity. The refined microstructure obtained during the squeeze-cast process contributes to improved mechanical properties of components compared to those produced by gravity casting. The influence of squeeze casting processing parameters, such as pouring temperature, applied pressure, and dwell time, has also been investigated. Increasing applied pressure and dwell time (just before the ending of solidification) refine microstructure and promote cast densification, which consequently improves the mechanical properties of the alloy. However, as pouring temperature increases, cast densification is promoted and grain size is coarsened, which leads first to an increase, then to a decrease of the mechanical properties. The study of Doležal et al. [215] on $\text{Mg}_3\text{Zn}_2\text{Ca}$ (in wt.%) alloy has also confirmed the grain refinement and the enhanced mechanical properties of Mg-Zn alloys produced by squeeze casting compared with those produced by gravity casting. Moreover, subsequent aging treatment can further improve the ultimate tensile strength and elongation to fracture due to the homogenization of microstructure.

4.2.2. Twin-Roll Casting

Twin-roll casting (TRC) processing reduces several production steps compared to the conventional production techniques by combining casting and hot rolling into a single step. This reduces manufacturing costs for commercial weight-saving applications of wrought Mg alloys. It has been revealed that TRC processing can provide much faster solidification speed, refine grain size, homogenize the microstructure, and reduce, or even remove, segregation of alloying elements [216–220]. Moreover, the basal texture can be reduced when Mg alloys are fabricated by TRC processing compared to the strong basal texture developed in hot rolling. Little attention has been paid to the corrosion behavior of Mg alloys fabricated by twin-roll casting. Oktay et al. [221] have compared the corrosion behavior of AZ31 sheets produced by twin-roll casting and conventional direct chill casting + rolling in 0.01 M NaCl and 0.5 M Na₂SO₄ solutions. The higher solidification rate during twin-roll casting results in much smaller and more homogeneously distributed secondary phases in the alloy, which contributes to a slightly higher corrosion resistance of TRC AZ31 alloy in both Na₂SO₄ and NaCl solutions. Mg alloys produced by TRC have comparable or better mechanical properties to those of Mg alloys sheets produced by conventional ingot casting and subsequent hot rolling, but a better combination of yield strength and fracture elongation [222,223]. Park et al. [224] have compared the high-temperature superplastic deformation behavior of TRC-prepared Mg₆Zn₁Mn₁Al (ZMA611) (in wt.%) and ingot cast AZ31 alloys. The TRC ZMA611 alloy exhibits larger fracture elongation than ingot cast AZ31 alloy at all testing temperatures and strain rates, which is caused by the presence of thermally stable Al₈Mn₅ dispersoid particles. Hou et al. [225] have compared the degradability and mechanical integrity of a TRC Mg_{0.7}Zn_{0.6}Ca alloy (in wt.%) before and after annealing. The results show that the residual strain and deformation twins restored in the as-rolled alloy lead to a slightly higher corrosion rate than that of the annealed one. For both alloys, sufficient mechanical support still exists after immersion in α-MEM + 10 % FBS for up to 42 days, with a residual YS and UTS that are more than 85% those of the pristine states. With further minor (0.1 wt.%) addition of Zr [226,227], the sheet exhibits excellent stretch formability at room temperature, slow corrosion rate (<0.25 mm/year, determined by a neutral salt spray test at room temperature), and a widely adjustable strength level (YS = 130–260 MPa, UTS = 210–300 MPa), which shows great potential in applications as both structural and biomedical materials.

4.2.3. Rapid Solidification

Compared with conventional ingot metallurgy (I/M), rapid solidification (RS) processing confers better corrosion and mechanical properties to Mg parts due to the refinement of grain and precipitate sizes, the extended solid solubility of alloying elements, and the homogeneous microstructure [228,229]. Zhang et al. [111] have compared the corrosion resistance (Figure 11) and mechanical properties of Mg₆Zn₁Mn (in wt.%) alloy fabricated by conventional casting and rapid solidification. In comparison to the formation of coarse dendrite cells (about 200 μm) in as-cast Mg₆Zn₁Mn alloy, extremely small dendrites with an average size of about 25 μm are formed in rapid solidification. The refinement of the dendritic microstructure consequently decreases the corrosion rate of Mg₆Zn₁Mn alloy in 3.5 wt.% NaCl solution by approximately one order of magnitude, and increases the ultimate strength from 335 MPa to 460 MPa. Xu et al. [230] have studied the influence of solidification rate on the microstructure and corrosion resistance of Mg₂₀Zn₁Ca (in wt.%) alloy. They have found that the grain size and precipitate size decrease with increased cooling rate. A continuous 3D network of secondary phases is formed under a cooling rate of 3000 °C/min. Moreover, as a result of fast cooling, the contents of Zn and Ca in the Mg matrix are much higher than their equilibrium solid solubility in Mg. The supersaturations of Zn and Ca elements and the dispersed alloying elements due to homogeneous microstructure enhance the corrosion resistance of Mg₂₀Zn₁Ca alloy in PBS solution.

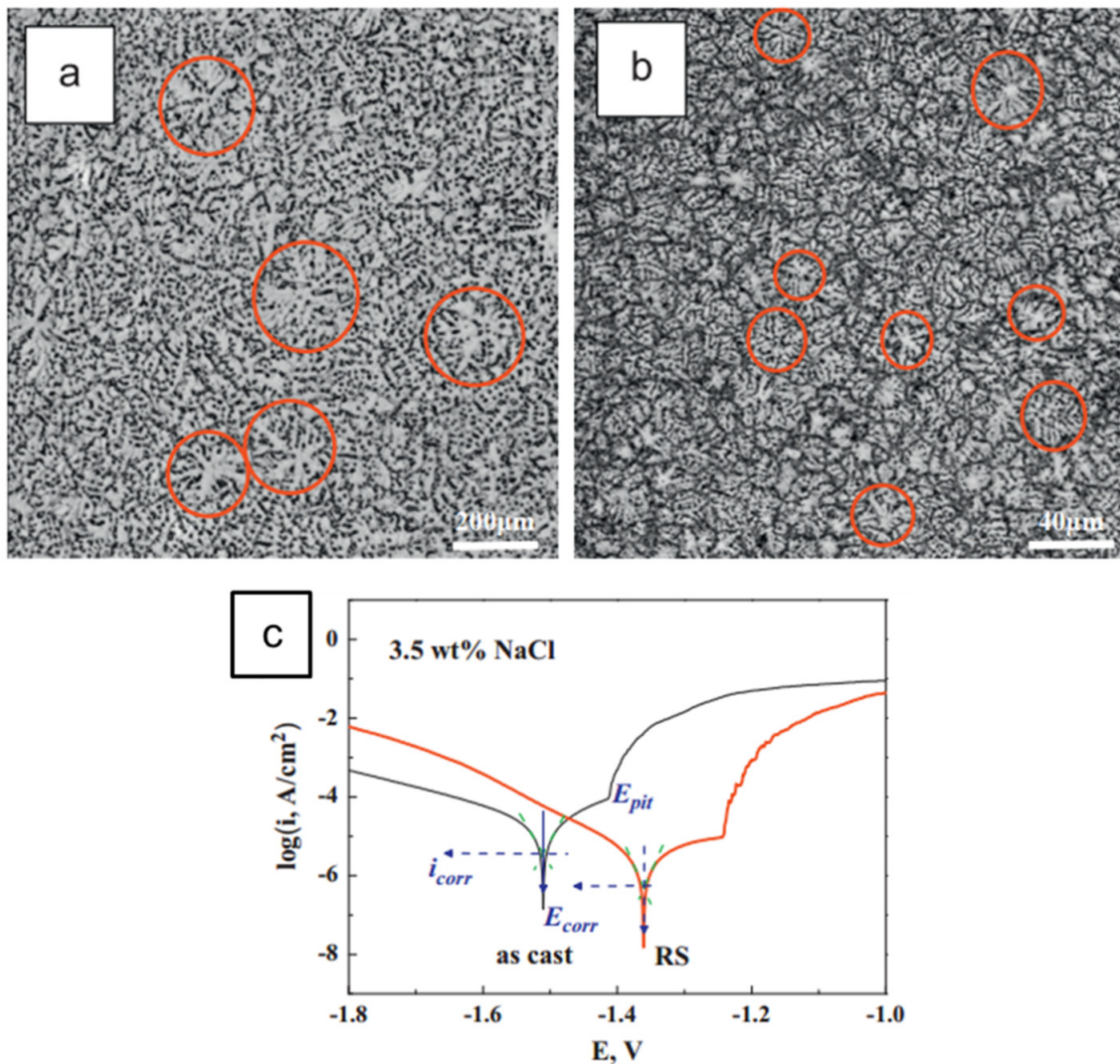


Figure 11. Comparison of the microstructure and corrosion behavior of Mg₆Zn₁Mn (in wt.%) alloy fabricated by conventional casting and rapid solidification. The microstructure of (a) as-cast and (b) rapid solidification Mg₆Zn₁Mn alloys. (c) Potentiodynamic polarization curves of Mg₆Zn₁Mn alloy in 3.5% NaCl solution [111]. (with permission from Elsevier and Copyright Clearance Center).

4.3. Surface Treatments

Modification of the surface is another very popular strategy to improve the (corrosion) properties of Mg alloys in general and Mg-Zn based alloys in particular. However, the field is wide; here, it is only intended to give a short overview of the topic. For a deeper study of the topic, a range of reviews about surface treatments of Mg alloys are available [231–239].

There are a couple of different approaches and concepts to either improving the substrate by itself (e.g., surface alloying), to coating it with a more resistant material, and/or to separating the substrate material from the surrounding. However, no coating is perfect or will survive in service forever without defects. From this point of view, the substrate corrosion resistance is still an important factor. Good substrate corrosion resistance is a requirement for minimizing reactions at the interface when diffusion of ions and water through the layer or defects take place. The formation of corrosion products (mainly hydroxide formation) can cause severe volume increase and thus stresses at the interface, leading to blistering and flaking-off of the coatings. As-cast Mg-Zn based alloys are, from this point of view, not the best choice, but the newly developed wrought alloys with much lower Zn contents and additional micro-alloying elements (e.g., Ca, Zr, etc.) do offer substrates with good corrosion resistance

and uniform corrosion without localized attack [147,226]. To guarantee good corrosion resistance, especially for wrought products, a sufficient cleaning (material removal) is the pre-requirement for any successful coating on Mg alloys. Removal of the undefined and contaminated surface oxide layer by etching has to be done, replacing it afterwards with a defined “passive” layer (conversion). The etching of Zn-rich alloys can result in Zn enrichment at the surface with problems to obtain such a uniform conversion layer. The latter is not a problem for most alloys with lower alloy content or the alloying elements in solid solution (Zn and other alloying elements < 1 wt.% each).

After cleaning, depending on the application and the required properties, a wide set of treatments/coatings are available, ranging from metals to ceramics and polymers. To deposit them on Mg, a range of coating techniques is available:

- Chemical conversion coatings
 - Chromates (restricted in use in most countries) [240]
 - Chromate-free alternatives: Phosphate-permanganate, vanadates, molybdates, stannates, tungstates, fluorozirconate/titanate, and potassium-permanganate [241–252]
- Electro-chemical coatings
 - Electroplating (Zn, Cu, Ni, Cr) [253–256]
 - Anodizing [257,258]
 - Plasma electrolytic oxidation (PEO) [259,260]
- Polymeric coatings/paints (e.g., Powder and E-Coat) and other non-metallic coatings (e.g., varnish, wax) [261–263]
- Physical techniques
 - Physical vapor deposition [264–266]
 - Plasma/laser surface treatments (alloying, cladding) [267–270]
 - Thermal/plasma spraying [271]

Currently, the most industrially used processes for corrosion protection are conversion coatings in combination with paint or polymer top coats. The conversion treatment is the base for paint application, and should create a strong interface with good adhesion to the paint. There are chromate-free conversions available, and if more adhesion and better barrier properties are required, the chemical conversion layer can be replaced by anodizing/PEO coatings. The paint/polymer top coats can range from single- to multi-layer coatings according to the requirements of the applications and severity of the environment. Such combinations are sufficient for most of today’s transport applications. The main challenge in coating development today is the integration of inhibitors into the coatings, offering release on demand, self-healing ability, and additional functionalities.

5. Applications of Mg-Zn Based Alloys

Mg-Zn based alloys have a long tradition in aerospace applications in helicopter, aircraft, and aeroengine components [272]. For example, ZE41 alloy is applied in the main transmission of Sikorsky UH60 Family (Blackhawk) and the turbofan of Pratt and Whitney Canada PW305. In addition, the tray of Rolls Royce is made from ELEKTRON ZRE1 alloy (Figure 12) [273]. In automotive applications, Mg_{4.2}Zn_{1.2}RE_{0.7}Zr (ZE41A) and Mg₆Zn_{2.7}Cu_{0.25}Mn (ZC63A) (both in wt.%) alloys have been used for functional prototypes due to the good pressure tightness of ZE41A alloy and the good elevated temperature properties of ZC63A alloy [274]. Moreover, ZK60 extruded at an extremely low extrusion rate is used for wheels and stems of racing cars and bicycles [275]. IMRA America Inc. [276] has developed a series of Mg₈Zn₅AlCa (in wt.%) alloys with a Ca content varying from 0.2 to 1.2 wt.% for automotive powertrain applications. The developed alloys showed a comparable or slightly better corrosion resistance than that of AZ91D alloy. The creep performance at 150 °C and 35 MPa was

decreased by almost one order of magnitude, while the tensile properties were comparable to or slightly better than those of AZ91D alloy. Volkswagen AG, Helmholtz-Zentrum Geesthacht, and Posco collaborated together to develop a new sheet alloy based on TRC Mg-Zn-Ca-Zr. The TRC Mg-Zn-Ca-Zr sheet reduced the forming temperatures from over 220 °C for a conventional AZ31 sheet to 160 °C, which means saving more energy and significantly simplified temperature control in a series-forming process. A tailgate was successfully produced as a demonstrator [227,277].



Figure 12. Tailgate for Volkswagen Passat utilizing a twin-roll-cast (TRC) Mg-Zn-Ca-Zr sheet [277] (pictures offered by Volkswagen. Copyright accessed).

Up to now, Mg-Zn based alloys have not been commercialized for clinical/medical applications, but a relatively high number of in vivo and in vitro studies have been carried out to investigate the feasibility of Mg-Zn based alloys as biomedical materials. He et al. [278,279] have comprehensively studied the in vitro and in vivo degradation behavior of extruded Mg6Zn (in wt.%) alloy. It exhibited better cell attachment, mineralization ability, and improved mRNA expression compared with PLLA. More importantly, considerable new bone formation is observed surrounding the implanted Mg6Zn alloy, and no adverse effect induced by hydrogen evolution is detected during the in vivo experiment. In addition, pathological analysis demonstrated that the in vivo degradation of Mg6Zn alloy did not harm the vital organs (heart, liver, kidney, and spleen) [278]. Guo et al. [60] have also studied the in vitro and in vivo histocompatibility of urinary implants made of Mg6Zn and pure Mg. The Mg6Zn alloy degrades faster than pure Mg in SBF, but exhibits better histocompatibility in the bladder compared to pure Mg after implantation for two weeks. Kraus et al. [280] have utilized online microfocus computed tomography (μ CT) (Figure 13) to observe the interaction of implant and tissue performance by implanting Mg5Zn0.25Ca0.15Mn (in wt.%) pins into a growing rat skeleton. During degradation in a physiological environment, large amounts of Mg²⁺ are released into the surrounding tissue. As a result, magnesium hydroxide is formed, which consequently facilitates the accumulation of calcium phosphates and the formation of new bone around the implanted material. Although the Mg5Zn0.25Ca0.15Mn alloy starts to degrade immediately after the implantation and generates a massive volume of hydrogen gas (about 270 mm³/d), the gas can be rapidly resorbed, and the bone recovers restitution after the complete degradation of the implanted pin. In addition, no inflammation is observed. These studies suggested that Mg-Zn based alloys have quite excellent in vivo biocompatibility and are promising candidates as biodegradable medical devices.

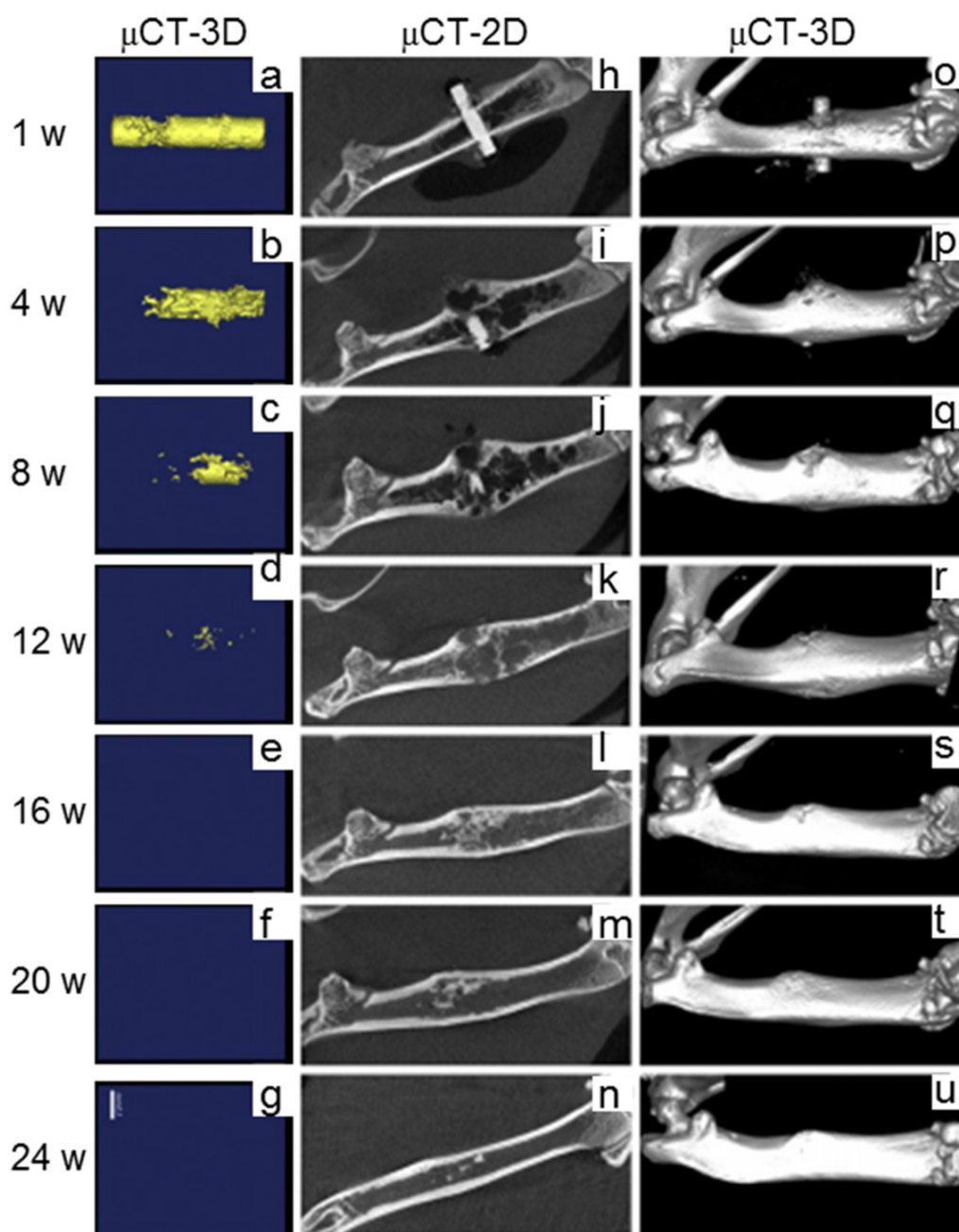


Figure 13. μ CT reconstructions showing the degradation process of ZX50 pins and bone response [280]. (a–g) 3-D reconstruction of the degradation process of the pin, (h–n) 2-D slices of the degradation process of the pin and (o–u) 3-D displays of the bone response. The ZX50 pin fully degraded 12 weeks after implantation. The bone recovered restitution after the complete degradation of the implanted pin without observation of inflammation. (with permission from Elsevier and Copyright Clearance Center).

6. Summary

This review presents recent developments of Mg-Zn based alloys for both industrial and biomedical applications. Various attempts have been made to improve the corrosion resistance and mechanical properties of Mg-Zn based alloys, including alloying addition, processing, development of composites, etc. The new developments focus on wrought alloys rather than as-cast alloys.

Obvious composition–microstructure–properties relationships can be observed, especially for Mg-Zn-Y alloys. Some Mg-Zn based alloys show good potential for structural or biomedical

applications—for example, Mg-Zn-Ca alloys as implants and new sheet materials for industrial wrought applications. On the other hand, inconsistent results between different studies can still be found, especially for the binary Mg-Zn system, which seems to offer no real potential for further developments. However, a good understanding of the binary Mg-Zn system is the basis for any further development of more complicated Mg-Zn-X alloys. Moreover, a satisfactory combination of high strength and good corrosion properties is difficult to be achieved, since more element addition usually results in a higher volume fraction of secondary phases, which is usually unfavorable for the corrosion performance. The combination of micro-alloying and wrought processing seems to be a promising way to solve this problem.

In summary, it can be stated that the current driving force for the development of Mg-Zn based alloys comes from two directions, both of which aim to prevent strong localized corrosion and to keep the corrosion rate of the alloy as low as possible. The first direction is the demand for new sheet material, mainly for industrial transport applications, and the second one is that of biomedical applications. Thus, the clear trend for the current ternary Mg-Zn-X and quaternary Mg-Zn-X-Y systems is to reduce the Zn content (less than 1 wt.%) and to improve strength by micro-alloying with ternary/quaternary alloying addition and wrought processing. In particular, the newly developed Mg-Zn-Ca-Zr sheet alloys [227,277] do have the potential to replace the currently most used AZ31 sheet alloys in many applications. To assure the biocompatibility and cytotoxicity, careful selection of bio-safe alloying elements and controlling of release rates of alloying elements within the safety range are of fundamental importance. However, more research is still needed for a better understanding of the Mg-Zn system and its interaction with other alloying elements to develop new Mg-Zn-X-Y alloys with better combinations of corrosion performance and mechanical properties.

Funding: This research was funded by China Scholarship Council (CSC), grant number 201606310043.

Acknowledgments: We would like to thank the China Scholarship Council (CSC) for a scholarship to Pingli Jiang (CSC No. 201606310043). The general discussion with colleagues in the department of Corrosion and Surface Technology, Helmholtz-Zentrum Geesthacht is also gratefully acknowledged.

Conflicts of Interest: The authors declare no conflict of interest. The funders had no role in the design of the study; in the collection, analyses, or interpretation of data; in the writing of the manuscript, or in the decision to publish the results.

Appendix A

Table A1. Potentials or relative Volta potentials of some secondary phases in Mg-Zn based alloys summarized from published literature.

Secondary Phase	Alloy	Condition of Alloy	Testing Method	Potential or Relative Volta Potential	Condition of Measurement	Details about the Instrument	Ref.
MgZn ₂	Mg-Zn	Induction melting	Microcapillary electrochemical cell	-1.03 V (vs. SCE)	0.1 M NaCl	-	[77]
Mg ₁₂ ZnY	Mg3.1Zn7.6Y	As-cast	Scanning Kelvin probe force microscopy	250 mV	In air	Multimode 3D, Bruker Corporation	[88]
CaMgSi	Mg6Zn5Si0.8Ca	Extruded	Scanning Kelvin probe force microscopy	384.56 mV	In air	Nanoscope III Multimode AFM	[281]
Mg ₂ Si				96.23 mV			
MgZn ₂	Mg6Zn5Si0.8Ca	Extruded	Scanning Kelvin probe force microscopy	551.19 ± 77.85 mV	In air	Nanoscope III Multimode AFM	[282]
Mn ₅ Si ₃				427.81 ± 147.88 mV			
CaMgSi				408.32 ± 26.35 mV			
Mg ₂ Si				96.23 ± 21.91 mV			
Grain boundary	ZE41	As-cast	Scanning Kelvin probe force microscopy	-80 ± 5 mV	In air	Nanoscope Dimension™ 3100 AFM	[123]
Mg ₇ Zn ₃ RE				100 ± 5 mV			
Zr-Zn-rich				180 ± 10 mV			
Mg ₇ Zn ₃	Mg2Zn0.6Zr	As-cast	Scanning Kelvin probe force microscopy	120 mV	In air	Dimension Icon AFM	[283]
Mg(Zn, Zr)	Mg2Zn0.6Zr	Extrusion	Scanning Kelvin probe force microscopy	50mV	In air	Dimension Icon AFM	[283]
MgZn ₂	Mg6Zn0.5Zr	Extrusion	Scanning Kelvin probe force microscopy	320 mV	In air	NT-MDT, Moscow	[284]
Zn ₂ Zr ₃				230 mV			
CuMgZn	Mg6Zn0.5Zr1Cu	Extrusion	Scanning Kelvin probe force microscopy	680 mV	In air	NT-MDT, Moscow	[284]
MgZn ₂				510 mV			
Zn ₂ Zr ₃				370 mV			
Mg ₇₅ Zn ₂₀ Nd ₅	Mg2Zn0.2MnxNd	As-cast	Scanning Kelvin probe force microscopy	250 mV	In air	MFP 3D Infinity AFM	[285]

Table A1. Cont.

Secondary Phase	Alloy	Condition of Alloy	Testing Method	Potential or Relative Volta Potential	Condition of Measurement	Details about the Instrument	Ref.
Ca ₂ Mg ₆ Zn ₃	Mg ₂ Zn ₁ Ca _{0.2} Mn	As-cast	Scanning Kelvin probe force microscopy	60 mV	In air	MFP 3D Infinity AFM	[286]
Ca ₂ Mg ₆ Zn ₃		T4		30 mV			
MgZn ₂	Mg ₂ Zn _{0.2} Mn _x Ca (<i>x</i> = 0.38; 0.76; 1.10)	As-cast	Scanning Kelvin probe force microscopy	96 mV*	In air	MFP 3D Infinity AFM	[287]
Mg-Zn	ZK40	As-cast	Scanning Kelvin probe force microscopy	50 mV	In air	Nanoscope IIIa Multimode microscope	[288]
Mg-Zn-Zr-Fe	Mg ₄ Zn _{0.5} Zr ₂ Gd	As-cast	Scanning Kelvin probe force microscopy	430 mV	In air	Nanoscope IIIa Multimode microscope	[288]
(MgZn) ₃ Gd ₂				170 mV			
Mg-Zn-Zr-Fe	Mg ₄ Zn _{0.5} Zr ₂ Nd	As-cast	Scanning Kelvin probe force microscopy	140 mV	In air	Nanoscope IIIa Multimode microscope	
Mg ₇₅ Zn ₂₀ Nd ₅				35 mV			

* The value was the highest potential compiled from the line-profile analysis of the secondary phase because no average value was afforded in the reference.

Table A2. Corrosion rates and mechanical properties (tested at room temperature) of Mg-Zn based alloys summarized from published researches.

Composition/ wt.%	Condition	Electrolyte	Impurity Content/wt.%	Corrosion Rate/mm year ⁻¹			Tensile Property			Ref.
				P_i	P_H	P_W	YS/MPa	UTS/MPa	Elongation/%	
Mg0.5Zn	As-cast	SBF, 37 °C	0.003Fe; 0.0004Cu; 0.0005Ni; 0.004Mn; 0.002Al	3.1			75	112	18.4	[46]
Mg0.5Zn	As-cast	SBF, RT	0.004Fe; 0.004Cu; 0.001Ni	1.2	1		38	95	4.2	[50]
Mg0.5Zn	Backward-extrusion	SBF, RT		0.5	0.5		62	145	17.2	[50]
Mg0.8Zn	Extrusion						198	238	26.5	[26]
Mg1Zn	As-cast	SBF, 37 °C	0.004Fe; 0.0003Cu; 0.0004Ni; 0.003Mn; 0.003Al	2.8			80	128	16.1	[46]
Mg1Zn	As-cast	SBF, 37 °C	<0.00016Fe; <0.002Cu; <0.001Mn	0.5		2	61	188	13.8	[10]
Mg1Zn	As-cast	9 g/L NaCl	<0.004Fe; <0.004Cu; <0.004Ni; 0.03Mn; 0.02Al	0.9		1.3				[49]
Mg1Zn	As-cast		0.004Fe; 0.058Mn; 0.023Al; 0.031Si				20	102	1	[22]
Mg1Zn	As-cast	SBF, 37 °C	0.007Fe; 0.0295Cu; 0.013Mn; 0.023Al; 0.041Si			0.07				[42]
Mg1Zn	As-cast	SBF, RT	0.008Fe; 0.004Cu; 0.005Ni	4.1	1.1		43	99	6.1	[50]
Mg1Zn	As-cast	SBF, 37 °C		1.5	2					[45]
		Hank's, 37 °C		0.2	0.3					
Mg1Zn	T4	SBF, 37 °C				0.09				[42]
Mg1Zn	Backward-extrusion	SBF, RT		1.1	0.5		91	169	18.7	[50]
Mg1Zn	Extrusion	0.6 M NaCl				1.7				[61]
Mg1Zn	Hot-rolling	SBF, 37 °C		0.9	2.3					[45]
		Hank's, 37 °C		0.2	0.6					
Mg1Zn	Induction melting	In vivo				0.4				[157]
		EBSS, 37 °C				0.5				
		MEM, 37 °C				1				
		MEMp, 37 °C				1.7				
Mg1.25Zn	As-cast	SBF, 37 °C	0.008Fe; 0.043Mn; 0.022Al; 0.029Si	6.5		3.2				[41]
Mg1.5Zn	As-cast	SBF, RT	0.007Fe; 0.006Cu; 0.004Ni	8.5	1.4		51	109	5.9	[50]
Mg1.5Zn	Backward-extrusion	SBF, RT		1.3	0.5		101	190	17.2	[50]
Mg2Zn	As-cast	SBF, 37 °C	0.002Fe; 0.0005Cu; 0.0005Ni; 0.004Mn; 0.002Al	2.6			86	137	14.5	[46]
Mg2Zn	As-cast		0.007Fe; 0.03Mn; 0.033Al; 0.039Si				27	146	12.2	[22]
Mg2Zn	As-cast	SBF, RT	0.004Fe; 0.003Cu; 0.007Ni	9.7	1.3		65	121	5.3	[50]

Table A2. Cont.

Composition/ wt.%	Condition	Electrolyte	Impurity Content/wt.%	Corrosion Rate/mm year ⁻¹			Tensile Property			Ref.
				P_i	P_H	P_W	YS/MPa	UTS/MPa	Elongation/%	
Mg2Zn	Backward-extrusion	SBF, RT		1.4	0.6		111	198	15.7	[50]
Mg2Zn	Extrusion	0.6 M NaCl				3.4				[61]
Mg2Zn	Extrusion	3.5 wt.% NaCl		0.2						[40]
Mg2.5Zn	As-cast	SBF, 37 °C	0.010Fe; 0.032Mn; 0.018Al; 0.033Si	5.5		2.4				[41]
Mg2.6Zn	Extrusion						208	263	25.6	[26]
Mg2.65Zn	As-cast	0.9 wt.% NaCl				13.4	45	145	12	[289]
Mg2.9Zn	Powder metallurgy						84	219	4.7	[54]
Mg3Zn	As-cast	SBF, 37 °C	0.004Fe; 0.0005Cu; 0.0002Ni; 0.002Mn; 0.004Al	2.3			93	147	12.4	[46]
Mg3Zn	As-cast	9 g/L NaCl	<0.004Fe; 0.01Cu; <0.004Ni; 0.04Mn; <0.01Al	0.9		2.5				[49]
Mg3Zn	As-cast		0.007Fe; 0.022Mn; 0.029Al; 0.036Si				47	168	13.7	[22]
Mg3Zn	As-cast	MEM, 37 °C			0.5					[59]
Mg3Zn	As-cast	0.1 M NaCl		0.5	1.5					[58]
Mg3Zn	As-cast	SBF, 37 °C		5.2		2				[48]
Mg3Zn	T4	SBF, 37 °C		4.8		1.9				[48]
Mg3Zn	T4	0.1 M NaCl		0.4	1.4					[58]
Mg3Zn	T6	0.1 M NaCl		0.4	1.3					[58]
Mg3Zn	T6	SBF, 37 °C		2.1		1.2	28	140	9.7	[187]
Mg3Zn	T6 (aging for 10 h)	SBF, 37 °C	0.0045Fe; <0.0001Cu; 0.0006Ni; <0.0001Si		6.6					[43]
Mg3Zn	T6 (aging for 50 h)	SBF, 37 °C			7.3					[43]
Mg3Zn	T6 (aging for 144 h)	SBF, 37 °C			9.7					[43]
Mg3Zn	Extrusion	0.6 M NaCl				8.4				[61]
Mg3Zn	Extrusion	3.5 wt.% NaCl		0.3						[40]
Mg3Zn	Bi-direction rolling	SBF, 37 °C		2.6		2	49	183	12.6	[187]
Mg3.3Zn	Powder metallurgy						90	210	4.6	[54]
Mg4Zn	As-cast		0.008Fe; 0.021Mn; 0.019Al; 0.032Si				58	217	15.8	[22]
Mg4Zn	As-cast	SBF, 37 °C	0.009Fe; 0.028Mn; 0.024Al; 0.025Si	4.9		2.1				[41]
Mg4Zn	Powder metallurgy						95	216	4.1	[54]

Table A2. Cont.

Composition/ wt.%	Condition	Electrolyte	Impurity Content/wt.%	Corrosion Rate/mm year ⁻¹			Tensile Property			Ref.
				P_i	P_H	P_W	YS/MPa	UTS/MPa	Elongation/%	
Mg4Zn	As-cast	SBF, 37 °C	0.0072Fe; 0.0308Cu; 0.0101Mn; 0.0273Al; 0.0565Si			0.4				[42]
Mg4Zn	T4	SBF, 37 °C				0.1				[42]
Mg4Zn	Extrusion	0.6 M NaCl				10				[61]
Mg4Zn	Extrusion	3.5 wt.% NaCl		0.4						[40]
Mg4.2Zn	Extrusion						227	288	21	[26]
Mg4.4Zn	Powder metallurgy						68	155	8.4	[54]
Mg4.5Zn	T6						57	209	14.7	[138]
Mg5Zn	As-cast	SBF, 37 °C		0.3		1.3	76	195	8.5	[10]
Mg5Zn	As-cast		0.009Fe; 0.031Mn; 0.027Al; 0.034Si				68	185	9.2	[22]
Mg5Zn	As-cast	3.5 wt.% NaCl+Mg(OH) ₂ Salt spray (5 wt.%)	0.0034Fe; 0.0028Cu; 0.0015Ni; 0.0545Mn; 0.0105Al; 0.0296Si	7.8	13.5	15.1				[57]
Mg5Zn	As-cast	3.5 wt.% NaCl		0.6		2.7				[47]
Mg5Zn	T4	3.5 wt.% NaCl		0.5		2.3				[47]
Mg5Zn	T6 (aging for 4 h)	3.5 wt.% NaCl		1.2		4				[47]
Mg5Zn	T6 (aging for 10 h)	3.5 wt.% NaCl		1.5		5.5				[47]
Mg5Zn	Solid solution treatment	3.5 wt.% NaCl+Mg(OH) ₂ Salt spray (5 wt.%)		2.7	10	6.5				[57]
Mg5Zn	Extrusion	3.5 wt.% NaCl		0.5						[40]
Mg5Zn	Extrusion	3.5 wt.% NaCl+Mg(OH) ₂	0.000017Fe; <0.00001Cu; <0.000001Ni; 0.000011Si		1.7	2.6				[168]
Mg6Zn	As-cast		0.012Fe; 0.019Mn; 0.024Al; 0.033Si				69	182	7.2	[22]
Mg6Zn	As-cast	SBF, 37 °C	0.0062Fe; 0.025Cu; 0.0077Mn; 0.0478Al; 0.0489Si			3				[42]
Mg6Zn	T4	SBF, 37 °C				0.8				[42]

Table A2. Cont.

Composition/ wt.%	Condition	Electrolyte	Impurity Content/wt.%	Corrosion Rate/mm year ⁻¹			Tensile Property			Ref.
				P_i	P_H	P_W	YS/MPa	UTS/MPa	Elongation/%	
Mg6Zn	As-cast	SBF, 37 °C		6.2		3.5				[48]
Mg6Zn	T4	SBF, 37 °C		4.4		1.4				[48]
Mg6Zn	Extrusion	SBF, 37 °C		5.4		12.6				[60]
Mg6Zn	Extrusion	SBF, 37 °C In vivo	0.0038Fe; 0.0005Cu; 0.0005Ni; 0.0085Al; 0.0004Mn; 0.0016Si	0.16		0.07 2.3	170	280	19	[160]
Mg6Zn	Extrusion (PM)	Ringer's solution, 37 °C		0.4						[55]
Mg6Zn	Extrusion (PM) + T4	Ringer's solution, 37 °C		0.5						[55]
Mg6Zn	Extrusion (PM) + T6	Ringer's solution, 37 °C		0.4						[55]
Mg6Zn	Extrusion (PM) + T5	Ringer's solution, 37 °C		0.2						[55]
Mg6Zn1Ag	Extrusion (at 275 °C)	3.5 wt.% NaCl saturated with Mg(OH) ₂				8.5				[144]
Mg6Zn1Ag	Extrusion (at 350 °C)	3.5 wt.% NaCl saturated with Mg(OH) ₂				16.5				[144]
Mg6Zn1Ag	Extrusion (at 275 °C) + Aging	3.5 wt.% NaCl saturated with Mg(OH) ₂				83				[144]
Mg6Zn1Ag	Extrusion (at 350 °C) + Aging	3.5 wt.% NaCl saturated with Mg(OH) ₂				100.3				[144]
Mg7Zn	As-cast	SBF, 37 °C		1.2	3.2		67	136	6	[10]
Mg14.5Zn	Extrusion (PM)	Ringer's solution, 37 °C		1.2						[55]
Mg25.3Zn	Extrusion (PM)	Ringer's solution, 37 °C		1.8						[55]
Mg40.3Zn	Extrusion (PM)	Ringer's solution, 37 °C		3						[55]
Mg0.8Zn0.6Ca	As-cast	HBSS, 37 °C PBS, 37 °C	0.0021Fe; 0.0021Cu; <0.0021Ni; 0.0231Mn; 0.02Al; 0.0343Si	0.08 0.02		0.1 0.1				[75]

Table A2. Cont.

Composition/ wt.%	Condition	Electrolyte	Impurity Content/wt.%	Corrosion Rate/mm year ⁻¹			Tensile Property			Ref.
				P_i	P_H	P_W	YS/MPa	UTS/MPa	Elongation/%	
Mg0.8Zn1.6Ca	As-cast	HBSS, 37 °C	<0.0006Fe; 0.0012Cu; <0.0021Ni; 0.011Mn; 0.036Al; 0.019Si	0.1		0.2				[75]
		PBS, 37 °C		0.04		0.2				
Mg1Zn0.5Ca	Extrusion						105	210	44	[72]
Mg1Zn1Ca	As-cast	Hank's, 37 °C	0.004Fe; 0.058Mn; 0.023Al; 0.031Si			2.1	45	125	5.7	[23]
Mg1.2Zn0.5Ca	As-cast	SBF, 37 °C		15.8		8.2	60	121	3.2	[176]
Mg1.2Zn0.5Ca	T6	SBF, 37 °C		9.6		4.8	84	151	4.9	[176]
Mg1.8Zn0.6Ca	As-cast	HBSS, 37 °C	<0.0006Fe; 0.001Cu; <0.0021Ni; 0.0079Mn; 0.0199Al; 0.024Si	0.03		0.1				[75]
		PBS, 37 °C		0.02		0.2				
Mg1.8Zn1.6Ca	As-cast	HBSS, 37 °C	<0.0006Fe; 0.0011Cu; <0.0021Ni; 0.0077Mn; 0.0358Al; 0.0225Si	0.04		0.2				[75]
		PBS, 37 °C		0.06		0.3				
Mg2Zn0.2Ca	As-cast	Ringer's solution, 37 °C		10.3						[51]
Mg2Zn0.2Ca	Extrusion						118	211	24.4	[167]
Mg2Zn0.24Ca	As-cast	SBF, 37 °C		12.1						[290]
Mg2Zn0.24Ca	High pressure torsion	SBF, 37 °C		0.08						[290]
Mg2Zn0.5Ca	Rapid solidification	SBF, 37 °C				9.6				[291]
Mg2Zn1Ca	As-cast	Hank's, 37 °C	0.007Fe; 0.03Mn; 0.033Al; 0.039Si			2.4	52	143	7.3	[23]
Mg3Zn0.2Ca	Extrusion	SBF, 37 °C	0.0096Fe; 0.1302Al			1.2	224	273	18.5	[7]
Mg3Zn0.3Ca	As-cast	SBF, 37 °C	0.004Fe; <0.0001Cu; <0.0001Ni; <0.0001Si		6.9					[70]
Mg3Zn0.3Ca	T4	SBF, 37 °C			3.4					[70]
Mg3Zn1Ca	As-cast	Hank's, 37 °C	0.007Fe; 0.022Mn; 0.029Al; 0.036Si			2.9	57	160	8.3	[23]
Mg3Zn1.34Ca	Induction melting	In vivo				0.8				[157]
		EBSS, 37 °C				1.6				
		MEM, 37 °C				4.7				
		MEMp, 37 °C				3.3				
Mg3Zn2Ca	Gravity casting						90 *	101	0.4	[215]
Mg3Zn2Ca	Aging						88 *	126	2	[215]

* means 0.2% yield strength.

Table A2. Cont.

Composition/ wt.%	Condition	Electrolyte	Impurity Content/wt.%	Corrosion Rate/mm year ⁻¹			Tensile Property			Ref.	
				P_i	P_H	P_W	YS/MPa	UTS/MPa	Elongation/%		
Mg3Zn2Ca	Squeeze casting						80 *	135	0.9	[215]	
Mg3Zn2Ca	Squeeze casting + Aging						74 *	144	3.3	[215]	
Mg3Zn2Ca	ECAP						166 *	206	1.1	[215]	
Mg3Zn2Ca	Aging + ECAP						174 *	223	2.4	[215]	
Mg3.3Zn3.2Ca0.5RE	Squeeze casting (surface)	3.5 wt.% NaCl, pH 11	0.02Fe;0.002Ni; 0.01Mn; 0.04Al; 0.02Si	7.2							[213]
	Squeeze casting (core)			6.1							
Mg3.6Zn3.5Ca0.7RE	Thixocasting (surface)	3.5 wt.% NaCl, pH 11	0.009Fe;0.002Ni; 0.01Mn; 0.06Al; 0.03Si	3							[213]
	Thixocasting (core)			3.6							
Mg4Zn0.2Ca	Extrusion	SBF, 37 °C	0.0095Fe; 0.1125Al			1.3	243	295	18	[7]	
Mg4Zn0.5Ca	As-cast	Hank's, 37 °C	0.007Fe; 0.022Mn; 0.029Al; 0.036Si				70	180	12.3	[22]	
Mg4Zn0.5Ca	As-cast							211	17	[16]	
Mg4Zn0.5Ca	Extrusion							273	34	[16]	
Mg4Zn1Ca	As-cast	Hank's, 37 °C	0.008Fe; 0.021Mn; 0.019Al; 0.032Si				83	175	8.7	[22]	
Mg4Zn1.5Ca	As-cast	Hank's, 37 °C	0.009Fe; 0.031Mn; 0.027Al; 0.034Si				83	167	7.1	[22]	
Mg4Zn2Ca	As-cast	Hank's, 37 °C	0.012Fe; 0.019Mn; 0.024Al; 0.033Si				90	143	2.1	[22]	
Mg4Zn1Ca	As-cast	Hank's, 37 °C	0.008Fe; 0.021Mn; 0.019Al; 0.032Si			4.4	63	182	9.1	[23]	
Mg5Zn1Ca	As-cast	Hank's, 37 °C	0.009Fe; 0.031Mn; 0.027Al; 0.034Si			6.2	65	173	8.2	[23]	
Mg5Zn1Ca	As-cast	SBF, 37 °C	<0.0016Fe; <0.002Cu; <0.001Mn	0.28	1.36			87		[5]	
Mg5Zn2Ca	As-cast	SBF, 37 °C		0.34	1.84			93		[5]	
Mg5Zn3Ca	As-cast	SBF, 37 °C		0.44	3.23			83		[5]	
Mg5.25Zn0.6Ca	Extrusion						178	276	25.9	[193]	
Mg5.25Zn0.6Ca	Extrusion + ECAP-A						246	332	15.5	[193]	
Mg5.25Zn0.6Ca	Extrusion + ECAP-B						180	287	21.9	[193]	
Mg5.25Zn0.6Ca	Extrusion + ECAP-C						131	228	12.6	[193]	

Table A2. Cont.

Composition/ wt.%	Condition	Electrolyte	Impurity Content/wt.%	Corrosion Rate/mm year ⁻¹			Tensile Property			Ref.
				P_i	P_H	P_W	YS/MPa	UTS/MPa	Elongation/%	
Mg5.25Zn0.6Ca	Extrusion						220		21.4	[292]
Mg5.25Zn0.6Ca0.3Mn	Extrusion						272		18.9	[292]
Mg6Zn1Ca	As-cast	Hank's, 37 °C	0.012Fe; 0.019Mn; 0.024Al; 0.033Si			9.2	67	145	4.5	[23]
Mg6Zn1Ca	Rapid solidification	PBS, RT		2.9						[230]
Mg6.6Zn0.19Ca	Extrusion						148	275	26	[293]
Mg5.7Zn0.17Ca0.84Zr	Extrusion						310	357	18	[293]
Mg10Zn1Ca	Rapid solidification	PBS, RT		3.1						[230]
Mg20Zn1Ca	Rapid solidification	PBS, RT		4.7						[230]
Mg46Zn10Ca	Induction melting	MEM, RT		0.4						[294]
Mg49Zn10Ca	Induction melting	MEM, RT		0.04						[294]
Mg51Zn10Ca	Induction melting	MEM, RT		0.04						[294]
Mg54Zn10Ca	Induction melting	MEM, RT		0.03						[294]
Mg56Zn10Ca	Induction melting	MEM, RT		0.4						[294]
Mg46Zn15Ca	Induction melting	MEM, RT		0.05						[294]
Mg49Zn15Ca	Induction melting	MEM, RT		0.2						[294]
Mg51Zn15Ca	Induction melting	MEM, RT		0.1						[294]
Mg54Zn15Ca	Induction melting	MEM, RT		0.1						[294]
Mg56Zn15Ca	Induction melting	MEM, RT		0.4						[294]
Mg51Zn10Ca	Induction melting	SBF, 37 °C		0.18						[295]
Mg50Zn10Ca2.6Y	Induction melting	SBF, 37 °C		0.19						[295]
Mg47Zn10Ca7.7Y	Induction melting	SBF, 37 °C		0.19						[295]
Mg50Zn10Ca	Induction melting	SBF, 37 °C		0.06	12.2					[296]
Mg50Zn10Ca2.6Y	Induction melting	SBF, 37 °C		0.2	28.3					[296]
Mg50Zn10Ca5.2Y	Induction melting	SBF, 37 °C		0.4	60.1					[296]
Mg51Zn12Ca	Rapid solidification	SBF, 37 °C		5.2	1.8					[297]
Mg51Zn12Ca	Rapid solidification + Annealing	SBF, 37 °C		9.2	10.4					[297]
Mg54Zn10Ca	Induction melting	SBF, 37 °C				0.2				[211]
Mg47Zn12Ca	Induction melting	SBF, 37 °C				0.4				[211]

Table A2. Cont.

Composition/ wt.%	Condition	Electrolyte	Impurity Content/wt.%	Corrosion Rate/mm year ⁻¹			Tensile Property			Ref.
				P_i	P_H	P_W	YS/MPa	UTS/MPa	Elongation/%	
Mg54Zn10Ca	Induction melting (22 mm)	SBF, 37 °C		35						[298]
Mg54Zn10Ca	Induction melting (8 mm)	SBF, 37 °C		0.2						[298]
Mg59Zn12Ca	Induction melting (22 mm)	SBF, 37 °C		5.1						[298]
Mg59Zn12Ca	Induction melting (8 mm)	SBF, 37 °C		0.1						[298]
Mg0.5Zn1Y	As-cast	3.5 wt.% NaCl		1.9	25.1	27.9				[87]
Mg0.9Zn1.6Y	As-cast	0.1 M NaCl		0.3	0.7	1.1	59	97	6.3	[88]
Mg1Zn2Y	As-cast	3.5 wt.% NaCl		0.2	1.9	2.4				[87]
Mg1.3Zn5Y	Rapid solidification	0.17 M NaCl			5.8					[299]
Mg1.5Zn0.2Y	Extrusion + Rolling		0.011Fe; 0.0006Cu; 0.001Ni; 0.024Mn; 0.02Al; 0.0091Si				139	222	23	[94]
Mg1.5Zn0.2Y	Extrusion + Rolling		0.011Fe; 0.006Cu; 0.001Ni; 0.024Mn; 0.019Al; 0.0073Si				178	225	18	[94]
Mg2Zn0.36Y	Extrusion	Hank's, 37 °C		0.04		0.7	197	260	23	[53]
Mg2Zn0.82Y	Extrusion	Hank's, 37 °C	<0.015Fe; <0.001Cu; <0.0005Ni	0.1		2	212	265	25	[53]
Mg2Zn1.54Y	Extrusion	Hank's, 37 °C		0.05		0.8	214	265	27	[53]
Mg2Zn4Y	As-cast	3.5 wt.% NaCl		8.1	88.8	110.4				[87]
Mg2Zn5Y	Gravity casting	0.17 M NaCl			33.8					[300]
Mg2Zn5Y	Injection casting	0.17 M NaCl			12.5					[300]
Mg2Zn5Y	Rapid solidification (10 m s ⁻¹)	0.17 M NaCl			5.1					[300]
Mg2Zn5Y	Rapid solidification (20 m s ⁻¹)	0.17 M NaCl			1.4					[300]
Mg2Zn5Y	Rapid solidification (40 m s ⁻¹)	0.17 M NaCl			1.2					[300]
Mg2Zn5Y1.3Al	Rapid solidification	0.17 M NaCl			0.6					[299]
Mg2Zn5Y2.6Al	Rapid solidification	0.17 M NaCl			0.3					[299]
Mg2Zn5Y3.9Al	Rapid solidification	0.17 M NaCl			0.1					[299]

Table A2. Cont.

Composition/ wt.%	Condition	Electrolyte	Impurity Content/wt.%	Corrosion Rate/mm year ⁻¹			Tensile Property			Ref.
				P_i	P_H	P_W	YS/MPa	UTS/MPa	Elongation/%	
Mg2Zn5Y1.3Nd	Rapid solidification	0.17 M NaCl			1					[299]
Mg2Zn5Y1.3Si	Rapid solidification	0.17 M NaCl			0.8					[299]
Mg2.1Zn5.2Y	As-cast	0.1 M NaCl		1.5	5.4	4.5	95	141	5.2	[88]
Mg2.6Zn5Y	Rapid solidification	0.17 M NaCl			2.4					[299]
Mg2.6Zn5.2Y	As-cast	DMEM+FBS, 37 °C		0.2						[89]
Mg2.6Zn5.2Y0.5Zr	As-cast	DMEM+FBS, 37 °C		0.1						[89]
Mg2.6Zn5.2Y0.5Zr	Extruded	DMEM+FBS, 37 °C		0.2						[89]
Mg2.6Zn2.6Y	As-cast						102		16	[97]
Mg2.6Zn2.6Y	Rolling						261		12	[97]
Mg2.6Zn2.6Y	Rolling + Annealing						190		25	[97]
Mg3Zn0.6Y	Rolling						121	226	30.2	[108]
Mg3.1Zn5.2Y	As-cast	0.1 M NaCl		0.6	2.1	9.5	107	148	3	[88]
Mg3.3Zn5Y	Rapid solidification	0.17 M NaCl			13.5					[299]
Mg4Zn0.7Y	Rolling						209	258	17.4	[74]
Mg3.24Zn3.34Y0.67Zr	As-cast						127	185	3	[301]
Mg3.93Zn4.14Y0.69Zr	As-cast						168	226	2	[301]
Mg4.87Zn5.03Y0.73Zr	As-cast						150	195	1.9	[301]
Mg5.95Zn6.08Y0.64Zr	As-cast						121	165	1.4	[301]
Mg4Zn8Y	As-cast	3.5 wt.% NaCl		3.8	71.3	80.5				[87]
Mg5Zn0.5Y	Rolling						157	306	23.4	[93]
Mg5.2Zn5.2Y	As-cast						130		11	[97]
Mg5.2Zn5.2Y	Rolling						317		10	[97]
Mg5.2Zn5.2Y	Rolling + Annealing						217		22	[97]

Table A2. Cont.

Composition/ wt.%	Condition	Electrolyte	Impurity Content/wt.%	Corrosion Rate/mm year ⁻¹			Tensile Property			Ref.
				P_i	P_H	P_W	YS/MPa	UTS/MPa	Elongation/%	
Mg5.2Zn10Y	As-cast	DMEM + FBS, 37 °C		0.07						[89]
Mg4.4Zn2.4Y6.2RE	Extrusion	PBS	0.00246Fe; 0.1Mn	0.4	4.9					[302]
Mg5.7Zn1Y3.8RE	Extrusion	PBS	0.00139Fe; 0.1Mn	0.1	2.5					[302]
Mg6Zn1.2Y	Rolling						157	259	29.3	[108]
Mg6Zn1.5Y0.5Zr	Extrusion (at 300 °C)						285	340	10.2	[180]
Mg6Zn1.5Y0.5Zr	Extrusion (at 300 °C) + Peak-aging						289	336	15.5	[180]
Mg6Zn1.5Y0.5Zr	Extrusion (at 350 °C)						278	336	108	[180]
Mg6Zn1.5Y0.5Zr	Extrusion (at 350 °C) + Peak-aging						290	332	17.9	[180]
Mg6Zn1.5Y0.5Zr	Extrusion (at 400 °C)						258	325	14.6	[180]
Mg6Zn1.5Y0.5Zr	Extrusion (at 400 °C) + Peak-aging						277	326	16.9	[180]
Mg6Zn1.2Y0.4Zr	As-cast						157	237	3	[177]
Mg6Zn1.2Y0.4Zr	Extrusion						203	290	16.7	[177]
Mg6.7Zn1.3Y0.6Zr	As-forged	0.1 M NaCl		0.5		2.2	202	280	17	[303]
Mg6.7Zn1.3Y0.6Zr	As-forged+T4	0.1 M NaCl		0.3		1.3	183	262	22	[303]
Mg7.7Zn10.7Y	As-cast	DMEM+FBS, 37 °C		0.08						[89]
Mg7.7Zn7.7Y	As-cast						177		10	[97]
Mg5.2Zn5.2Y	Rolling						380		6	[97]
Mg5.2Zn5.2Y	Rolling+Annealing						293		15	[97]
Mg8Zn1.6Y	Rolling						173	270	26.9	[108]
Mg8Zn14Y	As-cast			0.9						[304]
Mg8Zn6Y6Gd	As-cast			1.1						[304]
Mg8Zn5Y8Gd	As-cast			1.5						[304]
Mg8Zn4Y12Gd	As-cast			1.5						[304]

Table A2. Cont.

Composition/ wt.%	Condition	Electrolyte	Impurity Content/wt.%	Corrosion Rate/mm year ⁻¹			Tensile Property			Ref.
				P_i	P_H	P_W	YS/MPa	UTS/MPa	Elongation/%	
Mg8.6Zn1.6Y	Rolling			1.1			210	355	23.4	[90]
Mg10Zn2Y	Rolling						181	276	21.9	[108]
Mg10.8Zn1.9Y	Rolling						220	370	19.7	[90]
Mg10.8Zn1.9Y0.5Zr	Rolling						180	325	23.5	[90]
Mg11Zn2Y	Rolling						220	370	17.2	[93]
Mg10.5Zn2.1Y	Extrusion (at 300 °C)						200	300		[92]
Mg10.5Zn2.1Y	Extrusion +Heat-treatment						197	297	18	[305]
Mg11Zn2Y	Extrusion (Ratio: 10)						232	258	4.5	[86]
Mg11Zn2Y	Extrusion (Ratio: 15)						236	312	13.2	[86]
Mg11Zn2Y	Extrusion (Ratio: 20)						240	336	15.6	[86]
Mg12Zn2.4Y	Rolling						189	285	21.3	[108]
Mg12Zn1.2Y0.4Zr	As-cast						172	216	0.8	[177]
Mg12Zn1.2Y0.4Zr	Extrusion						231	320	13	[177]
Mg15.5Zn2.6Y	Extrusion (at 300 °C)						210	320		[92]
Mg15.5Zn2.6Y	Extrusion +Heat-treatment						213	321		[305]
Mg2Zn5Y0.6Zr	Extrusion						233	290	17.2	[306]
Mg4Zn5Y0.6Zr	Extrusion						322	345	18.3	[306]
Mg6Zn5Y0.6Zr	Extrusion						244	283	20.2	[306]
ZE41	As-cast	1 N NaCl	0.006Fe; <0.002Cu; <0.001Ni; 0.02Mn; 0.004Al; <0.001Cr	2.1	13.5	12				[118]
ZE41	As-cast	Hank's, 37 °C	0.0056Fe; 0.0014Cu; 0.0002Ni; 0.02Mn; 0.0101Al	0.24	1.6	2.3				[113]

Table A2. Cont.

Composition/ wt.%	Condition	Electrolyte	Impurity Content/wt.%	Corrosion Rate/mm year ⁻¹			Tensile Property			Ref.
				P_i	P_H	P_W	YS/MPa	UTS/MPa	Elongation/%	
ZE41	As-cast	0.2 M Na ₂ SO ₄ + 0.1 M NaCl (30 °C)	0.006Fe; <0.002Cu; 0.02Mn; <0.001Ni; 0.004Al	5.4						[117]
		0.2 M Na ₂ SO ₄ + 1.0 M NaCl (30 °C)		10						
		0.6 M Na ₂ SO ₄ + 0.1 M NaCl (30 °C)		8.49						
		0.6 M Na ₂ SO ₄ + 1.0 M NaCl(30 °C)		14.3						
		1.0 M Na ₂ SO ₄ + 0.1 M NaCl(30 °C)		12.3						
		0.1 M Na ₂ SO ₄ + 1.0 M NaCl (30 °C)		18.4						
ZE41	As-cast	0.1 M NaCl (pH3)	0.006Fe; <0.002Cu; 0.02Mn; <0.001Ni; 0.004Al	3.7	9.7				[119]	
		0.1 M NaCl (pH7)		0.63	2.3					
		0.1 M NaCl (pH11)		0.22	1.5					
		1 M NaCl (pH3)		5	20					
		1 M NaCl (pH7)		1.6	14					
		1 M NaCl (pH11)		0.6	8					
ZE41	As-cast	Hank's, 37 °C (pH6.6)	0.0056Fe; 0.0014Cu; 0.0002Ni; 0.02Mn: 0.0101Al		1.5	3.4			[148]	
		Hank's, 37 °C (pH6.9)			2.3	4.2				
		Hank's, 37 °C (pH7.4)			2.9	1.5				
		Hank's, 37 °C (pH8.2)			3.2	1.5				
ZE41	T5	0.5 wt.% NaCl	0.003Fe	0.1					[120]	
ZE41	As-cast	0.001 M NaCl	0.1Cu; 0.01Ni; 0.15Mn	0.07					[122]	
ZE41	T4	0.001 M NaCl		0.1					[122]	

Table A2. Cont.

Composition/wt.%	Condition	Electrolyte	Impurity Content/wt.%	Corrosion Rate/mm year ⁻¹			Tensile Property			Ref.
				P_i	P_H	P_W	YS/MPa	UTS/MPa	Elongation/%	
ZE41	As-cast	0.2 M Na ₂ SO ₄	0.006Fe; <0.002Cu; <0.001Ni; 0.02Mn; 0.004Al	pH2	12					[150]
				pH5	5.4					
				pH7	2.8					
				pH9	2					
				pH12	1.3					
		0.6 M Na ₂ SO ₄		pH2	15					
				pH5	9.3					
				pH7	6.2					
				pH9	4.7					
				pH12	3.9					
		1.0 M Na ₂ SO ₄		pH2	20.1					
				pH5	14.2					
				pH7	11.1					
				pH9	8.1					
				pH12	7.1					
ZE41	As-cast	3 wt.% NaCl	0.006Fe; <0.002Cu; <0.001Ni; 0.02Mn; 0.004Al	1.1	46				[15]	
		Interrupted 3 wt.% NaCl salt spray (1 min spray, 119 min humid)				47				
		Interrupted 3 wt.% NaCl salt spray (15 min spray, 105 min humid)				2.7				
Mg1Zn0.3Zr	Rolling					194	254	15.6	[74]	
Mg2Zn0.6Zr	As-cast	Hank's, 37 °C	<0.01Fe; <0.01Cu; <0.01Ni	0.3		51	195	18.1	[283]	
Mg2Zn0.6Zr	Extrusion	Hank's, 37 °C	<0.01Fe; <0.01Cu; <0.01Ni	0.1		194	258	17.6	[283]	
Mg2Zn0.8Zr	Extrusion					221	271	24.5	[307]	
Mg3Zn0.6Zr	As-cast					215	300	9	[125]	

Table A2. Cont.

Composition/wt.%	Condition	Electrolyte	Impurity Content/wt.%	Corrosion Rate/mm year ⁻¹			Tensile Property			Ref.
				P_i	P_H	P_W	YS/MPa	UTS/MPa	Elongation/%	
Mg3Zn0.8Zr	Extrusion + Aging	SBF, 37 °C		0.04				245	8.8	[206]
Mg3Zn0.8Zr0.5β-TCP	Extrusion + Aging	SBF, 37 °C		0.05				260	10.3	[206]
Mg3Zn0.8Zr1 β-TCP	Extrusion + Aging	SBF, 37 °C		0.03				280	10.5	[206]
Mg3Zn0.8Zr1.5 β-TCP	Extrusion + Aging	SBF, 37 °C		0.04				275	6.3	[206]
Mg4Zn0.5Zr	As-cast	DMEM+FBS, 37 °C	0.002Fe; 0.014Cu; 0.018Ni; 0.003Mn; 0.007Si	0.8		1.1				[308]
Mg4Zn0.5Zr	Heat-treatment	DMEM+FBS, 37 °C		0.9		0.5				[308]
Mg4Zn0.5Zr	Indirect chill casting	0.5 wt.% NaCl	0.00113Fe; 0.00141Cu; 0.00128Ni		2.9		102	225	12.8	[288]
Mg4Zn0.5Zr2Gd	Indirect chill casting	0.5 wt.% NaCl	0.00069Fe; 0.00292Cu; <0.003Ni		1.8		100	228	17.9	[288]
Mg4Zn0.5Zr2Nd	Indirect chill casting	0.5 wt.% NaCl	0.0011Fe; 0.00148Cu; 0.00282Ni		4.1		99	148	3.9	[288]
Mg4Zn0.7Zr	As-cast		0.03Cu; 0.01Ni; 0.2Si				108	216	16	[132]
Mg4Zn0.7Zr3Nd	As-cast						144	202	6	[132]
Mg6Zn0.6Zr	As-cast						235	315	8	[125]
Mg5Zn0.3Zr	Extrusion + Heat-treatment	5 wt.% NaCl				9.8				[129]
Mg5Zn0.3Zr1Nd	Extrusion + Heat-treatment	5 wt.% NaCl				9				[129]
Mg5Zn0.3Zr2Nd	Extrusion + Heat-treatment	5 wt.% NaCl				4.7				[129]
Mg5Zn0.3Zr0.5Y	Extrusion + Heat-treatment	5 wt.% NaCl				5.4				[129]
Mg5Zn0.3Zr1Y	Extrusion + Heat-treatment	5 wt.% NaCl				9				[129]
Mg5Zn0.6Zr	As-cast						88	236	18.2	[136]
Mg5Zn0.6Zr1Nd	As-cast						102	196	7.3	[136]
Mg5Zn0.6Zr2Nd	As-cast						89	133	2.9	[136]
Mg5Zn0.6Zr2Nd0.5Y	As-cast						94	203	9.1	[136]

Table A2. Cont.

Composition/wt.%	Condition	Electrolyte	Impurity Content/wt.%	Corrosion Rate/mm year ⁻¹			Tensile Property			Ref.
				P_i	P_H	P_W	YS/MPa	UTS/MPa	Elongation/%	
Mg5Zn0.6Zr2Nd1Y	As-cast						102	219	12.1	[136]
Mg5.3Zn0.48Zr	Extrusion	PBS, 37 °C								[189]
Mg5.3Zn0.48Zr	Extrusion+ECAP	PBS, 37 °C								[189]
Mg5.3Zn0.48Zr	Extrusion	PBS, 37 °C		1.4			290	340	15.1	[191]
Mg5.3Zn0.48Zr	Extrusion+ECAP	PBS, 37 °C		1.3			219	285	32.4	[191]
Mg5.45Zn0.45Zr	As-cast	Hank's, 37 °C		0.4	0.9					[126]
		DMEM, 37 °C		0.7						
		DMEM+FBS, 37 °C		1.3						
Mg5.45Zn0.45Zr	Extrusion	Hank's, 37 °C		0.2	0.3					[126]
		DMEM, 37 °C		0.3						
		DMEM+FBS, 37 °C		0.5						
Mg5.54Zn0.56Zr	Extrusion						237	312	15.5	[309]
Mg5.54Zn0.56Zr	Extrusion +T5						273	329	16.5	[309]
Mg5.6Zn0.5Zr	Laser rapid solidification (420 J/mm ³)	Hank's, 37 °C								[229]
Mg5.6Zn0.5Zr	Laser rapid solidification (500 J/mm ³)	Hank's, 37 °C								[229]
Mg5.6Zn0.5Zr	Laser rapid solidification (600 J/mm ³)	Hank's, 37 °C								[229]
Mg5.6Zn0.5Zr	Laser rapid solidification (750 J/mm ³)	Hank's, 37 °C								[229]
Mg5.5Zn0.4Zr0.74Y	Extrusion (at 300 °C)						263	326	12.9	[310]
Mg5.5Zn0.4Zr0.74Y	Extrusion (at 350 °C)						268	331	14.6	[310]
Mg5.5Zn0.4Zr0.74Y	Extrusion (at 400 °C)						257	327	14.5	[310]
Mg5.5Zn0.4Zr1.35Y	Extrusion (at 300 °C)						285	341	10.2	[310]
Mg5.5Zn0.4Zr1.35Y	Extrusion (at 350 °C)						279	338	10.8	[310]
Mg5.5Zn0.4Zr1.35Y	Extrusion (at 400 °C)						258	327	14.6	[310]
Mg5.5Zn0.4Zr1.72Y	Extrusion (at 300 °C)						267	335	15.3	[310]
Mg5.5Zn0.4Zr1.72Y	Extrusion (at 350 °C)						263	330	12.8	[310]
Mg5.5Zn0.4Zr1.72Y	Extrusion (at 400 °C)						283	338	10.1	[310]

Table A2. Cont.

Composition/wt. %	Condition	Electrolyte	Impurity Content/wt. %	Corrosion Rate/mm year ⁻¹			Tensile Property			Ref.
				P_i	P_H	P_W	YS/MPa	UTS/MPa	Elongation/%	
Mg5.5Zn0.6Zr	High strain-rate rolling						223	311	18.3	[133]
Mg5.5Zn0.6Zr0.2Gd	High strain-rate rolling						227	307	25.3	[133]
Mg5.5Zn0.6Zr0.5Gd	High strain-rate rolling						235	318	23.2	[133]
Mg5.5Zn0.6Zr0.8Gd	High strain-rate rolling						242	327	22	[133]
Mg5.79Zn0.35Zr	As-cast						108	233	9.6	[135]
Mg5.79Zn0.35Zr	T4						84	272	15.7	[135]
Mg5.79Zn0.35Zr	T6						165	281	10.9	[135]
Mg5.79Zn0.35Zr	Extrusion (at 300 °C) + T5						261	340	19.8	[135]
Mg5.79Zn0.35Zr	Extrusion (at 350 °C) + T5						269	343	19.2	[135]
Mg5.79Zn0.35Zr	Extrusion (at 400 °C) + T5						273	341	18.3	[135]
Mg5.79Zn0.35Zr	Extrusion + T6						222	311	15.8	[135]
Mg5.79Zn0.35Zr1.3Gd	As-cast						99	212	7.7	[135]
Mg5.79Zn0.35Zr1.3Gd	T4						78	262	16.1	[135]
Mg5.79Zn0.35Zr1.3Gd	T6						146	276	13.2	[135]
Mg5.79Zn0.35Zr1.3Gd	Extrusion (at 300 °C) + T5						252	321	20	[135]
Mg5.79Zn0.35Zr1.3Gd	Extrusion (at 350 °C) + T5						258	324	19.8	[135]
Mg5.79Zn0.35Zr1.3Gd	Extrusion (at 400 °C) + T5						261	325	19.9	[135]
Mg5.79Zn0.35Zr1.3Gd	Extrusion + T6						239	306	18.8	[135]
Mg6Zn0.5Zr	As-cast	Ringer's solution, 37 °C		1.9						[124]
		SBF, 37 °C		9.6						
Mg6.01Zn0.49Zr	Extrusion						209	315	19.3	[134]

Table A2. Cont.

Composition/wt. %	Condition	Electrolyte	Impurity Content/wt. %	Corrosion Rate/mm year ⁻¹			Tensile Property			Ref.
				P_i	P_H	P_W	YS/MPa	UTS/MPa	Elongation/%	
Mg5.94Zn0.37Zr0.96Y	Extrusion						246	325	22.3	[134]
Mg5.73Zn0.39Zr1.63Y	Extrusion						229	313	15.6	[134]
Mg5.50Zn0.43Zr2.2Y	Extrusion						261	313	17.6	[134]
Mg5.30Zn0.41Zr3.59Y	Extrusion						292	330	20.7	[134]
Mg5.88Zn0.48Zr	Extrusion						289	346	16.4	[311]
Mg5.57Zn0.52Zr0.45Yb	Extrusion						322	367	15.3	[311]
Mg5.64Zn0.47Zr0.93Yb	Extrusion						355	382	6.9	[311]
Mg6.03Zn0.56Zr1.78Yb	Extrusion						412	418	2.7	[311]
Mg5.88Zn0.48Zr	T5						315	352	14.3	[311]
Mg5.57Zn0.52Zr0.45Yb	T5						324	367	15.1	[311]
Mg5.64Zn0.47Zr0.93Yb	T5						323	371	14.8	[311]
Mg6.03Zn0.56Zr1.78Yb	T5						359	397	10.6	[311]
Mg5.88Zn0.48Zr	T6						266	332	14.3	[311]
Mg5.57Zn0.52Zr0.45Yb	T6						302	356	15.1	[311]
Mg5.64Zn0.47Zr0.93Yb	T6						314	368	14.9	[311]
Mg6.03Zn0.56Zr1.78Yb	T6						312	378	10.5	[311]
Mg9Zn0.6Zr	Extrusion						263	351	25	[175]
Mg9Zn0.6Zr	Aging						313	352	20	[175]
Mg9Zn0.6Zr0.5Er	Extrusion						313	366	22	[175]
Mg9Zn0.6Zr0.5Er	Aging						342	372	18	[175]
Mg1Zn3Gd	As-cast	9g/L NaCl	<0.004Fe; <0.004Cu; <0.004Ni; 0.3Al; 0.02Mn	1.2		0.83				[49]
Mg3Zn3Gd	As-cast		<0.004Fe; <0.004Cu; <0.004Ni; <0.01Al; 0.02Mn	1.9		5.29				[49]
Mg1Zn1Gd	Rolling						182	231	29.2	[185]
Mg2Zn1Gd	Rolling						189	233	27.2	[185]
Mg2.6Zn6.5Gd	Induction melting						288	335	9.2	[312]
Mg2.6Zn6.5Gd	Extrusion (Homogenized for 0.5 h)						303	352	8.3	[312]

Table A2. Cont.

Composition/ wt.%	Condition	Electrolyte	Impurity Content/wt.%	Corrosion Rate/mm year ⁻¹			Tensile Property			Ref.
				P_i	P_H	P_W	YS/MPa	UTS/MPa	Elongation/%	
Mg2.6Zn6.5Gd	Extrusion (Homogenized for 5 h)						336	391	7	[312]
Mg2.6Zn6.5Gd	Extrusion (Homogenized for 10 h)						345	380	6.9	[312]
Mg4.5Zn0.5Gd	T6						98	160	2.2	[138]
Mg4.5Zn1Gd	T6						110	189	4.1	[138]
Mg4.5Zn1.5Gd	T6						113	231	8.3	[138]
Mg4.5Zn2Gd	T6						121	215	6.4	[139]
Mg4.5Zn3Gd	T6						92	194	6.3	[139]
Mg4.5Zn5Gd	T6						80	154	5.6	[139]
Mg8.9Zn1.6Gd	Extrusion (at 300 °C)						214	311	16.5	[313]
Mg8.9Zn1.6Gd	Extrusion (at 400 °C)						199	302	14.6	[313]
Mg8.9Zn1.6Gd	Extrusion (at 300 °C) + T4						170	284	15.6	[313]
Mg8.9Zn1.6Gd	Extrusion (at 300 °C) + T6						188	285	15.3	[313]
Mg8.9Zn1.6Gd	Extrusion (at 400 °C) + T4						166	275	16.3	[313]
Mg8.9Zn1.6Gd	Extrusion (at 400 °C) + T6						190	274	15.7	[313]
Mg8.9Zn1.6Gd3.9Cu	Extrusion (at 300 °C)						222	297	10.4	[313]
Mg8.9Zn1.6Gd3.9Cu	Extrusion (at 400 °C)						223	299	11.4	[313]
Mg8.9Zn1.6Gd3.9Cu	Extrusion (at 300 °C) + T4						164	258	11.1	[313]
Mg8.9Zn1.6Gd3.9Cu	Extrusion (at 300 °C) + T6						161	248	10.6	[313]
Mg8.9Zn1.6Gd3.9Cu	Extrusion (at 400 °C) + T4						174	266	16.3	[313]
Mg8.9Zn1.6Gd3.9Cu	Extrusion (at 400 °C) + T6						172	257	12.3	[313]
Mg1Zn0.1Ce	Rolling						191	216	19.8	[74]
Mg1Zn0.3RE0.5Zr	Rolling						203	234	23.7	[74]
Mg4Zn1RE0.5Zr	Rolling						258	291	8.8	[74]
Mg1Zn0.5Mn	As-cast	Ringer's solution, 37 °C				1.6				[112]
Mg1Zn1Mn	As-cast		<0.01Fe; <0.005Cu; <0.005Ni; <0.3Al				44	175	12.1	[314]
Mg1Zn1Mn	Extrusion	SBE, 37 °C	<0.01Fe; <0.005Cu; <0.005Ni; <0.3Al			0.06	247	280	21.8	[133]

Table A2. Cont.

Composition/ wt.%	Condition	Electrolyte	Impurity Content/wt.%	Corrosion Rate/mm year ⁻¹			Tensile Property			Ref.
				P_i	P_H	P_W	YS/MPa	UTS/MPa	Elongation/%	
Mg1.5Zn0.5Mn	As-cast	Ringer's solution, 37 °C		1.1						[112]
Mg1.5Zn1Mn	As-cast	Ringer's solution, 37 °C		0.9						[112]
Mg2Zn0.2Mn	As-cast	Hank's, 37 °C	0.003Fe; 0.002Mn; <0.001Ni; 0.1Al; 0.02Si	0.2	0.2	1.1				[113]
Mg2Zn0.2Mn	As-cast	Ringer's solution, 37 °C		3.4						[51]
Mg2Zn0.2Mn	As-cast	SBF, 37 °C				3.7				[109]
Mg2Zn0.2Mn	Extrusion Aging	SBF, 37 °C				3.1				[109]
Mg2Zn1Mn	As-cast						58	181	11.1	[314]
Mg2Zn1Mn	Extrusion	SBF, 37 °C	<0.01Fe; <0.005Cu; <0.005Ni; <0.3Al			0.2	249	284	20.9	[133]
Mg2Zn1Mn	Rolling						127	236	24.3	[74]
Mg2Zn1Mn0.3Ca	As-cast	Hank's, 37 °C		1.7			59	162	7.4	[52]
Mg2Zn1Mn0.5Ca	As-cast	Hank's, 37 °C		1.3			73	188	9.1	[52]
Mg2Zn1Mn1Ca	As-cast	Hank's, 37 °C		0.07			81	136	2.7	[52]
Mg2Zn0.2Mn	As-cast	SBF, 37 °C	<0.01Fe; <0.01Cu; <0.01Ni	8.4		20.4				[287]
Mg2Zn0.2Mn0.38Ca	As-cast	SBF, 37 °C	<0.01Fe; <0.01Cu; <0.01Ni	7		15.4				[287]
Mg2Zn0.2Mn0.76Ca	As-cast	SBF, 37 °C	<0.01Fe; <0.01Cu; <0.01Ni	10.1		23.5				[287]
Mg2Zn0.2Mn1.1Ca	As-cast	SBF, 37 °C	<0.01Fe; <0.01Cu; <0.01Ni	13.1		27.8				[287]
Mg2Zn0.2Mn	Solid solution treatment	Kokubo solution, 37 °C		6.6		14.6				[315]
Mg2Zn0.2Mn0.38Ca	Solid solution treatment	Kokubo solution, 37 °C		6.3		11.8				[315]
Mg2Zn0.2Mn0.76Ca	Solid solution treatment	Kokubo solution, 37 °C		8.1		18.6				[315]
Mg2Zn0.2Mn1.1Ca	Solid solution treatment	Kokubo solution, 37 °C		9.2		23.5				[315]
Mg2Zn0.2Mn1.1Ca	As-cast	SBF, 37 °C		13.1				129	1.5	[286]
Mg2Zn0.2Mn1.1Ca	Solid solution treatment (at 300 °C)	SBF, 37 °C		11.1				148	3	[286]

Table A2. Cont.

Composition/ wt.%	Condition	Electrolyte	Impurity Content/wt.%	Corrosion Rate/mm year ⁻¹			Tensile Property			Ref.
				P_i	P_H	P_W	YS/MPa	UTS/MPa	Elongation/%	
Mg2Zn0.2Mn1.1Ca	Solid solution treatment (at 360 °C)	SBF, 37 °C		10.6						[286]
Mg2Zn0.2Mn1.1Ca	Solid solution treatment (at 420 °C)	SBF, 37 °C		5.9				198		[286]
Mg2Zn0.2Mn1.1Ca	Solid solution treatment (at 460 °C)	SBF, 37 °C		8.1				220		[286]
Mg2Zn0.2Mn1.1Ca	Solid solution treatment (at 500 °C)	SBF, 37 °C		8.8						[286]
Mg2Zn0.2Mn	As-cast	Kokubo solution, 37 °C	<0.01Fe; <0.01Cu; <0.01Ni	8.4				102		[285]
Mg2Zn0.2Mn0.6Nd	As-cast	Kokubo solution, 37 °C	<0.01Fe; <0.01Cu; <0.01Ni	1.2				178		[285]
Mg2Zn0.2Mn1.2Nd	As-cast	Kokubo solution, 37 °C	<0.01Fe; <0.01Cu; <0.01Ni	2.2				208		[285]
Mg2Zn0.2Mn1.8Nd	As-cast	Kokubo solution, 37 °C	<0.01Fe; <0.01Cu; <0.01Ni	3.8				215		[285]
Mg2Zn0.2Mn	Solid solution treatment	Kokubo solution, 37 °C	<0.01Fe; <0.01Cu; <0.01Ni	6.6				158		[316]
Mg2Zn0.2Mn0.6Nd	Solid solution treatment	Kokubo solution, 37 °C	<0.01Fe; <0.01Cu; <0.01Ni	0.8				224		[316]
Mg2Zn0.2Mn1.2Nd	Solid solution treatment	Kokubo solution, 37 °C	<0.01Fe; <0.01Cu; <0.01Ni	1.8				228		[316]
Mg2Zn0.2Mn1.8Nd	Solid solution treatment	Kokubo solution, 37 °C	<0.01Fe; <0.01Cu; <0.01Ni	3.1				235		[316]
Mg3Zn1Mn	As-cast						66	217	15.5	[314]
Mg3Zn1Mn	Extrusion	SBF, 37 °C	<0.01Fe; <0.005Cu; <0.005Ni; <0.3Al			0.4	276	316	10.5	[133]
Mg6Zn0.5Mn	Extrusion	3.5 wt.% NaCl saturated with Mg(OH) ₂	0.04Fe(max); 0.005Ni(max); 0.05Cu(max)	0.46		8.3				[114]
Mg6Zn0.5Mn0.5Si	Extrusion	3.5 wt.% NaCl saturated with Mg(OH) ₂	0.04Fe(max); 0.005Ni(max); 0.05Cu(max)	1.25		26.7				[114]

Table A2. Cont.

Composition/ wt.%	Condition	Electrolyte	Impurity Content/wt.%	Corrosion Rate/mm year ⁻¹			Tensile Property			Ref.
				P_i	P_H	P_W	YS/MPa	UTS/MPa	Elongation/%	
Mg6Zn0.5Mn1Si	Extrusion	3.5 wt.% NaCl saturated with Mg(OH) ₂	0.04Fe(max); 0.005Ni(max); 0.05Cu(max)	0.54		13.5				[114]
Mg6Zn0.5Mn2Si	Extrusion	3.5 wt.% NaCl saturated with Mg(OH) ₂	0.04Fe(max); 0.005Ni(max); 0.05Cu(max)	0.47		9.5				[114]
Mg6Zn1Mn	Induction melting	3.5 wt.% NaCl		0.1			108	335	20.3	[111]
Mg6Zn1Mn	Rapid solidification	3.5 wt.% NaCl		0.01			154	460	20.5	[111]
Mg6Zn1Mn	Extrusion	Hank's		0.2		1				[317]
Mg6Zn1Mn	Extrusion + Aging	Hank's		0.3		1.3				[317]
Mg6Zn1Mn	Twin roll casting + T4						170	284	17.1	[217]
Mg6Zn1Mn	Twin roll casting + T6						256	310	16.2	[217]
Mg6Zn1Mn1Al	Twin roll casting + T4						216	308	17.3	[217]
Mg6Zn1Mn1Al	Twin roll casting + T6						307	330	16.2	[217]
Mg6Zn1Mn3Al	Twin roll casting + T4						227	327	7.8	[217]
Mg6Zn1Mn1Al	Twin roll casting + T6						319	360	6.3	[217]
Mg6Zn0.5Mn	Extrusion	3.5 wt.% NaCl saturated with Mg(OH) ₂		5.9		3.1				[115]
		0.01M NaOH		7.3		0.27				[116]
Mg6Zn0.5Mn0.5Si	Extrusion	3.5 wt.% NaCl saturated with Mg(OH) ₂		28.3		16.9				[115]
		0.01M NaOH		4.1		0.36				[116]
Mg6Zn0.5Mn0.5Si0.2Ca	Extrusion	3.5 wt.% NaCl saturated with Mg(OH) ₂		25.5		9.1				[115]
		0.01M NaOH		5.4		0.42				[116]

Table A2. Cont.

Composition/ wt.%	Condition	Electrolyte	Impurity Content/wt.%	Corrosion Rate/mm year ⁻¹			Tensile Property			Ref.
				P_i	P_H	P_W	YS/MPa	UTS/MPa	Elongation/%	
Mg6Zn0.5Mn0.5Si0.4Ca	Extrusion	3.5 wt.% NaCl saturated with Mg(OH) ₂		21.1		7.1				[115]
		0.01M NaOH		4.5		0.42				[116]
Mg6Zn0.5Mn1Si	Extrusion	3.5 wt.% NaCl saturated with Mg(OH) ₂		15.6		12.3				[115]
		0.01M NaOH		3.2		0.36				[116]
Mg6Zn0.5Mn1Si0.2Ca	Extrusion	3.5 wt.% NaCl saturated with Mg(OH) ₂		22.3		10.3				[115]
		0.01M NaOH		2.7		0.38				[116]
Mg6Zn0.5Mn1Si0.4Ca	Extrusion	3.5 wt.% NaCl saturated with Mg(OH) ₂		25.9		12.1				[115]
		0.01M NaOH		3.8		0.49				[116]
Mg6Zn0.5Mn2Si	Extrusion	3.5 wt.% NaCl saturated with Mg(OH) ₂		18.9		12.6				[115]
		0.01M NaOH		2.7		0.52				[116]
Mg6Zn0.5Mn2Si0.2Ca	Extrusion	3.5 wt.% NaCl saturated with Mg(OH) ₂		16.9		12.2				[115]
		0.01M NaOH		2.6		0.59				[116]
Mg6Zn0.5Mn2Si0.4Ca	Extrusion	3.5 wt.% NaCl saturated with Mg(OH) ₂		21.9		14.3				[115]
		0.01M NaOH		3.6		0.78				[116]
Mg2Zn0.2Si	As-cast	Ringer's solution, 37 °C		12.3						[51]
Mg6Zn1Si	As-cast						135	183	5.8	[318]
Mg6Zn1Si0.1Ca	As-cast						149	213	5.1	[318]
Mg6Zn1Si0.25Ca	As-cast						161	220	5.2	[318]
Mg6Zn1Si0.5Ca	As-cast						146	197	4.7	[318]
Mg6Zn4Si	As-cast	3.5 wt.% NaCl		4.2		2.8				[319]
Mg6Zn4Si0.1Sr	As-cast	3.5 wt.% NaCl		4.1		2.5				[319]
Mg6Zn4Si0.5Sr	As-cast	3.5 wt.% NaCl		0.003		1.5				[319]
Mg6Zn4Si1Sr	As-cast	3.5 wt.% NaCl		0.1		1.6				[319]
Mg6Zn4Si1.5Sr	As-cast	3.5 wt.% NaCl		5		1				[319]

Table A2. Cont.

Composition/ wt.%	Condition	Electrolyte	Impurity Content/wt.%	Corrosion Rate/mm year ⁻¹			Tensile Property			Ref.
				P_i	P_H	P_W	YS/MPa	UTS/MPa	Elongation/%	
Mg6Zn3Si1Mn0.4Ca	Extrusion	3.5 wt.% NaCl saturated with Mg(OH) ₂	0.04Fe(max); 0.005Ni(max); 0.05Cu(max)	0.73						[282]
Mg6Zn5Si1Mn0.4Ca	Extrusion	3.5 wt.% NaCl saturated with Mg(OH) ₂	0.04Fe(max); 0.005Ni(max); 0.05Cu(max)	0.42						[282]
Mg6Zn5Si1Mn0.6Ca	Extrusion	3.5 wt.% NaCl saturated with Mg(OH) ₂	0.04Fe(max); 0.005Ni(max); 0.05Cu(max)	0.44						[282]
Mg6Zn5Si1Mn0.8Ca	Extrusion	3.5 wt.% NaCl saturated with Mg(OH) ₂	0.04Fe(max); 0.005Ni(max); 0.05Cu(max)	0.49						[282]
Mg6Zn10Si1Mn0.4Ca	Extrusion	3.5 wt.% NaCl saturated with Mg(OH) ₂	0.04Fe(max); 0.005Ni(max); 0.05Cu(max)	0.39						[282]
Mg6Zn2Al0.2Mn	As-cast	1 M NaCl		7.3			101	190	8.5	[320]
Mg6Zn2Al0.2Mn0.5Sn	As-cast	1 M NaCl		8.6			118	225	8.9	[320]
Mg6Zn2Al0.2Mn1Sn	As-cast	1 M NaCl		7			122	215	7.8	[320]
Mg6Zn2Al0.2Mn2Sn	As-cast	1 M NaCl		6.8			127	206	7	[320]
Mg6Zn2Al0.2Mn3Sn	As-cast	1 M NaCl		6.4			137	203	6.5	[320]
Mg6Zn2Al0.2Mn0.5Sn0.2Ca	As-cast	1 M NaCl		5.3			115	220	8	[320]
Mg6Zn2Al0.2Mn3Sn0.2Ca	As-cast	1 M NaCl		3.8			135	255	9	[320]
Mg8Zn5Al0.2Mn	As-cast	1 M NaCl		11.9			106	142	3.5	[320]
Mg6Zn5Al4RE	As-cast						140	242	6.4	[321]
Mg6Zn7Al4RE	As-cast						93	168	3.2	[321]
Mg8Zn5Al4RE	As-cast						95	174	3.1	[321]
Mg10Zn5Al4RE	As-cast						93	159	1.8	[321]
Mg8Zn4Al	As-cast						125	174	3.85	[322]
Mg8Zn4Al0.5Sn	As-cast						137	185	4.05	[322]
Mg8Zn4Al1Sn	As-cast						149	194	4.32	[322]
Mg8Zn4Al2Sn	As-cast						163	180	3.13	[322]
Mg1Zn0.2Sr	Backward-extrusion	SBF		0.53		1.8	89	187	11	[140]
Mg1Zn0.5Sr	Backward-extrusion	SBF		0.71		2.8	93	211	11.8	[140]
Mg1Zn0.8Sr	Backward-extrusion	SBF		2.4		3.9	117	210	11.5	[140]
Mg1Zn1Sr	Backward-extrusion	SBF		5.1		6.3	130	249	12.6	[140]

Table A2. Cont.

Composition/ wt.%	Condition	Electrolyte	Impurity Content/wt.%	Corrosion Rate/mm year ⁻¹			Tensile Property			Ref.
				P_i	P_H	P_W	YS/MPa	UTS/MPa	Elongation/%	
Mg2Zn0.1Sr	As-cast	SBF; 37 °C	0.025Fe; <0.001Cu; <0.001Ni; 0.065Al	8.9		6.4	58	179	11.5	[141]
Mg2Zn0.2Sr	As-cast	SBF; 37 °C	0.033Fe; <0.001Cu; <0.001Ni; 0.058Al	7.6		5.6	66	186	14.4	[141]
Mg2Zn0.3Sr	As-cast	SBF; 37 °C	0.018Fe; <0.001Cu; <0.001Ni; 0.072Al	9.5		6.8	66	179	10.7	[141]
Mg2Zn0.4Sr	As-cast	SBF; 37 °C	0.026Fe; <0.001Cu; <0.001Ni; 0.061Al	13.1		7	64	176	10.4	[141]
Mg2Zn0.5Sr	As-cast	SBF; 37 °C	0.033Fe; <0.001Cu; <0.001Ni; 0.074Al	14.9		7.5	52	153	6.3	[141]
Mg2Zn0.5Sr	Aging	HBSS			0.2		62	142	8.9	[143]
Mg4Zn0.5Sr	Aging	HBSS			0.4		104	169	3	[143]
Mg6Zn0.5Sr	Aging	HBSS			10.6		128	209	3.6	[143]
Mg4Zn1Sr	As-cast	SBF; 37 °C		9.4		2.3		250	5	[142]
Mg6Zn1Ag	Extrusion (at 275 °C)	3.5 wt.% NaCl saturated with Mg(OH) ₂					33.3			[144]
Mg6Zn1Ag	Extrusion (at 350 °C)	3.5 wt.% NaCl saturated with Mg(OH) ₂					48.1			[144]
Mg6Zn1Ag	Extrusion (at 275 °C) + Aging	3.5 wt.% NaCl saturated with Mg(OH) ₂					88.4			[144]
Mg6Zn1Ag	Extrusion (at 350 °C) + Aging	3.5 wt.% NaCl saturated with Mg(OH) ₂					106.2			[144]
Mg6Zn2Ag	Extrusion (at 275 °C)	3.5 wt.% NaCl saturated with Mg(OH) ₂					40			[144]
Mg6Zn2Ag	Extrusion (at 350 °C)	3.5 wt.% NaCl saturated with Mg(OH) ₂					58.5			[144]
Mg6Zn2Ag	Extrusion (at 275 °C) + Aging	3.5 wt.% NaCl saturated with Mg(OH) ₂					97.8			[144]
Mg6Zn2Ag	Extrusion (at 350 °C) + Aging	3.5 wt.% NaCl saturated with Mg(OH) ₂					111.2			[144]
Mg6Zn3Ag	Extrusion (at 275 °C)	3.5 wt.% NaCl saturated with Mg(OH) ₂					42.7			[144]

Table A2. Cont.

Composition/ wt.%	Condition	Electrolyte	Impurity Content/wt.%	Corrosion Rate/mm year ⁻¹			Tensile Property			Ref.
				P_i	P_H	P_W	YS/MPa	UTS/MPa	Elongation/%	
Mg6Zn3Ag	Extrusion (at 350 °C)	3.5 wt.% NaCl saturated with Mg(OH) ₂				66				[144]
Mg6Zn3Ag	Extrusion (at 275 °C) + Aging	3.5 wt.% NaCl saturated with Mg(OH) ₂				85.4				[144]
Mg6Zn3Ag	Extrusion (at 350 °C) + Aging	3.5 wt.% NaCl saturated with Mg(OH) ₂				102.9				[144]
Mg6Zn3Si0.4Ca	Extrusion	3.5 wt.% NaCl saturated with Mg(OH) ₂	0.04Fe(max); 0.005Ni(max); 0.05Cu(max)	0.73						[281]
Mg6Zn5Si0.4Ca	Extrusion	3.5 wt.% NaCl saturated with Mg(OH) ₂	0.04Fe(max); 0.005Ni(max); 0.05Cu(max)	0.42						[281]
Mg6Zn5Si0.6Ca	Extrusion	3.5 wt.% NaCl saturated with Mg(OH) ₂	0.04Fe(max); 0.005Ni(max); 0.05Cu(max)	0.44						[281]
Mg6Zn5Si0.8Ca	Extrusion	3.5 wt.% NaCl saturated with Mg(OH) ₂	0.04Fe(max); 0.005Ni(max); 0.05Cu(max)	0.48						[281]
Mg6Zn10Si0.4Ca	Extrusion	3.5 wt.% NaCl saturated with Mg(OH) ₂	0.04Fe(max); 0.005Ni(max); 0.05Cu(max)	0.4						[281]
Mg6Zn3Cu	Squeeze casting	Salt spray				11.7				[323]
Mg1.3Zn3.9La	Rapid solidification	1 wt.% NaCl	0.0229Fe		1.5					[228]
Mg2.6Zn3.9La	Rapid solidification	1 wt.% NaCl	0.0231Fe		2.3					[228]
Mg3.9Zn3.9La	Rapid solidification	1 wt.% NaCl	0.0234Fe		3.4					[228]
Mg5.2Zn3.9La	Rapid solidification	1 wt.% NaCl	0.0234Fe		6.3					[228]
Mg1.3Zn5.2Yb	Rapid solidification	1 wt.% NaCl	0.0237Fe		0.8					[228]
Mg2.6Zn5.2Yb	Rapid solidification	1 wt.% NaCl	0.0237Fe		1.4					[228]
Mg3.9Zn5.2Yb	Rapid solidification	1 wt.% NaCl	0.0237Fe		2.8					[228]
Mg5.2Zn5.2Yb	Rapid solidification	1 wt.% NaCl	0.0239Fe		4.1					[228]
Mg12Zn4Al0.5Ca	Gravity casting						118	151	1.3	[214]
Mg12Zn4Al0.5Ca	Squeeze casting						113	211	5.2	[214]

* means 0.2% yield strength.

References

1. Song, G.L.; Atrens, A. Corrosion mechanisms of magnesium alloys. *Adv. Eng. Mater.* **1999**, *1*, 11–33. [[CrossRef](#)]
2. Gusieva, K.; Davies, C.; Scully, J.; Birbilis, N. Corrosion of magnesium alloys: The role of alloying. *Int. Mater. Rev.* **2015**, *60*, 169–194. [[CrossRef](#)]
3. Yang, Z.; Li, J.; Zhang, J.; Lorimer, G.; Robson, J. Review on research and development of magnesium alloys. *Acta Metall. Sin.* **2008**, *21*, 313–328. [[CrossRef](#)]
4. Kulekci, M.K. Magnesium and its alloys applications in automotive industry. *Int. J. Adv. Manuf. Technol.* **2008**, *39*, 851–865. [[CrossRef](#)]
5. Yin, P.; Li, N.F.; Lei, T.; Liu, L.; Ouyang, C. Effects of Ca on microstructure, mechanical and corrosion properties and biocompatibility of Mg–Zn–Ca alloys. *J. Mater. Sci. Mater. Med.* **2013**, *24*, 1365–1373. [[CrossRef](#)] [[PubMed](#)]
6. Sun, Y.; Zhang, B.; Wang, Y.; Geng, L.; Jiao, X. Preparation and characterization of a new biomedical Mg–Zn–Ca alloy. *Mater. Des.* **2012**, *34*, 58–64. [[CrossRef](#)]
7. Li, H.; Liu, D.; Zhao, Y.; Jin, F.; Chen, M. The influence of Zn content on the corrosion and wear performance of Mg–Zn–Ca alloy in simulated body fluid. *J. Mater. Eng. Perform.* **2016**, *25*, 3890–3895. [[CrossRef](#)]
8. Li, N.; Zheng, Y. Novel magnesium alloys developed for biomedical application: A review. *J. Mater. Sci. Technol.* **2013**, *29*, 489–502. [[CrossRef](#)]
9. Xin, Y.; Hu, T.; Chu, P. In vitro studies of biomedical magnesium alloys in a simulated physiological environment: A review. *Acta Biomater.* **2011**, *7*, 1452–1459. [[CrossRef](#)]
10. Cai, S.; Lei, T.; Li, N.; Feng, F. Effects of Zn on microstructure, mechanical properties and corrosion behavior of Mg–Zn alloys. *Mater. Sci. Eng. C* **2012**, *32*, 2570–2577.
11. Bamberger, M.; Dehm, G. Trends in the development of new Mg alloys. *Annu. Rev. Mater. Res.* **2008**, *38*, 505–533. [[CrossRef](#)]
12. Blum, W.; Zhang, P.; Watzinger, B.; Grossmann, B.; Haldenwanger, H. Comparative study of creep of the die-cast Mg-alloys AZ91, AS21, AS41, AM60 and AE42. *Mater. Sci. Eng. A* **2001**, *319*, 735–740. [[CrossRef](#)]
13. Han, Q.; Kad̄, B.K.; Viswanathan, S. Design perspectives for creep-resistant magnesium die-casting alloys. *Philos. Mag.* **2004**, *84*, 3843–3860. [[CrossRef](#)]
14. El-Rahman, S.S.A. Neuropathology of aluminum toxicity in rats (glutamate and GABA impairment). *Pharmacol. Res.* **2003**, *47*, 189–194. [[CrossRef](#)]
15. Xia, X.; Davies, C.; Nie, J.; Birbilis, N. Influence of composition and processing on the corrosion of magnesium alloys containing binary and ternary additions of zinc and strontium. *Corrosion* **2014**, *71*, 38–49. [[CrossRef](#)]
16. Geng, L.; Zhang, B.; Li, A.; Dong, C. Microstructure and mechanical properties of Mg–4.0Zn–0.5Ca alloy. *Mater. Lett.* **2009**, *63*, 557–559. [[CrossRef](#)]
17. Haferkamp, H.; Bach, F.W.; Kaese, V.; M̄hwald, K.; Niemeyer, M.; Schreckenberger, H.; Tai, P.T. Magnesium Corrosion–Processes, Protection of Anode and Cathode. In *Magnesium-Alloys and Technology*; Kainer, K., Ed.; Wiley-VCH: Weinheim, Germany, 2003; pp. 226–241.
18. Mordike, B.; Lukác, P. Physical metallurgy. In *Magnesium Technology: Metallurgy, Design Data, Applications*; Friedrich, H.E., Mordike, B., Eds.; Springer: Berlin, Germany, 2006; p. 76.
19. Shi, Z.-Z.; Zhang, W.-Z. Investigation on the microstructure of a τ -Mg₃₂(Al, Zn) 49 strengthened Mg–Zn–Al alloy with relatively low Zn content. *Phase Transit.* **2012**, *85*, 41–51. [[CrossRef](#)]
20. Zhang, J.; Li, Z.-S.; Guo, Z.-X.; Pan, F.-S. Solidification microstructural constituent and its crystallographic morphology of permanent-mould-cast Mg–Zn–Al alloys. *T. Nonferr. Metal Soc.* **2006**, *16*, 452–458. [[CrossRef](#)]
21. Tapiero, H.; Tew, K.D. Trace elements in human physiology and pathology: Zinc and metallothioneins. *Biomed. Pharmacother.* **2003**, *57*, 399–411. [[CrossRef](#)]
22. Zhang, B.; Wang, Y.; Geng, L. Research on Mg–Zn–Ca alloy as degradable biomaterial. In *Biomaterials-Physics and Chemistry*; Pignatello, R., Ed.; InTech: London, UK, 2011; pp. 183–204.
23. Zhang, B.; Hou, Y.; Wang, X.; Wang, Y.; Geng, L. Mechanical properties, degradation performance and cytotoxicity of Mg–Zn–Ca biomedical alloys with different compositions. *Mater. Sci. Eng. C* **2011**, *31*, 1667–1673.
24. Okamoto, H. Comment on Mg–Zn (magnesium–zinc). *J. Phase Equilib.* **1994**, *15*, 129–130. [[CrossRef](#)]

25. Witte, F.; Hort, N.; Vogt, C.; Cohen, S.; Kainer, K.U.; Willumeit, R.; Feyerabend, F. Degradable biomaterials based on magnesium corrosion. *Curr. Opin. Solid State Mater. Sci.* **2008**, *12*, 63–72. [[CrossRef](#)]
26. Somekawa, H.; Osawa, Y.; Mukai, T. Effect of solid-solution strengthening on fracture toughness in extruded Mg–Zn alloys. *Scripta Mater.* **2006**, *55*, 593–596. [[CrossRef](#)]
27. Ohno, M.; Schmid-Fetzer, R. Mg-rich phase equilibria of Mg–Mn–Zn alloys analyzed by computational thermochemistry. *ZMetl* **2006**, *97*, 526–532. [[CrossRef](#)]
28. Tsai, A.-P.; Murakami, Y.; Niikura, A. The Zn-Mg-Y phase diagram involving quasicrystals. *Philos. Mag. A* **2000**, *80*, 1043–1054. [[CrossRef](#)]
29. Bhan, S.; Lal, A. The Mg-Zn-Zr system (magnesium-zinc-zirconium). *J. Phase Equilib.* **1993**, *14*, 634–637. [[CrossRef](#)]
30. Higashi, I.; Shiotani, N.; Uda, M.; Mizoguchi, T.; Katoh, H. The crystal structure of Mg₅₁Zn₂₀. *J. Solid State Chem.* **1981**, *36*, 225–233. [[CrossRef](#)]
31. Gao, X.; Nie, J. Structure and thermal stability of primary intermetallic particles in an Mg–Zn casting alloy. *Scripta Mater.* **2007**, *57*, 655–658. [[CrossRef](#)]
32. Komura, Y.; Tokunaga, K. Structural studies of stacking variants in Mg-base Friauf–Laves phases. *Acta Crystallogr. Sect. B* **1980**, *36*, 1548–1554. [[CrossRef](#)]
33. Samson, S. Die Kristallstruktur von Mg₂Zn₁₁-Isomorphie zwischen Mg₂Zn₁₁ und Mg₂Cu₆Al₅. *Acta Chem. Scand.* **1949**, *3*, 835–843. [[CrossRef](#)]
34. Gallot, J.; Graf, R. X-Ray Investigation of the Equilibrium Phase in a 60% Zinc Containing Magnesium-Zinc Alloy. *Comptes Rendus Acad. Sci.* **1966**, *262*, 1219–1222.
35. Chun, J.; Byrne, J. Precipitate strengthening mechanisms in magnesium zinc alloy single crystals. *J. Mater. Sci. Mater. Med.* **1969**, *4*, 861–872. [[CrossRef](#)]
36. Cáceres, C.; Blake, A. The Strength of Concentrated Mg–Zn Solid Solutions. *Phys. Status Solidi. A* **2002**, *194*, 147–158. [[CrossRef](#)]
37. Clark, J. Transmission electron microscopy study of age hardening in a Mg-5 wt.% Zn alloy. *Acta Metall.* **1965**, *13*, 1281–1289. [[CrossRef](#)]
38. Kirkland, N.T.; Staiger, M.P.; Nisbet, D.; Davies, C.H.; Birbilis, N. Performance-driven design of biocompatible Mg alloys. *JOM* **2011**, *63*, 28–34. [[CrossRef](#)]
39. Makar, G.; Kruger, J. Corrosion studies of rapidly solidified magnesium alloys. *J. Electrochem. Soc.* **1990**, *137*, 414–421. [[CrossRef](#)]
40. Song, Y.; Han, E.-H.; Shan, D.; Yim, C.D.; You, B.S. The effect of Zn concentration on the corrosion behavior of Mg–xZn alloys. *Corros. Sci.* **2012**, *65*, 322–330. [[CrossRef](#)]
41. Bakhsheshi-Rad, H.; Hamzah, E.; Fereidouni-Lotfabadi, A.; Daroonparvar, M.; Yajid, M.; Mezbahul-Islam, M.; Kasiri-Asgarani, M.; Medraj, M. Microstructure and bio-corrosion behavior of Mg–Zn and Mg–Zn–Ca alloys for biomedical applications. *Mater. Corros.* **2014**, *65*, 1178–1187. [[CrossRef](#)]
42. Kubasek, J.; Vojtech, D.; Pospisilova, I. Structural and corrosion characterization of biodegradable Mg–Zn alloy castings. *Kovove Mater.* **2012**, *50*, 415–424.
43. Lu, Y.; Bradshaw, A.; Chiu, Y.-L.; Jones, I. The role of β1' precipitates in the bio-corrosion performance of Mg–3Zn in simulated body fluid. *J. Alloys Compd.* **2014**, *614*, 345–352. [[CrossRef](#)]
44. Avedesian, M.M.; Baker, H. *ASM Speciality Handbook: Magnesium and Magnesium Alloys*; ASM International: Novelty, OH, USA, 1999; Volume 59, p. 60.
45. Gu, X.; Zheng, Y.; Cheng, Y.; Zhong, S.; Xi, T. In vitro corrosion and biocompatibility of binary magnesium alloys. *Biomaterials* **2009**, *30*, 484–498. [[CrossRef](#)] [[PubMed](#)]
46. Koç, E.; Kannan, M.B.; Ünal, M.; Candan, E. Influence of zinc on the microstructure, mechanical properties and in vitro corrosion behavior of magnesium–zinc binary alloys. *J. Alloys Compd.* **2015**, *648*, 291–296. [[CrossRef](#)]
47. Song, Y.; Han, E.-H.; Shan, D.; Yim, C.D.; You, B.S. The role of second phases in the corrosion behavior of Mg–5Zn alloy. *Corros. Sci.* **2012**, *60*, 238–245. [[CrossRef](#)]
48. Bakhsheshi-Rad, H.; Hamzah, E.; Medraj, M.; Idris, M.; Lotfabadi, A.; Daroonparvar, M.; Yajid, M. Effect of heat treatment on the microstructure and corrosion behaviour of Mg–Zn alloys. *Mater. Corros.* **2014**, *65*, 999–1006. [[CrossRef](#)]
49. Kubasek, J.; Vojtěch, D. Structural characteristics and corrosion behavior of biodegradable Mg–Zn, Mg–Zn–Gd alloys. *J. Mater. Sci. Mater. Med.* **2013**, *24*, 1615–1626. [[CrossRef](#)] [[PubMed](#)]

50. Peng, Q.; Li, X.; Ma, N.; Liu, R.; Zhang, H. Effects of backward extrusion on mechanical and degradation properties of Mg–Zn biomaterial. *J. Mech. Behav. Biomed.* **2012**, *10*, 128–137. [[CrossRef](#)]
51. Rosalbino, F.; De Negri, S.; Saccone, A.; Angelini, E.; Delfino, S. Bio-corrosion characterization of Mg–Zn–X (X = Ca, Mn, Si) alloys for biomedical applications. *J. Mater. Sci. Mater. Med.* **2010**, *21*, 1091–1098. [[CrossRef](#)]
52. Zhang, E.; Yang, L. Microstructure, mechanical properties and bio-corrosion properties of Mg–Zn–Mn–Ca alloy for biomedical application. *Mater. Sci. Eng. A* **2008**, *497*, 111–118. [[CrossRef](#)]
53. Zhang, E.; He, W.; Du, H.; Yang, K. Microstructure, mechanical properties and corrosion properties of Mg–Zn–Y alloys with low Zn content. *Mater. Sci. Eng. A* **2008**, *488*, 102–111. [[CrossRef](#)]
54. Boehlert, C.; Knittel, K. The microstructure, tensile properties, and creep behavior of Mg–Zn alloys containing 0–4.4 wt.% Zn. *Mater. Sci. Eng. A* **2006**, *417*, 315–321. [[CrossRef](#)]
55. Yan, Y.; Cao, H.; Kang, Y.; Yu, K.; Xiao, T.; Luo, J.; Deng, Y.; Fang, H.; Xiong, H.; Dai, Y. Effects of Zn concentration and heat treatment on the microstructure, mechanical properties and corrosion behavior of as-extruded Mg–Zn alloys produced by powder metallurgy. *J. Alloys Compd.* **2017**, *693*, 1277–1289. [[CrossRef](#)]
56. Zhang, S.; Li, J.; Song, Y.; Zhao, C.; Zhang, X.; Xie, C.; Zhang, Y.; Tao, H.; He, Y.; Jiang, Y. In vitro degradation, hemolysis and MC3T3-E1 cell adhesion of biodegradable Mg–Zn alloy. *Mater. Sci. Eng. C* **2009**, *29*, 1907–1912.
57. Cao, F.; Shi, Z.; Song, G.-L.; Liu, M.; Atrens, A. Corrosion behaviour in salt spray and in 3.5% NaCl solution saturated with Mg(OH)₂ of as-cast and solution heat-treated binary Mg–X alloys: X = Mn, Sn, Ca, Zn, Al, Zr, Si, Sr. *Corros. Sci.* **2013**, *76*, 60–97. [[CrossRef](#)]
58. Liu, X.-B.; Shan, D.-Y.; Song, Y.-W.; Han, E.-H. Effects of heat treatment on corrosion behaviors of Mg–3Zn magnesium alloy. *T. Nonferr. Metal Soc.* **2010**, *20*, 1345–1350. [[CrossRef](#)]
59. Chen, X.-B.; Kirkland, N.; Krebs, H.; Thiriat, M.; Virtanen, S.; Nisbet, D.; Birbilis, N. In vitro corrosion survey of Mg–x Ca and Mg–3Zn–y Ca alloys with and without calcium phosphate conversion coatings. *Corros. Eng. Sci. Techn.* **2012**, *47*, 365–373. [[CrossRef](#)]
60. Zhang, S.; Zheng, Y.; Zhang, L.; Bi, Y.; Li, J.; Liu, J.; Yu, Y.; Guo, H.; Li, Y. In vitro and in vivo corrosion and histocompatibility of pure Mg and a Mg–6Zn alloy as urinary implants in rat model. *Mater. Sci. Eng. C* **2016**, *68*, 414–422.
61. Ha, H.-Y.; Kang, J.-Y.; Yang, J.; Yim, C.D.; You, B.S. Limitations in the use of the potentiodynamic polarisation curves to investigate the effect of Zn on the corrosion behaviour of as-extruded Mg–Zn binary alloy. *Corros. Sci.* **2013**, *75*, 426–433. [[CrossRef](#)]
62. Ralston, K.; Birbilis, N. Effect of grain size on corrosion: A review. *Corrosion* **2010**, *66*, 075005–075005-13. [[CrossRef](#)]
63. Op't Hoog, C.; Birbilis, N.; Estrin, Y. Corrosion of pure Mg as a function of grain size and processing route. *Adv. Eng. Mater.* **2008**, *10*, 579–582. [[CrossRef](#)]
64. Birbilis, N.; Zhang, M.X.; Estrin, Y. Surface grain size effects on the corrosion of magnesium. In *Key Engineering Materials*; Hoog, C.O.T., Birbilis, N., Zhang, M.X., Eds.; Trans Tech Publ.: Zürich, Switzerland, 2008; pp. 229–240.
65. Ambat, R.; Aung, N.N.; Zhou, W. Evaluation of microstructural effects on corrosion behaviour of AZ91D magnesium alloy. *Corros. Sci.* **2000**, *42*, 1433–1455. [[CrossRef](#)]
66. Ben-Hamu, G.; Eliezer, D.; Shin, K.; Cohen, S. The relation between microstructure and corrosion behavior of Mg–Y–RE–Zr alloys. *J. Alloys Compd.* **2007**, *431*, 269–276. [[CrossRef](#)]
67. Birbilis, N.; Ralston, K.; Virtanen, S.; Fraser, H.; Davies, C. Grain character influences on corrosion of ECAPed pure magnesium. *Corros. Eng. Sci. Techn.* **2010**, *45*, 224–230. [[CrossRef](#)]
68. Zhao, M.-C.; Liu, M.; Song, G.; Atrens, A. Influence of the β -phase morphology on the corrosion of the Mg alloy AZ91. *Corros. Sci.* **2008**, *50*, 1939–1953. [[CrossRef](#)]
69. Song, G.; Atrens, A.; Dargusch, M. Influence of microstructure on the corrosion of diecast AZ91D. *Corros. Sci.* **1998**, *41*, 249–273. [[CrossRef](#)]
70. Lu, Y.; Bradshaw, A.; Chiu, Y.; Jones, I. Effects of secondary phase and grain size on the corrosion of biodegradable Mg–Zn–Ca alloys. *Mater. Sci. Eng. C* **2015**, *48*, 480–486.
71. Jeong, Y.; Kim, W. Enhancement of mechanical properties and corrosion resistance of Mg–Ca alloys through microstructural refinement by indirect extrusion. *Corros. Sci.* **2014**, *82*, 392–403. [[CrossRef](#)]
72. Zhang, B.; Wang, Y.; Geng, L.; Lu, C. Effects of calcium on texture and mechanical properties of hot-extruded Mg–Zn–Ca alloys. *Mater. Sci. Eng. A* **2012**, *539*, 56–60. [[CrossRef](#)]

73. Fang, D.; Li, X.; Li, H.; Peng, Q. Electrochemical corrosion behavior of backward extruded Mg-Zn-Ca alloys in different media. *Int. J. Electrochem. Sci* **2013**, *8*, 2551–2565.
74. Bohlen, J.; Nürnberg, M.R.; Senn, J.W.; Letzig, D.; Agnew, S.R. The texture and anisotropy of magnesium–zinc–rare earth alloy sheets. *Acta Mater.* **2007**, *55*, 2101–2112. [[CrossRef](#)]
75. Zander, D.; Zumdick, N.A. Influence of Ca and Zn on the microstructure and corrosion of biodegradable Mg–Ca–Zn alloys. *Corros. Sci.* **2015**, *93*, 222–233. [[CrossRef](#)]
76. Cha, P.-R.; Han, H.-S.; Yang, G.-F.; Kim, Y.-C.; Hong, K.-H.; Lee, S.-C.; Jung, J.-Y.; Ahn, J.-P.; Kim, Y.-Y.; Cho, S.-Y. Biodegradability engineering of biodegradable Mg alloys: Tailoring the electrochemical properties and microstructure of constituent phases. *Sci. Rep.* **2013**, *3*, 2367. [[CrossRef](#)] [[PubMed](#)]
77. Südholz, A.; Kirkland, N.; Buchheit, R.; Birbilis, N. Electrochemical properties of intermetallic phases and common impurity elements in magnesium alloys. *Electrochem. Solid-State Lett.* **2011**, *14*, C5–C7.
78. Gao, X.; Zhu, S.; Muddle, B.; Nie, J. Precipitation-hardened Mg–Ca–Zn alloys with superior creep resistance. *Scripta Mater.* **2005**, *53*, 1321–1326. [[CrossRef](#)]
79. Oh, J.; Ohkubo, T.; Mukai, T.; Hono, K. TEM and 3DAP characterization of an age-hardened Mg–Ca–Zn alloy. *Scripta Mater.* **2005**, *53*, 675–679. [[CrossRef](#)]
80. Liu, D.; Guo, C.; Chai, L.; Sherman, V.R.; Qin, X.; Ding, Y.; Meyers, M.A. Mechanical properties and corrosion resistance of hot extruded Mg–2.5 Zn–1Ca alloy. *Mater. Sci. Eng. B* **2015**, *195*, 50–58. [[CrossRef](#)]
81. Chino, Y.; Kobata, M.; Iwasaki, H.; Mabuchi, M. Tensile properties from room temperature to 673 K of Mg–0.9 mass% Ca alloy containing lamella Mg₂Ca. *Mater. Trans.* **2002**, *43*, 2643–2646. [[CrossRef](#)]
82. Jang, Y.; Tan, Z.; Jurey, C.; Xu, Z.; Dong, Z.; Collins, B.; Yun, Y.; Sankar, J. Understanding corrosion behavior of Mg–Zn–Ca alloys from subcutaneous mouse model: Effect of Zn element concentration and plasma electrolytic oxidation. *Mater. Sci. Eng. C* **2015**, *48*, 28–40.
83. Shao, G.; Varsani, V.; Fan, Z. Thermodynamic modelling of the Y–Zn and Mg–Zn–Y systems. *Calphad* **2006**, *30*, 286–295. [[CrossRef](#)]
84. Lee, J.Y.; Kim, D.H.; Lim, H.K.; Kim, D.H. Effects of Zn/Y ratio on microstructure and mechanical properties of Mg–Zn–Y alloys. *Mater. Lett.* **2005**, *59*, 3801–3805. [[CrossRef](#)]
85. Nam, S.; Kim, W.; Kim, D.; Kim, T. Microstructure and corrosion behavior of rapidly solidified Mg–Zn–Y alloys. *Met. Mater. Int.* **2013**, *19*, 205–209. [[CrossRef](#)]
86. Asgharzadeh, H.; Yoon, E.; Chae, H.; Kim, T.; Lee, J.; Kim, H. Microstructure and mechanical properties of a Mg–Zn–Y alloy produced by a powder metallurgy route. *J. Alloys Compd.* **2014**, *586*, S95–S100. [[CrossRef](#)]
87. Zhang, J.; Xu, J.; Cheng, W.; Chen, C.; Kang, J. Corrosion behavior of Mg–Zn–Y alloy with long-period stacking ordered structures. *J. Mater. Sci. Technol.* **2012**, *28*, 1157–1162. [[CrossRef](#)]
88. Li, C.; Xu, D.; Zeng, Z.; Wang, B.; Sheng, L.; Chen, X.-B.; Han, E. Effect of volume fraction of LPSO phases on corrosion and mechanical properties of Mg–Zn–Y alloys. *Mater. Des.* **2017**, *121*, 430–441. [[CrossRef](#)]
89. Zhao, X.; Shi, L.-l.; Xu, J. Mg–Zn–Y alloys with long-period stacking ordered structure: In vitro assessments of biodegradation behavior. *Mater. Sci. Eng. C* **2013**, *33*, 3627–3637.
90. Bae, D.; Lee, M.; Kim, K.; Kim, W.; Kim, D. Application of quasicrystalline particles as a strengthening phase in Mg–Zn–Y alloys. *J. Alloys Compd.* **2002**, *342*, 445–450. [[CrossRef](#)]
91. Xu, D.; Han, E. Effects of icosahedral phase formation on the microstructure and mechanical improvement of Mg alloys: A review. *Progr. Nat. Sci.* **2012**, *22*, 364–385. [[CrossRef](#)]
92. Singh, A.; Watanabe, M.; Kato, A.; Tsai, A. Microstructure and strength of quasicrystal containing extruded Mg–Zn–Y alloys for elevated temperature application. *Mater. Sci. Eng. A* **2004**, *385*, 382–396. [[CrossRef](#)]
93. Bae, D.; Kim, S.; Kim, D.; Kim, W. Deformation behavior of Mg–Zn–Y alloys reinforced by icosahedral quasicrystalline particles. *Acta Mater.* **2002**, *50*, 2343–2356. [[CrossRef](#)]
94. Chino, Y.; Sassa, K.; Mabuchi, M. Texture and stretch formability of a rolled Mg–Zn alloy containing dilute content of Y. *Mater. Sci. Eng. A* **2009**, *513*, 394–400. [[CrossRef](#)]
95. Lu, F.; Ma, A.; Jiang, J.; Yang, D.; Zhou, Q. Review on long-period stacking-ordered structures in Mg–Zn–RE alloys. *Rare Metals* **2012**, *31*, 303–310. [[CrossRef](#)]
96. Zhao, X.; Shi, L.-l.; Xu, J. Biodegradable Mg–Zn–Y alloys with long-period stacking ordered structure: Optimization for mechanical properties. *J. Mech. Behav. Biomed.* **2013**, *18*, 181–190. [[CrossRef](#)] [[PubMed](#)]
97. Itoi, T.; Inazawa, T.; Yamasaki, M.; Kawamura, Y.; Hirohashi, M. Microstructure and mechanical properties of Mg–Zn–Y alloy sheet prepared by hot-rolling. *Mater. Sci. Eng. A* **2013**, *560*, 216–223. [[CrossRef](#)]

98. Kawamura, Y.; Yamasaki, M. Formation and mechanical properties of Mg₉₇Zn₁RE₂ alloys with long-period stacking ordered structure. *Mater. Trans.* **2007**, *48*, 2986–2992. [[CrossRef](#)]
99. Yoshimoto, S.; Yamasaki, M.; Kawamura, Y. Microstructure and mechanical properties of extruded Mg-Zn-Y alloys with 14H long period ordered structure. *Mater. Trans.* **2006**, *47*, 959–965. [[CrossRef](#)]
100. Chen, B.; Lin, D.; Zeng, X.; Lu, C. Effects of yttrium and zinc addition on the microstructure and mechanical properties of Mg-Y-Zn alloys. *J. Mater. Sci. Mater. Med.* **2010**, *45*, 2510–2517. [[CrossRef](#)]
101. Itoi, T.; Suzuki, T.; Kawamura, Y.; Hirohashi, M. Microstructure and mechanical properties of Mg-Zn-Y rolled sheet with a Mg₁₂ZnY phase. *Mater. Trans.* **2010**, *51*, 1536–1542. [[CrossRef](#)]
102. Chen, B.; Lin, D.; Zeng, X.; Lu, C. Microstructure and mechanical properties of ultrafine grained Mg₉₇Y₂Zn₁ alloy processed by equal channel angular pressing. *J. Alloys Compd.* **2007**, *440*, 94–100. [[CrossRef](#)]
103. Kawamura, Y.; Hayashi, K.; Inoue, A.; Masumoto, T. Rapidly solidified powder metallurgy Mg₉₇Zn₁Y₂Alloys with excellent tensile yield strength above 600 MPa. *Mater. Trans.* **2001**, *42*, 1172–1176. [[CrossRef](#)]
104. Matsuda, M.; Ando, S.; Nishida, M. Dislocation structure in rapidly solidified Mg₉₇Zn₁Y₂ alloy with long period stacking order phase. *Mater. Trans.* **2005**, *46*, 361–364. [[CrossRef](#)]
105. Shao, X.; Yang, Z.; Ma, X. Strengthening and toughening mechanisms in Mg-Zn-Y alloy with a long period stacking ordered structure. *Acta Mater.* **2010**, *58*, 4760–4771. [[CrossRef](#)]
106. Hagihara, K.; Yokotani, N.; Umakoshi, Y. Plastic deformation behavior of Mg₁₂YZn with 18R long-period stacking ordered structure. *Intermetallics* **2010**, *18*, 267–276. [[CrossRef](#)]
107. Mora, E.; Garcés, G.; Onorbe, E.; Pérez, P.; Adeva, P. High-strength Mg-Zn-Y alloys produced by powder metallurgy. *Scripta Mater.* **2009**, *60*, 776–779. [[CrossRef](#)]
108. Lee, J.Y.; Lim, H.K.; Kim, D.H.; Kim, W.T.; Kim, D.H. Effect of volume fraction of quasicrystal on the mechanical properties of quasicrystal-reinforced Mg-Zn-Y alloys. *Mater. Sci. Eng. A* **2007**, *449*, 987–990. [[CrossRef](#)]
109. Liu, D.-B.; Wu, B.; Wang, X.; Chen, M.-F. Corrosion and wear behavior of an Mg-2Zn-0.2 Mn alloy in simulated body fluid. *Rare Metals* **2015**, *34*, 553–559. [[CrossRef](#)]
110. Yin, D.-s.; Zhang, E.-l.; Zeng, S.-y. Effect of Zn on mechanical property and corrosion property of extruded Mg-Zn-Mn alloy. *T. Nonferr. Metal Soc.* **2008**, *18*, 763–768. [[CrossRef](#)]
111. Zhang, H.; Zhang, D.; Ma, C.; Guo, S. Improving mechanical properties and corrosion resistance of Mg-6Zn-Mn magnesium alloy by rapid solidification. *Mater. Lett.* **2013**, *92*, 45–48. [[CrossRef](#)]
112. Rosalbino, F.; De Negri, S.; Scavino, G.; Saccone, A. Microstructure and in vitro degradation performance of Mg-Zn-Mn alloys for biomedical application. *J. Biomed. Mater. Res. A* **2013**, *101*, 704–711. [[CrossRef](#)]
113. Abidin, N.I.Z.; Atrens, A.D.; Martin, D.; Atrens, A. Corrosion of high purity Mg, Mg₂Zn_{0.2}Mn, ZE41 and AZ91 in Hank's solution at 37 °C. *Corros. Sci.* **2011**, *53*, 3542–3556. [[CrossRef](#)]
114. Ben-Hamu, G.; Eliezer, D.; Shin, K. The role of Mg₂Si on the corrosion behavior of wrought Mg-Zn-Mn alloy. *Intermetallics* **2008**, *16*, 860–867. [[CrossRef](#)]
115. Lisitsyn, V.; Ben-Hamu, G.; Eliezer, D.; Shin, K. The role of Ca microalloying on the microstructure and corrosion behavior of Mg-6Zn-Mn-(0.5–2) Si alloys. *Corros. Sci.* **2009**, *51*, 776–784. [[CrossRef](#)]
116. Lisitsyn, V.; Ben-Hamu, G.; Eliezer, D.; Shin, K. Some particularities of the corrosion behaviour of Mg-Zn-Mn-Si-Ca alloys in alkaline chloride solutions. *Corros. Sci.* **2010**, *52*, 2280–2290. [[CrossRef](#)]
117. Dinodi, N.; Shetty, A.N. Electrochemical investigations on the corrosion behaviour of magnesium alloy ZE41 in a combined medium of chloride and sulphate. *J. Magnes. Alloys* **2013**, *1*, 201–209. [[CrossRef](#)]
118. Zhao, M.C.; Liu, M.; Song, G.-L.; Atrens, A. Influence of Microstructure on Corrosion of As-cast ZE41. *Adv. Eng. Mater.* **2008**, *10*, 104–111. [[CrossRef](#)]
119. Zhao, M.-C.; Liu, M.; Song, G.-L.; Atrens, A. Influence of pH and chloride ion concentration on the corrosion of Mg alloy ZE41. *Corros. Sci.* **2008**, *50*, 3168–3178. [[CrossRef](#)]
120. Kannan, M.B.; Blawert, C.; Dietzel, W. Electrochemical corrosion behaviour of ZE41 and QE22 magnesium alloys. In *Materials Science Forum*; Dieringa, H., Hort, N., Kainer, K.U., Eds.; Trans Tech Publ.: Zürich, Switzerland, 2011; pp. 385–388.
121. Neil, W.; Forsyth, M.; Howlett, P.; Hutchinson, C.; Hinton, B. Corrosion of magnesium alloy ZE41—The role of microstructural features. *Corros. Sci.* **2009**, *51*, 387–394. [[CrossRef](#)]
122. Neil, W.; Forsyth, M.; Howlett, P.; Hutchinson, C.; Hinton, B. Corrosion of heat treated magnesium alloy ZE41. *Corros. Sci.* **2011**, *53*, 3299–3308. [[CrossRef](#)]
123. Coy, A.; Viejo, F.; Skeldon, P.; Thompson, G. Susceptibility of rare-earth-magnesium alloys to micro-galvanic corrosion. *Corros. Sci.* **2010**, *52*, 3896–3906. [[CrossRef](#)]

124. Jamesh, M.I.; Wu, G.; Zhao, Y.; McKenzie, D.R.; Bilek, M.M.; Chu, P.K. Electrochemical corrosion behavior of biodegradable Mg–Y–RE and Mg–Zn–Zr alloys in Ringer’s solution and simulated body fluid. *Corros. Sci.* **2015**, *91*, 160–184. [[CrossRef](#)]
125. Huan, Z.; Leeftang, M.; Zhou, J.; Fratila-Apachitei, L.; Duszczyc, J. In vitro degradation behavior and cytocompatibility of Mg–Zn–Zr alloys. *J. Mater. Sci. Mater. Med.* **2010**, *21*, 2623–2635. [[CrossRef](#)]
126. Gu, X.; Li, N.; Zheng, Y.; Ruan, L. In vitro degradation performance and biological response of a Mg–Zn–Zr alloy. *Mater. Sci. Eng. B* **2011**, *176*, 1778–1784. [[CrossRef](#)]
127. Witte, F.; Kaese, V.; Haferkamp, H.; Switzer, E.; Meyer-Lindenberg, A.; Wirth, C.; Windhagen, H. In vivo corrosion of four magnesium alloys and the associated bone response. *Biomaterials* **2005**, *26*, 3557–3563. [[CrossRef](#)] [[PubMed](#)]
128. Gao, J.-C.; Sha, W.; Qiao, L.-Y.; Yong, W. Corrosion behavior of Mg and Mg–Zn alloys in simulated body fluid. *T. Nonferr. Metal Soc.* **2008**, *18*, 588–592. [[CrossRef](#)]
129. Chang, J.-W.; Duo, J.; Xiang, Y.-Z.; Yang, H.-Y.; Ding, W.-J.; Peng, Y.-H. Influence of Nd and Y additions on the corrosion behaviour of extruded Mg–Zn–Zr alloys. *Int. J. Min. Metal Mater.* **2011**, *18*, 203. [[CrossRef](#)]
130. Campos, M.D.R.S.; del Rosario, M. *The Role of Intermetallic Phases in the Corrosion of Magnesium–Rare Earth Alloys*; Technische Universität Hamburg-Harburg: Hamburg, Germany, 2016.
131. Liu, L.; Chen, X.; Pan, F.; Wang, Z.; Liu, W.; Cao, P.; Yan, T.; Xu, X. Effect of Y and Ce additions on microstructure and mechanical properties of Mg–Zn–Zr alloys. *Mater. Sci. Eng. A* **2015**, *644*, 247–253. [[CrossRef](#)]
132. Wu, W.; Wang, Y.; Zeng, X.; Chen, L.; Liu, Z. Effect of neodymium on mechanical behavior of Mg–Zn–Zr magnesium alloy. *J. Mater. Sci. Lett.* **2003**, *22*, 445–447. [[CrossRef](#)]
133. Yu, H.; Hongge, Y.; Jihua, C.; Bin, S.; Yi, Z.; Yanjin, S.; Zhaojie, M. Effects of minor Gd addition on microstructures and mechanical properties of the high strain-rate rolled Mg–Zn–Zr alloys. *J. Alloys Compd.* **2014**, *586*, 757–765. [[CrossRef](#)]
134. Wang, J.; Song, P.; Gao, S.; Wei, Y.; Pan, F. Influence of Y on the phase composition and mechanical properties of as-extruded Mg–Zn–Y–Zr magnesium alloys. *J. Mater. Sci. Mater. Med.* **2012**, *47*, 2005–2010. [[CrossRef](#)]
135. He, S.; Peng, L.; Zeng, X.; Ding, W.; Zhu, Y. Comparison of the microstructure and mechanical properties of a ZK60 alloy with and without 1.3 wt.% gadolinium addition. *Mater. Sci. Eng. A* **2006**, *433*, 175–181. [[CrossRef](#)]
136. Li, Q.; Wang, Q.; Wang, Y.; Zeng, X.; Ding, W. Effect of Nd and Y addition on microstructure and mechanical properties of as-cast Mg–Zn–Zr alloy. *J. Alloys Compd.* **2007**, *427*, 115–123. [[CrossRef](#)]
137. Liu, Y.; Yuan, G.; Zhang, S.; Zhang, X.; Lu, C.; Ding, W. Effects of Zn/Gd ratio and content of Zn, Gd on phase constitutions of Mg alloys. *Mater. Trans.* **2008**, *49*, 941–944. [[CrossRef](#)]
138. Yang, J.; Xiao, W.; Wang, L.; Wu, Y.; Wang, L.; Zhang, H. Influences of Gd on the microstructure and strength of Mg–4.5 Zn alloy. *Mater. Charact.* **2008**, *59*, 1667–1674. [[CrossRef](#)]
139. Yang, J.; Wang, L.; Wang, L.; Zhang, H. Microstructures and mechanical properties of the Mg–4.5 Zn–xGd (x = 0, 2, 3 and 5) alloys. *J. Alloys Compd.* **2008**, *459*, 274–280. [[CrossRef](#)]
140. Li, H.; Peng, Q.; Li, X.; Li, K.; Han, Z.; Fang, D. Microstructures, mechanical and cytocompatibility of degradable Mg–Zn based orthopedic biomaterials. *Mater. Des.* **2014**, *58*, 43–51. [[CrossRef](#)]
141. Lai, H.; Li, J.; Li, J.; Zhang, Y.; Xu, Y. Effects of Sr on the microstructure, mechanical properties and corrosion behavior of Mg–2Zn–xSr alloys. *J. Mater. Sci. Mater. Med.* **2018**, *29*, 87. [[CrossRef](#)] [[PubMed](#)]
142. Guan, R.-G.; Cipriano, A.F.; Zhao, Z.-Y.; Lock, J.; Tie, D.; Zhao, T.; Cui, T.; Liu, H. Development and evaluation of a magnesium–zinc–strontium alloy for biomedical applications—Alloy processing, microstructure, mechanical properties, and biodegradation. *Mater. Sci. Eng. C* **2013**, *33*, 3661–3669. [[CrossRef](#)]
143. Brar, H.S.; Wong, J.; Manuel, M.V. Investigation of the mechanical and degradation properties of Mg–Sr and Mg–Zn–Sr alloys for use as potential biodegradable implant materials. *J. Mech. Behav. Biomed.* **2012**, *7*, 87–95. [[CrossRef](#)] [[PubMed](#)]
144. Ben-Hamu, G.; Eliezer, D.; Kaya, A.; Na, Y.; Shin, K. Microstructure and corrosion behavior of Mg–Zn–Ag alloys. *Mater. Sci. Eng. A* **2006**, *435*, 579–587. [[CrossRef](#)]
145. Lotfpour, M.; Emamy, M.; Dehghanian, C.; Tavighi, K. Influence of Cu addition on the structure, mechanical and corrosion properties of Cast Mg–2% Zn alloy. *J. Mater. Eng. Perform.* **2017**, *26*, 2136–2150. [[CrossRef](#)]
146. Liu, R.; Zeng, Z.; Scully, J.; Williams, G.; Birbilis, N. Simultaneously improving the corrosion resistance and strength of magnesium via low levels of Zn and Ge additions. *Corros. Sci.* **2018**, *140*, 18–29. [[CrossRef](#)]

147. Jiang, P.; Blawert, C.; Hou, R.; Scharnagl, N.; Bohlen, J.; Zheludkevich, M.L. Microstructural influence on corrosion behavior of MgZnGe alloy in NaCl solution. *J. Alloys Compd.* **2019**, *783*, 179–192. [[CrossRef](#)]
148. Johnston, S.; Shi, Z.; Atrons, A. The influence of pH on the corrosion rate of high-purity Mg, AZ91 and ZE41 in bicarbonate buffered Hanks' solution. *Corros. Sci.* **2015**, *101*, 182–192. [[CrossRef](#)]
149. Taltavull, C.; Shi, Z.; Torres, B.; Rams, J.; Atrons, A. Influence of the chloride ion concentration on the corrosion of high-purity Mg, ZE41 and AZ91 in buffered Hank's solution. *J. Mater. Sci. Mater. Med.* **2014**, *25*, 329–345. [[CrossRef](#)] [[PubMed](#)]
150. Dinodi, N.; Shetty, A.N. Investigation of influence of medium pH and sulfate ion concentrations on corrosion behavior of magnesium alloy ZE41. *Surf. Eng. Appl. Elect.* **2014**, *50*, 149–156. [[CrossRef](#)]
151. Natarajan, S.; Ravikiran, V. Evaluation of electrochemical and surface characteristics of conversion coatings on ZM21 magnesium alloy. *Surf. Eng.* **2006**, *22*, 287–293. [[CrossRef](#)]
152. Martin, H.J.; Horstemeyer, M.; Wang, P.T. Comparison of corrosion pitting under immersion and salt-spray environments on an as-cast AE44 magnesium alloy. *Corros. Sci.* **2010**, *52*, 3624–3638. [[CrossRef](#)]
153. Song, W.; Martin, H.J.; Hicks, A.; Seely, D.; Walton, C.A.; Lawrimore, W.B., II; Wang, P.T.; Horstemeyer, M. Corrosion behaviour of extruded AM30 magnesium alloy under salt-spray and immersion environments. *Corros. Sci.* **2014**, *78*, 353–368. [[CrossRef](#)]
154. Walton, C.A.; Martin, H.J.; Horstemeyer, M.; Wang, P.T. Quantification of corrosion mechanisms under immersion and salt-spray environments on an extruded AZ31 magnesium alloy. *Corros. Sci.* **2012**, *56*, 194–208. [[CrossRef](#)]
155. Zhao, M.-C.; Schmutz, P.; Brunner, S.; Liu, M.; Song, G.-l.; Atrons, A. An exploratory study of the corrosion of Mg alloys during interrupted salt spray testing. *Corros. Sci.* **2009**, *51*, 1277–1292. [[CrossRef](#)]
156. Gonzalez, J.; Hou, R.Q.; Nidadavolu, E.P.; Willumeit-Römer, R.; Feyerabend, F. Magnesium degradation under physiological conditions—Best practice. *Bioact. Mater.* **2018**, *3*, 174–185. [[CrossRef](#)]
157. Walker, J.; Shadanbaz, S.; Kirkland, N.T.; Stace, E.; Woodfield, T.; Staiger, M.P.; Dias, G.J. Magnesium alloys: Predicting in vivo corrosion with in vitro immersion testing. *J. Biomed. Mater. Res. B Appl. Biomater.* **2012**, *100*, 1134–1141. [[CrossRef](#)]
158. Hänni, A.C.; Gerber, I.; Schinhammer, M.; Löffler, J.F.; Uggowitzer, P.J. On the in vitro and in vivo degradation performance and biological response of new biodegradable Mg–Y–Zn alloys. *Acta Biomater.* **2010**, *6*, 1824–1833. [[CrossRef](#)] [[PubMed](#)]
159. Sanchez, A.H.M.; Luthringer, B.J.; Feyerabend, F.; Willumeit, R. Mg and Mg alloys: How comparable are in vitro and in vivo corrosion rates? A review. *Acta Biomater.* **2015**, *13*, 16–31. [[CrossRef](#)] [[PubMed](#)]
160. Zhang, S.; Zhang, X.; Zhao, C.; Li, J.; Song, Y.; Xie, C.; Tao, H.; Zhang, Y.; He, Y.; Jiang, Y. Research on an Mg–Zn alloy as a degradable biomaterial. *Acta Biomater.* **2010**, *6*, 626–640. [[CrossRef](#)] [[PubMed](#)]
161. Seuss, F.; Seuss, S.; Turhan, M.; Fabry, B.; Virtanen, S. Corrosion of Mg alloy AZ91D in the presence of living cells. *J. Biomed. Mater. Res. B Appl. Biomater.* **2011**, *99*, 276–281. [[CrossRef](#)] [[PubMed](#)]
162. Hou, R.; Willumeit-Römer, R.; Garamus, V.M.; Frant, M.; Koll, J.; Feyerabend, F. Adsorption of Proteins on Degradable Magnesium—Which Factors are Relevant? *ACS Appl. Mater. Inter.* **2018**, *10*, 42175–42185. [[CrossRef](#)]
163. Willumeit, R.; Fischer, J.; Feyerabend, F.; Hort, N.; Bismayer, U.; Heidrich, S.; Mihailova, B. Chemical surface alteration of biodegradable magnesium exposed to corrosion media. *Acta Biomater.* **2011**, *7*, 2704–2715. [[CrossRef](#)]
164. Yamamoto, A.; Hiromoto, S. Effect of inorganic salts, amino acids and proteins on the degradation of pure magnesium in vitro. *Mater. Sci. Eng. C* **2009**, *29*, 1559–1568. [[CrossRef](#)]
165. Raman, R.S.; Jafari, S.; Harandi, S.E. Corrosion fatigue fracture of magnesium alloys in bioimplant applications: A review. *Eng. Fract. Mech.* **2015**, *137*, 97–108. [[CrossRef](#)]
166. Gu, X.; Zhou, W.; Zheng, Y.; Cheng, Y.; Wei, S.; Zhong, S.; Xi, T.; Chen, L. Corrosion fatigue behaviors of two biomedical Mg alloys—AZ91D and WE43—in simulated body fluid. *Acta Biomater.* **2010**, *6*, 4605–4613. [[CrossRef](#)]
167. Bian, D.; Zhou, W.; Liu, Y.; Li, N.; Zheng, Y.; Sun, Z. Fatigue behaviors of HP-Mg, Mg–Ca and Mg–Zn–Ca biodegradable metals in air and simulated body fluid. *Acta Biomater.* **2016**, *41*, 351–360. [[CrossRef](#)]
168. Shi, Z.; Hofstetter, J.; Cao, F.; Uggowitzer, P.J.; Dargusch, M.S.; Atrons, A. Corrosion and stress corrosion cracking of ultra-high-purity Mg5Zn. *Corros. Sci.* **2015**, *93*, 330–335. [[CrossRef](#)]

169. Choudhary, L.; Raman, R.S. Mechanical integrity of magnesium alloys in a physiological environment: Slow strain rate testing based study. *Eng. Fract. Mech.* **2013**, *103*, 94–102. [[CrossRef](#)]
170. Winzer, N.; Atrens, A.; Dietzel, W.; Song, G.; Kainer, K. Stress corrosion cracking in magnesium alloys: Characterization and prevention. *JOM* **2007**, *59*, 49–53. [[CrossRef](#)]
171. Prabhu, D.B.; Dhamotharan, S.; Kumar, G.S.; Gopalakrishnan, P.; Ravi, K. Stress corrosion cracking of biodegradable Mg-4Zn alloy in simulated body fluid at different strain rates—a fractographic investigation. *Mater. Sci. Eng. A* **2018**. [[CrossRef](#)]
172. Jafari, S.; Raman, R.S.; Davies, C.H. Stress corrosion cracking of an extruded magnesium alloy (ZK21) in a simulated body fluid. *Eng. Fract. Mech.* **2018**, *201*, 47–55. [[CrossRef](#)]
173. Yuan, G.; Liu, Y.; Ding, W.; Lu, C. Effects of extrusion on the microstructure and mechanical properties of Mg–Zn–Gd alloy reinforced with quasicrystalline particles. *Mater. Sci. Eng. A* **2008**, *474*, 348–354. [[CrossRef](#)]
174. Shi, Z.; Song, G.; Atrens, A. Corrosion resistance of anodised single-phase Mg alloys. *Surf. Coat. Technol.* **2006**, *201*, 492–503. [[CrossRef](#)]
175. Zhang, J.; Ma, Q.; Pan, F. Effects of trace Er addition on the microstructure and mechanical properties of Mg–Zn–Zr alloy. *Mater. Des.* **2010**, *31*, 4043–4049. [[CrossRef](#)]
176. Ibrahim, H.; Klarner, A.D.; Poorganji, B.; Dean, D.; Luo, A.A.; Elahinia, M. Microstructural, mechanical and corrosion characteristics of heat-treated Mg-1.2 Zn-0.5 Ca (wt%) alloy for use as resorbable bone fixation material. *J. Mech. Behav. Biomed.* **2017**, *69*, 203–212. [[CrossRef](#)]
177. Xu, D.; Han, E.-H.; Liu, L.; Xu, Y. Influence of higher Zn/Y ratio on the microstructure and mechanical properties of Mg–Zn–Y–Zr alloys. *Metall. Mater. Trans. A* **2009**, *40*, 1727–1740. [[CrossRef](#)]
178. Singh, A.; Somekawa, H.; Mukai, T. Compressive strength and yield asymmetry in extruded Mg–Zn–Ho alloys containing quasicrystal phase. *Scripta Mater.* **2007**, *56*, 935–938. [[CrossRef](#)]
179. Park, S.H.; You, B.S.; Mishra, R.K.; Sachdev, A.K. Effects of extrusion parameters on the microstructure and mechanical properties of Mg–Zn–(Mn)–Ce/Gd alloys. *Mater. Sci. Eng. A* **2014**, *598*, 396–406. [[CrossRef](#)]
180. Zeng, X.; Zhang, Y.; Lu, C.; Ding, W.; Wang, Y.; Zhu, Y. Precipitation behavior and mechanical properties of a Mg–Zn–Y–Zr alloy processed by thermo-mechanical treatment. *J. Alloys Compd.* **2005**, *395*, 213–219. [[CrossRef](#)]
181. Kim, I.; Bae, D.; Kim, D. Precipitates in a Mg–Zn–Y alloy reinforced by an icosahedral quasicrystalline phase. *Mater. Sci. Eng. A* **2003**, *359*, 313–318. [[CrossRef](#)]
182. Mackenzie, L.; Davis, B.; Humphreys, F.; Lorimer, G. The deformation, recrystallisation and texture of three magnesium alloy extrusions. *Mater. Sci. Technol.* **2007**, *23*, 1173–1180. [[CrossRef](#)]
183. Agnew, S.; Horton, J.; Lillo, T.; Brown, D. Enhanced ductility in strongly textured magnesium produced by equal channel angular processing. *Scripta Mater.* **2004**, *50*, 377–381. [[CrossRef](#)]
184. Chino, Y.; Lee, J.-S.; Sassa, K.; Kamiya, A.; Mabuchi, M. Press formability of a rolled AZ31 Mg alloy sheet with controlled texture. *Mater. Lett.* **2006**, *60*, 173–176. [[CrossRef](#)]
185. Yan, H.; Chen, R.; Han, E. Room-temperature ductility and anisotropy of two rolled Mg–Zn–Gd alloys. *Mater. Sci. Eng. A* **2010**, *527*, 3317–3322. [[CrossRef](#)]
186. Lee, J.-Y.; Yun, Y.-S.; Suh, B.-C.; Kim, N.-J.; Kim, W.-T.; Kim, D.-H. Comparison of static recrystallization behavior in hot rolled Mg–3Al–1Zn and Mg–3Zn–0.5 Ca sheets. *J. Alloys Compd.* **2014**, *589*, 240–246. [[CrossRef](#)]
187. Nayak, S.; Bhushan, B.; Jayaganthan, R.; Gopinath, P.; Agarwal, R.; Lahiri, D. Strengthening of Mg based alloy through grain refinement for orthopaedic application. *J. Mech. Behav. Biomed.* **2016**, *59*, 57–70. [[CrossRef](#)]
188. Jiang, J.; Aibin, M.; Saito, N.; Zhixin, S.; Dan, S.; Fumin, L.; Nishida, Y.; Donghui, Y.; Pinghua, L. Improving corrosion resistance of RE-containing magnesium alloy ZE41A through ECAP. *J. Rare Earth.* **2009**, *27*, 848–852. [[CrossRef](#)]
189. Mostaed, E.; Hashempour, M.; Fabrizi, A.; Dellasega, D.; Bestetti, M.; Bonollo, F.; Vedani, M. Microstructure, texture evolution, mechanical properties and corrosion behavior of ECAP processed ZK60 magnesium alloy for biodegradable applications. *J. Mech. Behav. Biomed.* **2014**, *37*, 307–322. [[CrossRef](#)]
190. Zheng, M.Y.; Xu, S.W.; Qiao, X.G.; Gan, W.M.; Wu, K.; Kamado, S.; Kojima, Y.; Brokmeier, H.G. Equal channel angular pressing of magnesium alloy containing quasicrystal phase. In *Materials Science Forum*; Horita, Z., Ed.; Trans Tech Publ.: Zürich, Switzerland, 2006; pp. 527–532.

191. Mostaed, E.; Vedani, M.; Hashempour, M.; Bestetti, M. Influence of ECAP process on mechanical and corrosion properties of pure Mg and ZK60 magnesium alloy for biodegradable stent applications. *Biomaterials* **2014**, *4*, e28283. [[CrossRef](#)]
192. Tong, L.; Zheng, M.; Chang, H.; Hu, X.; Wu, K.; Xu, S.; Kamado, S.; Kojima, Y. Microstructure and mechanical properties of Mg–Zn–Ca alloy processed by equal channel angular pressing. *Mater. Sci. Eng. A* **2009**, *523*, 289–294. [[CrossRef](#)]
193. Tong, L.; Zheng, M.; Hu, X.; Wu, K.; Xu, S.; Kamado, S.; Kojima, Y. Influence of ECAP routes on microstructure and mechanical properties of Mg–Zn–Ca alloy. *Mater. Sci. Eng. A* **2010**, *527*, 4250–4256. [[CrossRef](#)]
194. Stolyarov, V.V.; Zhu, Y.T.; Alexandrov, I.V.; Lowe, T.C.; Valiev, R.Z. Influence of ECAP routes on the microstructure and properties of pure Ti. *Mater. Sci. Eng. A* **2001**, *299*, 59–67. [[CrossRef](#)]
195. Witte, F.; Feyerabend, F.; Maier, P.; Fischer, J.; Störmer, M.; Blawert, C.; Dietzel, W.; Hort, N. Biodegradable magnesium–hydroxyapatite metal matrix composites. *Biomaterials* **2007**, *28*, 2163–2174. [[CrossRef](#)] [[PubMed](#)]
196. Poddar, P.; Srivastava, V.; De, P.; Sahoo, K. Processing and mechanical properties of SiC reinforced cast magnesium matrix composites by stir casting process. *Mater. Sci. Eng. A* **2007**, *460*, 357–364. [[CrossRef](#)]
197. Saravanan, R.; Surappa, M. Fabrication and characterisation of pure magnesium-30 vol.% SiCP particle composite. *Mater. Sci. Eng. A* **2000**, *276*, 108–116. [[CrossRef](#)]
198. Nunez-Lopez, C.; Skeldon, P.; Thompson, G.; Lyon, P.; Karimzadeh, H.; Wilks, T. The corrosion behaviour of Mg alloy ZC71/SiCp metal matrix composite. *Corros. Sci.* **1995**, *37*, 689–708. [[CrossRef](#)]
199. Nunez-Lopez, C.; Habazaki, H.; Skeldon, P.; Thompson, G.; Karimzadeh, H.; Lyon, P.; Wilks, T. An investigation of microgalvanic corrosion using a model magnesium-silicon carbide metal matrix composite. *Corros. Sci.* **1996**, *38*, 1721–1729. [[CrossRef](#)]
200. Zucchi, F.; TrabANELLI, G.; Grassi, V.; Frignani, A. Corrosion behavior in sodium sulfate and sodium chloride solutions of SiCp reinforced magnesium alloy metal matrix composites. *Corrosion* **2004**, *60*, 362–368. [[CrossRef](#)]
201. Feng, A.; Han, Y. Mechanical and in vitro degradation behavior of ultrafine calcium polyphosphate reinforced magnesium-alloy composites. *Mater. Des.* **2011**, *32*, 2813–2820. [[CrossRef](#)]
202. Nieh, T.; Schwartz, A.; Wadsworth, J. Superplasticity in a 17 vol.% SiC particulate-reinforced ZK60A magnesium composite (ZK60/SiC/17p). *Mater. Sci. Eng. A* **1996**, *208*, 30–36. [[CrossRef](#)]
203. Lianxi, H.; Erde, W. Fabrication and mechanical properties of SiCw/ZK51A magnesium matrix composite by two-step squeeze casting. *Mater. Sci. Eng. A* **2000**, *278*, 267–271. [[CrossRef](#)]
204. Liu, D.-B.; Chen, M.-F.; Ye, X.-Y. Fabrication and corrosion behavior of HA/Mg-Zn biocomposites. *Front. Mater. Sci.* **2010**, *4*, 139–144. [[CrossRef](#)]
205. Ye, X.; Chen, M.; Yang, M.; Wei, J.; Liu, D. In vitro corrosion resistance and cytocompatibility of nano-hydroxyapatite reinforced Mg–Zn–Zr composites. *J. Mater. Sci. Mater. Med.* **2010**, *21*, 1321–1328. [[CrossRef](#)]
206. He, S.-Y.; Yue, S.; Chen, M.-F.; Liu, D.-B.; Ye, X.-Y. Microstructure and properties of biodegradable β -TCP reinforced Mg-Zn-Zr composites. *T. Nonferr. Metal Soc.* **2011**, *21*, 814–819. [[CrossRef](#)]
207. Cifuentes, S.C.; Frutos, E.; González-Carrasco, J.L.; Muñoz, M.; Multigner, M.; Chao, J.; Benavente, R.; Lieblich, M. Novel PLLA/magnesium composite for orthopedic applications: A proof of concept. *Mater. Lett.* **2012**, *74*, 239–242. [[CrossRef](#)]
208. Yu, K.; Chen, L.; Zhao, J.; Li, S.; Dai, Y.; Huang, Q.; Yu, Z. In vitro corrosion behavior and in vivo biodegradation of biomedical β -Ca₃(PO₄)₂/Mg–Zn composites. *Acta Biomater.* **2012**, *8*, 2845–2855. [[CrossRef](#)]
209. Wang, J.; Huang, S.; Wei, Y.; Guo, S.; Fusheng, P. Enhanced mechanical properties and corrosion resistance of a Mg–Zn–Ca bulk metallic glass composite by Fe particle addition. *Mater. Lett.* **2013**, *91*, 311–314. [[CrossRef](#)]
210. Gu, X.; Shiflet, G.; Guo, F.; Poon, S. Mg–Ca–Zn bulk metallic glasses with high strength and significant ductility. *J. Mater. Res.* **2005**, *20*, 1935–1938. [[CrossRef](#)]
211. Gu, X.; Zheng, Y.; Zhong, S.; Xi, T.; Wang, J.; Wang, W. Corrosion of, and cellular responses to Mg–Zn–Ca bulk metallic glasses. *Biomaterials* **2010**, *31*, 1093–1103. [[CrossRef](#)] [[PubMed](#)]
212. Kamado, S.; Ikeya, N.; Rudi, R.S.; Araki, T.; Kojima, Y. Application of semi-solid forming to Mg-Zn-Al-Ca alloys. In *Materials Science Forum*; Kojima, Y., Aizawa, T., Kamado, S., Eds.; Trans Tech Publ.: Zürich, Switzerland, 2000; pp. 205–214.

213. Blawert, C.; Morales, E.D.; Dietzel, W.; Kainer, K.U. Comparison of corrosion properties of squeeze cast and thixocast MgZnRE alloys. In *Materials Science Forum*; Ke, W., Han, E.H., Han, Y.F., Eds.; Trans Tech Publ.: Zürich, Switzerland, 2005; pp. 697–700.
214. Mo, W.; Zhang, L.; Wu, G.; Zhang, Y.; Liu, W.; Wang, C. Effects of processing parameters on microstructure and mechanical properties of squeeze-cast Mg–12Zn–4Al–0.5 Ca alloy. *Mater. Des.* **2014**, *63*, 729–737. [[CrossRef](#)]
215. Doležal, P.; Zapletal, J.; Fintová, S.; Trojanová, Z.; Greger, M.; Roupčová, P.; Podrábský, T. Influence of processing techniques on microstructure and mechanical properties of a biodegradable Mg-3Zn-2Ca alloy. *Materials* **2016**, *9*, 880. [[CrossRef](#)]
216. Chen, H.-M.; Yu, H.-S.; Kang, S.-B.; Min, G.-H.; Jin, Y.-X. Effect of rolling temperature on microstructure and texture of twin roll cast ZK60 magnesium alloy. *T. Nonferr. Metal Soc.* **2010**, *20*, 2086–2091. [[CrossRef](#)]
217. Park, S.S.; Bae, G.; Kang, D.; Jung, I.-H.; Shin, K.; Kim, N.J. Microstructure and tensile properties of twin-roll cast Mg–Zn–Mn–Al alloys. *Scripta Mater.* **2007**, *57*, 793–796. [[CrossRef](#)]
218. Wang, S.-R.; Min, W.; Kang, S.-B.; Cho, J.-H. Microstructure comparison of ZK60 alloy under casting, twin roll casting and hot compression. *T. Nonferr. Metal Soc.* **2010**, *20*, 763–768. [[CrossRef](#)]
219. Watari, H.; Davey, K.; Rasgado, M.; Haga, T.; Izawa, S. Semi-solid manufacturing process of magnesium alloys by twin-roll casting. *J. Mater. Process. Technol.* **2004**, *155*, 1662–1667. [[CrossRef](#)]
220. Park, S.S.; Park, W.-J.; Kim, C.; You, B.; Kim, N.J. The twin-roll casting of magnesium alloys. *JOM* **2009**, *61*, 14. [[CrossRef](#)]
221. Oktay, G.; Ürgen, M. Corrosion behaviour of magnesium AZ31 sheet produced by twin roll casting. *Corros. Eng. Sci. Technol.* **2015**, *50*, 380–389. [[CrossRef](#)]
222. Mendis, C.; Bae, J.; Kim, N.; Hono, K. Microstructures and tensile properties of a twin roll cast and heat-treated Mg–2.4 Zn–0.1 Ag–0.1 Ca–0.1 Zr alloy. *Scripta Mater.* **2011**, *64*, 335–338. [[CrossRef](#)]
223. Kim, N. Critical assessment 6: Magnesium sheet alloys: Viable alternatives to steels? *Mater. Sci. Technol.* **2014**, *30*, 1925–1928. [[CrossRef](#)]
224. Park, S.S.; Bae, G.; Kang, D.; You, B.; Kim, N.J. Superplastic deformation behavior of twin-roll cast Mg–6Zn–1Mn–1Al alloy. *Scripta Mater.* **2009**, *61*, 223–226. [[CrossRef](#)]
225. Hou, R.; Victoria-Hernandez, J.; Jiang, P.; Willumeit-Römer, R.; Luthringer-Feyerabend, B.; Yi, S.; Letzig, D.; Feyerabend, F. In vitro evaluation of the ZX11 magnesium alloy as potential bone plate: Degradability and mechanical integrity. *Acta Biomater.* **2019**, *97*, 608–622. [[CrossRef](#)] [[PubMed](#)]
226. Victoria-Hernández, J.; Yi, S.; Klaumünzer, D.; Letzig, D. Recrystallization behavior and its relationship with deformation mechanisms of a hot rolled Mg-Zn-Ca-Zr alloy. *Mater. Sci. Eng. A* **2019**, *761*, 138054. [[CrossRef](#)]
227. Klaumünzer, D.; Marx, A.; Schauerte, O.; Wollenberg, A.; Letzig, D.; Yi, S.; Victoria-Hernández, J.; Uggowitzer, P.; Knwon, O.-D.; Kim, J.J.; et al. Magnesium Alloy Sheet Produced by Twin Roll Casting. EP3205736A1, 22 August 2018.
228. Yamasaki, M.; Hayashi, N.; Izumi, S.; Kawamura, Y. Corrosion behavior of rapidly solidified Mg–Zn–rare earth element alloys in NaCl solution. *Corros. Sci.* **2007**, *49*, 255–262. [[CrossRef](#)]
229. Shuai, C.; Yang, Y.; Wu, P.; Lin, X.; Liu, Y.; Zhou, Y.; Feng, P.; Liu, X.; Peng, S. Laser rapid solidification improves corrosion behavior of Mg–Zn–Zr alloy. *J. Alloys Compd.* **2017**, *691*, 961–969. [[CrossRef](#)]
230. Xu, Z.; Smith, C.; Chen, S.; Sankar, J. Development and microstructural characterizations of Mg–Zn–Ca alloys for biomedical applications. *Mater. Sci. Eng. B* **2011**, *176*, 1660–1665. [[CrossRef](#)]
231. Hornberger, H.; Virtanen, S.; Boccaccini, A. Biomedical coatings on magnesium alloys—A review. *Acta Biomater.* **2012**, *8*, 2442–2455. [[CrossRef](#)]
232. Chen, X.; Yang, H.Y.; Abbott, T.; Easton, M.A.; Birbilis, N. Corrosion-resistant electrochemical platings on magnesium alloys: A state-of-the-art review. *Corrosion* **2012**, *68*, 518–535. [[CrossRef](#)]
233. Singh, A.; Harimkar, S.P. Laser surface engineering of magnesium alloys: A review. *JOM* **2012**, *64*, 716–733. [[CrossRef](#)]
234. Yang, J.; Cui, F.-z.; Lee, I.S.; Wang, X. Plasma surface modification of magnesium alloy for biomedical application. *Surf. Coat. Technol.* **2010**, *205*, S182–S187. [[CrossRef](#)]
235. Gray, J.; Luan, B. Protective coatings on magnesium and its alloys—A critical review. *J. Alloys Compd.* **2002**, *336*, 88–113. [[CrossRef](#)]
236. Hu, R.-G.; Zhang, S.; Bu, J.-F.; Lin, C.-J.; Song, G.-L. Recent progress in corrosion protection of magnesium alloys by organic coatings. *Prog. Org. Coat.* **2012**, *73*, 129–141. [[CrossRef](#)]

237. Chen, X.; Birbilis, N.; Abbott, T. Review of corrosion-resistant conversion coatings for magnesium and its alloys. *Corrosion* **2011**, *67*, 035005-1–035005-16. [[CrossRef](#)]
238. Wang, J.; Tang, J.; Zhang, P.; Li, Y.; Wang, J.; Lai, Y.; Qin, L. Surface modification of magnesium alloys developed for bioabsorbable orthopedic implants: A general review. *J. Biomed. Mater. Res. B Appl. Biomater.* **2012**, *100*, 1691–1701. [[CrossRef](#)]
239. Uddin, M.; Hall, C.; Murphy, P. Surface treatments for controlling corrosion rate of biodegradable Mg and Mg-based alloy implants. *Sci. Technol. Adv. Mat.* **2015**, *16*, 053501. [[CrossRef](#)]
240. Pommiers-Belin, S.; Frayret, J.; Uhart, A.; Ledeuil, J.; Dupin, J.-C.; Castetbon, A.; Potin-Gautier, M. Determination of the chemical mechanism of chromate conversion coating on magnesium alloys EV31A. *Appl. Surf. Sci.* **2014**, *298*, 199–207. [[CrossRef](#)]
241. Yong, Z.; Zhu, J.; Qiu, C.; Liu, Y. Molybdate/phosphate composite conversion coating on magnesium alloy surface for corrosion protection. *Appl. Surf. Sci.* **2008**, *255*, 1672–1680. [[CrossRef](#)]
242. Yang, K.; Ger, M.; Hwu, W.; Sung, Y.; Liu, Y. Study of vanadium-based chemical conversion coating on the corrosion resistance of magnesium alloy. *Mater. Chem. Phys.* **2007**, *101*, 480–485. [[CrossRef](#)]
243. Zhao, M.; Wu, S.; Luo, J.; Fukuda, Y.; Nakae, H. A chromium-free conversion coating of magnesium alloy by a phosphate–permanganate solution. *Surf. Coat. Technol.* **2006**, *200*, 5407–5412. [[CrossRef](#)]
244. Lee, Y.; Chu, Y.; Li, W.; Lin, C. Effect of permanganate concentration on the formation and properties of phosphate/permanganate conversion coating on AZ31 magnesium alloy. *Corros. Sci.* **2013**, *70*, 74–81. [[CrossRef](#)]
245. Zhang, H.; Yao, G.; Wang, S.; Liu, Y.; Luo, H. A chrome-free conversion coating for magnesium–lithium alloy by a phosphate–permanganate solution. *Surf. Coat. Technol.* **2008**, *202*, 1825–1830. [[CrossRef](#)]
246. Hu, J.; Li, Q.; Zhong, X.; Zhang, L.; Chen, B. Composite anticorrosion coatings for AZ91D magnesium alloy with molybdate conversion coating and silicon sol–gel coatings. *Prog. Org. Coat.* **2009**, *66*, 199–205. [[CrossRef](#)]
247. Li, K.; Liu, J.; Lei, T.; Xiao, T. Optimization of process factors for self-healing vanadium-based conversion coating on AZ31 magnesium alloy. *Appl. Surf. Sci.* **2015**, *353*, 811–819. [[CrossRef](#)]
248. Niu, L.; Chang, S.-H.; Tong, X.; Li, G.; Shi, Z. Analysis of characteristics of vanadate conversion coating on the surface of magnesium alloy. *J. Alloys Compd.* **2014**, *617*, 214–218. [[CrossRef](#)]
249. Lin, C.; Lin, H.; Lin, K.; Lai, W. Formation and properties of stannate conversion coatings on AZ61 magnesium alloys. *Corros. Sci.* **2006**, *48*, 93–109. [[CrossRef](#)]
250. Li, Z.; Dai, C.-I.; Liu, Y.-I.; Zhu, J. Study of Silicate and Tungstate Composite Conversion Coating on Magnesium Alloy. *Electroplating Pollut. Control* **2007**, *27*, 16.
251. Yang, Y.; Tsai, C.; Huang, Y.; Lin, C. Formation mechanism and properties of titanate conversion coating on AZ31 magnesium alloy. *J. Electrochem. Soc.* **2012**, *159*, C226–C232. [[CrossRef](#)]
252. Jian, S.-Y.; Chu, Y.-R.; Lin, C.-S. Permanganate conversion coating on AZ31 magnesium alloys with enhanced corrosion resistance. *Corros. Sci.* **2015**, *93*, 301–309. [[CrossRef](#)]
253. Zhang, X.; Liang, J.; Liu, B.; Peng, Z. Preparation of superhydrophobic zinc coating for corrosion protection. *Colloids Surf. Physicochem. Eng. Aspects* **2014**, *454*, 113–118. [[CrossRef](#)]
254. Park, B.C. Method of preparing copper plating layer having high adhesion to magnesium alloy using electroplating. US7368047B2, 6 May 2008.
255. Macary, R.L. Method of chrome plating magnesium and magnesium alloys. US8152985B2, 10 April 2012.
256. Zhang, Z.; Yu, G.; Ouyang, Y.; He, X.; Hu, B.; Zhang, J.; Wu, Z. Studies on influence of zinc immersion and fluoride on nickel electroplating on magnesium alloy AZ91D. *Appl. Surf. Sci.* **2009**, *255*, 7773–7779. [[CrossRef](#)]
257. Song, G.-L.; Shi, Z. Corrosion mechanism and evaluation of anodized magnesium alloys. *Corros. Sci.* **2014**, *85*, 126–140. [[CrossRef](#)]
258. Blawert, C.; Dietzel, W.; Ghali, E.; Song, G. Anodizing treatments for magnesium alloys and their effect on corrosion resistance in various environments. *Adv. Eng. Mater.* **2006**, *8*, 511–533. [[CrossRef](#)]
259. Lu, X.; Blawert, C.; Kainer, K.U.; Zheludkevich, M.L. Investigation of the formation mechanisms of plasma electrolytic oxidation coatings on Mg alloy AM50 using particles. *Electrochim. Acta* **2016**, *196*, 680–691. [[CrossRef](#)]
260. Lu, X.; Blawert, C.; Huang, Y.; Ovri, H.; Zheludkevich, M.L.; Kainer, K.U. Plasma electrolytic oxidation coatings on Mg alloy with addition of SiO₂ particles. *Electrochim. Acta* **2016**, *187*, 20–33. [[CrossRef](#)]

261. Shao, Y.; Huang, H.; Zhang, T.; Meng, G.; Wang, F. Corrosion protection of Mg–5Li alloy with epoxy coatings containing polyaniline. *Corros. Sci.* **2009**, *51*, 2906–2915. [[CrossRef](#)]
262. Truong, V.-T.; Lai, P.; Moore, B.; Muscat, R.; Russo, M. Corrosion protection of magnesium by electroactive polypyrrole/paint coatings. *Synthetic Met.* **2000**, *110*, 7–15. [[CrossRef](#)]
263. Wong, H.M.; Yeung, K.W.; Lam, K.O.; Tam, V.; Chu, P.K.; Luk, K.D.; Cheung, K.M. A biodegradable polymer-based coating to control the performance of magnesium alloy orthopaedic implants. *Biomaterials* **2010**, *31*, 2084–2096. [[CrossRef](#)]
264. Hoche, H.; Groß, S.; Oechsner, M. Development of new PVD coatings for magnesium alloys with improved corrosion properties. *Surf. Coat. Technol.* **2014**, *259*, 102–108. [[CrossRef](#)]
265. Wu, G.; Zeng, X.; Yuan, G. Growth and corrosion of aluminum PVD-coating on AZ31 magnesium alloy. *Mater. Lett.* **2008**, *62*, 4325–4327. [[CrossRef](#)]
266. Altun, H.; Sen, S. The effect of PVD coatings on the corrosion behaviour of AZ91 magnesium alloy. *Mater. Des.* **2006**, *27*, 1174–1179. [[CrossRef](#)]
267. Gao, Y.-l.; Wang, C.-S.; Yao, M.; Liu, H.-B. The resistance to wear and corrosion of laser-cladding Al₂O₃ ceramic coating on Mg alloy. *Appl. Surf. Sci.* **2007**, *253*, 5306–5311. [[CrossRef](#)]
268. Ignat, S.; Sallamand, P.; Grevey, D.; Lambertin, M. Magnesium alloys laser (Nd: YAG) cladding and alloying with side injection of aluminium powder. *Appl. Surf. Sci.* **2004**, *225*, 124–134. [[CrossRef](#)]
269. Kim, J.; Lee, S.; Park, J.; Kim, H. Laser surface modification of Ti and TiC coatings on magnesium alloy. *Phys. Met. Metallogr.* **2014**, *115*, 1389–1394. [[CrossRef](#)]
270. Qian, J.; Yin, Y.; Li, T.; Hu, X.; Wang, C.; Li, S. Structure, micro-hardness and corrosion behaviour of the Al–Si/Al₂O₃ coatings prepared by laser plasma hybrid spraying on magnesium alloy. *Vacuum* **2015**, *117*, 55–59. [[CrossRef](#)]
271. Waterman, J.; Staiger, M. Coating systems for magnesium-based biomaterials—State of the art. In *Magnesium Technology 2011*; Neelameggham, A.R., Mathaudhu, S.N., Eds.; Springer: Berlin/Heidelberg, Germany, 2011; pp. 403–408.
272. Aghion, E.; Bronfin, B. Magnesium alloys development towards the 21st century. In *Materials Science Forum*; Kojima, Y., Aizawa, T., Kamado, S., Eds.; Trans Tech Publ.: Zürich, Switzerland, 2000; pp. 19–30.
273. Luo, A.A. Magnesium casting technology for structural applications. *J. Magnes. Alloys* **2013**, *1*, 2–22. [[CrossRef](#)]
274. Luo, A.; Renaud, J.; Nakatsugawa, I.; Plourde, J. Magnesium castings for automotive applications. *JOM* **1995**, *47*, 28–31. [[CrossRef](#)]
275. Powell, B.; Luo, A.; Krajewski, P. Magnesium alloys for lightweight powertrains and automotive bodies. In *Advanced Materials in Automotive Engineering*; Rowe, J., Ed.; Elsevier: Amsterdam, The Netherlands, 2012; pp. 150–209.
276. Luo, A.; Shinoda, T. A new magnesium alloy for automotive powertrain applications. *SAE Trans.* **1998**, *107*, 86–94.
277. Klaumünzer, D.; Hernandez, J.V.; Yi, S.; Letzig, D.; Kim, S.-h.; Kim, J.J.; Seo, M.H.; Ahn, K. Magnesium Process and Alloy Development for Applications in the Automotive Industry. In *Magnesium Technology 2019*; Springer: Berlin/Heidelberg, Germany, 2019; pp. 15–20.
278. He, Y.; Tao, H.; Zhang, Y.; Jiang, Y.; Zhang, S.; Zhao, C.; Li, J.; Zhang, B.; Song, Y.; Zhang, X. Biocompatibility of bio-Mg-Zn alloy within bone with heart, liver, kidney and spleen. *Chin. Sci. Bull.* **2009**, *54*, 484–491. [[CrossRef](#)]
279. Chen, D.; He, Y.; Tao, H.; Zhang, Y.; Jiang, Y.; Zhang, X.; Zhang, S. Biocompatibility of magnesium-zinc alloy in biodegradable orthopedic implants. *Int. J. Mol. Med.* **2011**, *28*, 343–348. [[PubMed](#)]
280. Kraus, T.; Fischerauer, S.F.; Hänzli, A.C.; Uggowitzer, P.J.; Löffler, J.F.; Weinberg, A.M. Magnesium alloys for temporary implants in osteosynthesis: In vivo studies of their degradation and interaction with bone. *Acta Biomater.* **2012**, *8*, 1230–1238. [[CrossRef](#)]
281. Ben-Hamu, G.; Eliezer, D.; Shin, K. Influence of Si, Ca and Ag addition on corrosion behaviour of new wrought Mg–Zn alloys. *Mater. Sci. Technol.* **2006**, *22*, 1213–1218. [[CrossRef](#)]
282. Ben-Hamu, G.; Eliezer, D.; Shin, K. The role of Si and Ca on new wrought Mg–Zn–Mn based alloy. *Mater. Sci. Eng. A* **2007**, *447*, 35–43. [[CrossRef](#)]
283. Wang, L.-X.; Song, R.-B.; Cai, C.-H.; Li, J.-Y. Enhanced Strength and Corrosion Resistance of Mg–2Zn–0.6Zr Alloy with Extrusion. *Acta Metall. Sin.-Engl.* **2019**, *32*, 10–22. [[CrossRef](#)]

284. Baek, S.-M.; Kim, B.; Park, S.S. Influence of Intermetallic Particles on the Corrosion Properties of Extruded ZK60 Mg Alloy Containing Cu. *Metals* **2018**, *8*, 323. [[CrossRef](#)]
285. Zhang, Y.; Li, J.; Li, J. Microstructure, mechanical properties, corrosion behavior and film formation mechanism of Mg-Zn-Mn-xNd in Kokubo's solution. *J. Alloys Compd.* **2018**, *730*, 458–470. [[CrossRef](#)]
286. Zhang, Y.; Li, J.; Li, J. Effects of microstructure transformation on mechanical properties, corrosion behaviors of Mg-Zn-Mn-Ca alloys in simulated body fluid. *J. Mech. Behav. Biomed.* **2018**, *80*, 246–257. [[CrossRef](#)]
287. Zhang, Y.; Li, J.; Li, J. Effects of Calcium addition on phase characteristics and corrosion behaviors of Mg-2Zn-0.2 Mn-xCa in simulated body fluid. *J. Alloys Compd.* **2017**, *728*, 37–46. [[CrossRef](#)]
288. Buzolin, R.; Mohedano, M.; Mendis, C.; Mingo, B.; Tolnai, D.; Blawert, C.; Kainer, K.; Pinto, H.; Hort, N. As cast microstructures on the mechanical and corrosion behaviour of ZK40 modified with Gd and Nd additions. *Mater. Sci. Eng. A* **2017**, *682*, 238–247. [[CrossRef](#)]
289. Zheng, Y.; Li, Y.; Chen, J.; Zou, Z. Effects of tensile and compressive deformation on corrosion behaviour of a Mg-Zn alloy. *Corros. Sci.* **2015**, *90*, 445–450. [[CrossRef](#)]
290. Gao, J.; Guan, S.; Ren, Z.; Sun, Y.; Zhu, S.; Wang, B. Homogeneous corrosion of high pressure torsion treated Mg-Zn-Ca alloy in simulated body fluid. *Mater. Lett.* **2011**, *65*, 691–693. [[CrossRef](#)]
291. Liu, D.; Liu, Y.; Huang, Y.; Song, R.; Chen, M. Effects of solidification cooling rate on the corrosion resistance of Mg-Zn-Ca alloy. *Progr. Nat. Sci.* **2014**, *24*, 452–457. [[CrossRef](#)]
292. Tong, L.; Zheng, M.; Xu, S.; Kamado, S.; Du, Y.; Hu, X.; Wu, K.; Gan, W.; Brokmeier, H.; Wang, G. Effect of Mn addition on microstructure, texture and mechanical properties of Mg-Zn-Ca alloy. *Mater. Sci. Eng. A* **2011**, *528*, 3741–3747. [[CrossRef](#)]
293. Homma, T.; Mendis, C.; Hono, K.; Kamado, S. Effect of Zr addition on the mechanical properties of as-extruded Mg-Zn-Ca-Zr alloys. *Mater. Sci. Eng. A* **2010**, *527*, 2356–2362. [[CrossRef](#)]
294. Cao, J.; Laws, K.; Birbilis, N.; Ferry, M. Potentiodynamic polarisation study of bulk metallic glasses based on the Mg-Zn-Ca ternary system. *Corros. Eng. Sci. Technol.* **2012**, *47*, 329–334. [[CrossRef](#)]
295. Wang, J.; Wei, Y.; Guo, S.; Huang, S.; Zhou, X.; Pan, F. The Y-doped MgZnCa alloys with ultrahigh specific strength and good corrosion resistance in simulated body fluid. *Mater. Lett.* **2012**, *81*, 112–114. [[CrossRef](#)]
296. Wang, J.; Li, Y.; Huang, S.; Wei, Y.; Xi, X.; Cai, K.; Pan, F. Effects of Y on the Microstructure, Mechanical and Bio-corrosion Properties of Mg-Zn-Ca Bulk Metallic Glass. *J. Mater. Sci. Technol.* **2014**, *30*, 1255–1261. [[CrossRef](#)]
297. Wang, Y.; Tan, M.J.; Pang, J.; Wang, Z.; Jarfors, A.W. In vitro corrosion behaviors of Mg₆₇Zn₂₈Ca₅ alloy: From amorphous to crystalline. *Mater. Chem. Phys.* **2012**, *134*, 1079–1087. [[CrossRef](#)]
298. Ramya, M.; Sarwat, S.G.; Udhayabanu, V.; Subramanian, S.; Raj, B.; Ravi, K. Role of partially amorphous structure and alloying elements on the corrosion behavior of Mg-Zn-Ca bulk metallic glass for biomedical applications. *Mater. Des.* **2015**, *86*, 829–835. [[CrossRef](#)]
299. Yamasaki, M.; Izumi, S.; Kawamura, Y. Development of High Strength and Highly Corrosion-Resistant Bulk Nanocrystalline Mg-Zn-Y Alloys with Long Period Stacking Ordered Phase. *ECS Trans.* **2009**, *16*, 81–88.
300. Izumi, S.; Yamasaki, M.; Kawamura, Y. Relation between corrosion behavior and microstructure of Mg-Zn-Y alloys prepared by rapid solidification at various cooling rates. *Corros. Sci.* **2009**, *51*, 395–402. [[CrossRef](#)]
301. Xu, D.; Tang, W.; Liu, L.; Xu, Y.; Han, E. Effect of W-phase on the mechanical properties of as-cast Mg-Zn-Y-Zr alloys. *J. Alloys Compd.* **2008**, *461*, 248–252. [[CrossRef](#)]
302. Pérez, P.; Onofre, E.; Cabeza, S.; Llorente, I.; Del Valle, J.; García-Alonso, M.; Adeva, P.; Escudero, M. Corrosion behaviour of Mg-Zn-Y-Mischmetal alloys in phosphate buffer saline solution. *Corros. Sci.* **2013**, *69*, 226–235. [[CrossRef](#)]
303. Wang, S.; Xu, D.; Chen, X.; Han, E.; Dong, C. Effect of heat treatment on the corrosion resistance and mechanical properties of an as-forged Mg-Zn-Y-Zr alloy. *Corros. Sci.* **2015**, *92*, 228–236. [[CrossRef](#)]
304. Fei, S.; Wang, C.-Q.; Zhang, Z.-M. Microstructures, corrosion and mechanical properties of as-cast Mg-Zn-Y-(Gd) alloys. *T. Nonferr. Metal Soc.* **2015**, *25*, 2172–2180.
305. Singh, A.; Nakamura, M.; Watanabe, M.; Kato, A.; Tsai, A. Quasicrystal strengthened Mg-Zn-Y alloys by extrusion. *Scripta Mater.* **2003**, *49*, 417–422. [[CrossRef](#)]
306. Wang, J.; Song, P.; Gao, S.; Huang, X.; Shi, Z.; Pan, F. Effects of Zn on the microstructure, mechanical properties, and damping capacity of Mg-Zn-Y-Zr alloys. *Mater. Sci. Eng. A* **2011**, *528*, 5914–5920. [[CrossRef](#)]
307. Song, R.; Liu, D.-B.; Liu, Y.-C.; Zheng, W.-B.; Zhao, Y.; Chen, M.-F. Effect of corrosion on mechanical behaviors of Mg-Zn-Zr alloy in simulated body fluid. *Front. Mater. Sci.* **2014**, *8*, 264–270. [[CrossRef](#)]

308. Hong, D.; Saha, P.; Chou, D.-T.; Lee, B.; Collins, B.E.; Tan, Z.; Dong, Z.; Kumta, P.N. In vitro degradation and cytotoxicity response of Mg-4% Zn-0.5% Zr (ZK40) alloy as a potential biodegradable material. *Acta Biomater.* **2013**, *9*, 8534–8547. [[CrossRef](#)] [[PubMed](#)]
309. Liu, W.; Dong, J.; Zhang, P.; Yao, Z.; Zhai, C.; Ding, W. High cycle fatigue behavior of as-extruded ZK60 magnesium alloy. *J. Mater. Sci. Mater. Med.* **2009**, *44*, 2916. [[CrossRef](#)]
310. Zhang, Y.; Zeng, X.; Liu, L.; Lu, C.; Zhou, H.; Li, Q.; Zhu, Y. Effects of yttrium on microstructure and mechanical properties of hot-extruded Mg-Zn-Y-Zr alloys. *Mater. Sci. Eng. A* **2004**, *373*, 320–327. [[CrossRef](#)]
311. Yu, W.; Liu, Z.; He, H.; Cheng, N.; Li, X. Microstructure and mechanical properties of ZK60-Yb magnesium alloys. *Mater. Sci. Eng. A* **2008**, *478*, 101–107. [[CrossRef](#)]
312. Yamasaki, M.; Anan, T.; Yoshimoto, S.; Kawamura, Y. Mechanical properties of warm-extruded Mg-Zn-Gd alloy with coherent 14H long periodic stacking ordered structure precipitate. *Scripta Mater.* **2005**, *53*, 799–803. [[CrossRef](#)]
313. Yuan, G.; Liu, Y.; Lu, C.; Ding, W. Effect of quasicrystal and Laves phases on strength and ductility of as-extruded and heat treated Mg-Zn-Gd-based alloys. *Mater. Sci. Eng. A* **2008**, *472*, 75–82. [[CrossRef](#)]
314. Zhang, E.; Yin, D.; Xu, L.; Yang, L.; Yang, K. Microstructure, mechanical and corrosion properties and biocompatibility of Mg-Zn-Mn alloys for biomedical application. *Mater. Sci. Eng. C* **2009**, *29*, 987–993. [[CrossRef](#)]
315. Zhang, Y.; Li, J.; Lai, H.; Xu, Y. Effect of Homogenization on Microstructure Characteristics, Corrosion and Biocompatibility of Mg-Zn-Mn-xCa Alloys. *Materials* **2018**, *11*, 227. [[CrossRef](#)]
316. Zhang, Y.; Li, J.-y.; Liaw, P.K.; Xu, Y.-z.; Lai, H.-y. Effects of heat treatment on the mechanical properties and corrosion behaviour of the Mg-2Zn-0.2 Mn-xNd alloys. *J. Alloys Compd.* **2018**, *769*, 552–565. [[CrossRef](#)]
317. He, R.; Liu, R.; Chen, Q.; Zhang, H.; Wang, J.; Guo, S. In vitro degradation behavior and cytocompatibility of Mg-6Zn-Mn alloy. *Mater. Lett.* **2018**, *228*, 77–80. [[CrossRef](#)]
318. Guangyin, Y.; Manping, L.; Wenjiang, D.; Inoue, A. Microstructure and mechanical properties of Mg-Zn-Si-based alloys. *Mater. Sci. Eng. A* **2003**, *357*, 314–320. [[CrossRef](#)]
319. Mengqi, C.; Ziquan, L.; Jinsong, L.; Menghui, W.; Beibei, S.; Bijun, W. Corrosion Behavior of as-Cast Mg-6Zn-4Si Alloy with Sr Addition. *Rare Metal Mat. Eng.* **2017**, *46*, 2405–2410. [[CrossRef](#)]
320. Jihua, C.; Zhenhua, C.; Hongge, Y.; Fuquan, Z.; Yingliang, C. Effects of Sn and Ca additions on microstructure, mechanical properties, and corrosion resistance of the as-cast Mg-Zn-Al-based alloy. *Mater. Corros.* **2008**, *59*, 934–941. [[CrossRef](#)]
321. Xiao, W.; Jia, S.; Wang, L.; Wu, Y.; Wang, L. The microstructures and mechanical properties of cast Mg-Zn-Al-RE alloys. *J. Alloys Compd.* **2009**, *480*, L33–L36. [[CrossRef](#)]
322. Yang, M.; Pan, F. Effects of Sn addition on as-cast microstructure, mechanical properties and casting fluidity of ZA84 magnesium alloy. *Mater. Des.* **2010**, *31*, 68–75. [[CrossRef](#)]
323. Jayalakshmi, S.; Kailas, S.V.; Seshan, S.; Fleury, E. Properties of squeeze cast Mg-6Zn-3Cu alloy and its saffil alumina short fibre reinforced composites. *J. Mater. Sci. Mater. Med.* **2006**, *41*, 3743–3752. [[CrossRef](#)]

